Non-Ideal Effects on the Stability and Transport of Magnetized Plasmas

Nathaniel Mandrachia Ferraro

A dissertation
presented to the faculty
of Princeton University
in candidacy for the degree
of Doctor of Philosophy

Recommended for acceptance by
the department of
astrophysical sciences

Adviser: Stephen Jardin

November, 2008

Abstract

Magnetohydrodynamics (MHD), a fluid model of the low-frequency behavior of magnetized plasma, provides the most successful framework for understanding the equilibrium and large-scale stability of magnetically confined plasma. The success of this model is due in large part to its simplicity relative to more complete models. Much of this simplicity comes at the expense of the omission of non-ideal effects, which include dissipation, two-fluid and finite Larmor radius effects, micro-turbulence, and wave-particle interactions, among others. Often, the inclusion of these effects leads to important and unexpected phenomena. However, incorporating some of these effects, which may occur on vastly disparate spatial and temporal scales, introduces significant mathematical complexity and makes obtaining numerical solutions substantially more difficult. This dissertation investigates methods for numerically solving fluid models that have been extended to include some of these non-ideal effects, and to use these methods together with analytic theory to explore non-ideal effects on the steady-states and stability of magnetized plasmas.

An overview of the two-fluid model of a magnetized plasma is given. This overview includes discussion of various methods of closing the fluid equations, and the physical effects included (or excluded) by each method. A method for the solution of a generic set of collisional two-fluid equations is described, and results from an implementation of this method, the numerical code M3D-C^1, are presented. The importance of two-fluid effects and

gyroviscosity on the linear growth rate of three instabilities—the gravitational instability, the magnetorotational instability, and the magnetothermal instability—is demonstrated analytically. It is shown that gyroviscosity, in particular, may play an important role in the stability threshold of these instabilities. Toroidal axisymmetric steady-states of the two-fluid model are obtained using M3D-C^1 for magnetic configurations typical of the National Spherical Torus Experiment (NSTX). These steady-states represent the first such states obtained with self-consistently determined flow of a dissipative model in realistic geometry. Resistively-driven radial flows are shown to be in excellent agreement with Pfirsch-Schlüter theory. Qualitative and quantitative agreement is found with comparable results for resistively-driven toroidal edge flows. New results, including toroidal rotation and oscillation due to gyroviscosity, are characterized and discussed.

Acknowledgments

This work would not have been possible without the involvement and support of many people, both personal and professional. I gratefully acknowledge the invaluable support of Sam Cohen, who shepherded me through my first years at Princeton and always provides enthusiastic skepticism; Greg Hammett, with whom I have shared many insightful conversations on a range of topics including the magnetorotational instability, the interpretation of viscosity, and numerical methods; and of course my adviser Steve Jardin, upon whom I have relied for knowledge and guidance and whose contributions to this work are far too numerous to list here. Conversations with many others over the past five years have provided many useful insights, including those with Ian Parrish (who piqued my interest in the magnetorotational and magnetothermal instabilities), Jesus Ramos, Carl Sovinec, Dalton Schnack, Slava Lukin, and many others. I also gratefully appreciate the guidance of Barrett Rogers, who introduced me to plasma physics and set me out on the right foot. Of all the impressive people at Princeton, perhaps the most impressive to me is Barbara Sarfaty, without whom the graduate program in plasma physics could simply not function, and to whom I personally owe a debt of gratitude. Financial support for this work has been provided through Princeton's graduate program in plasma physics, US DOE contract DE-AC02-76CH03073, and Princeton's Charlotte E. Proctor fellowship.

On a personal level, I thank my parents, to whom I owe everything, for their gracious and sincere support of my scientific ambitions throughout my

life. I sincerely apologize to my father for the use of imaginary numbers in this work, and hope that one day he softens his position that they represent a heinous affront to human dignity. For his sake I have avoided any mention of "dark energy" in the pages that follow. I have benefited greatly from taking the opportunity to interact with, and occasionally befriend, the talented and motivated individuals who make up the graduate student population at Princeton. I thank the PPPL Tokabats for a much-needed diversion this past summer, and wish them continued success in my absence. Finally, I acknowledge the loving support of Monica Skoge, whose support on both personal and professional levels have meant the world to me.

Contents

List of Figures

Chapter 1

Introduction

1.1 Magnetic Fusion Energy

The goal of magnetic fusion energy (MFE) research is to discover and optimize profitable methods for extracting the energy released from fusion reactions occurring in plasma confined by magnetic fields. To achieve this, the plasma must be held at a high temperature continuously and without disruption, in order to ensure the essentially uninterrupted power generation required of commercial power plants. The properties of the steady-state must be such that the thermal energy of plasma is not rapidly transported to the walls, as this transport would degrade the efficiency of the reactor by necessitating the injection of power into the plasma to keep it at fusion temperatures. Thus a major focus of MFE research is to optimize the stability and transport properties of magnetically confined plasma steady-states.[1]

The confinement of plasma by magnetic fields is made possible by the strongly anisotropic transport properties of a plasma in the presence of a magnetic field. Since particles may travel rapidly along magnetic field lines,

[1]The term "steady-state" is used in favor of "equilibrium" because fusion plasmas, being strongly driven by external sources of particles, energy, and momentum, are generally far from thermal equilibrium.

but are deflected by the Lorentz force when moving across field lines, the plasma may be well confined by "magnetic surfaces"—roughly, surfaces in space to which the magnetic field is everywhere tangent. Most magnetic fusion reactor concepts employ magnetic field configurations having such surfaces—configurations created either through currents in coils outside the plasma, through inducing currents within the plasma, or a combination of both methods.

Because the plasma must be at a much higher temperature than the wall of the device, the plasma must be held far from a global thermal equilibrium, with gradients in the thermal pressure balanced by the magnetic forces. Such a steady-state may be unstable, in several different ways. The most dangerous type of instability are magnetohydrodynamic (MHD) instabilities, which disrupt the magnetic field configuration on large scales. Such an instability may cause the plasma to be rapidly lost to the walls, and may even terminate the discharge. Some instabilities which saturate before the magnetic field is greatly perturbed may still destroy magnetic surfaces, significantly increasing the rate of energy transport to the walls. Other instabilities (micro-instabilities), driven by gradients in the density and temperature, may lead to the formation of turbulent convection cells which significantly enhance the transport of energy across magnetic surfaces. A successful reactor must operate sufficiently far from disruptive instability thresholds to minimize their occurrence, while also minimizing the deleterious transport effects of micro-instabilities.

There are several of types of toroidal magnetic fusion reactor concepts; however, much of the work presented here is most relevant to tokamak reactors in general, and the National Spherical Torus Experiment (NSTX) [1] in particular. The tokamak is the most well-developed fusion reactor concept, both theoretically and experimentally, having been the primary focus of fusion research in the United States over the past few decades. The international fusion reactor, ITER, is a tokamak design [2]. Yet there remain many

questions about the steady-states, transport, and stability of tokamak plasmas which must be answered before a commercial tokamak reactor can be realized. To adequately answer these questions will require a more complete model than ideal MHD.

One of the major such questions is an understanding of the H-mode ("high confinement" mode) of tokamak operation [3]. The H-mode is characterized by relatively stable, steep density and temperature gradients at the edge of the tokamak plasma. This is in contrast to the L-mode ("low confinement" mode), in which the gradients are relatively gentle and the edge is somewhat more turbulent. Because temperatures at the edge are kept relatively low through thermal coupling with the wall, plasmas in H-mode are able to achieve much higher temperatures in the core than in L-mode. Therefore understanding how to achieve and maintain H-mode, as well as a capability to predict the magnitude of the edge gradients, is crucial for successfully operating and designing tokamaks.

An understanding of the L-H mode transition is far from complete, but most present theories rely on the suppression of turbulent transport near the edge by sheared flow [4, 5]. The transition is rapid, and is characterized by the formation of a strongly negative (inward) radial electric field at the plasma edge, which drives poloidal particle drifts. Some models of this transition, such as those of Shaing [6] and Hassam [7], propose a bifurcation in the balance of poloidal torques, which may lead to a sudden onset of strong poloidal rotation which suppress edge turbulence. Hinton has proposed that poloidal rotation is driven by the ion thermal gradient, and that these flows reduce turbulent transport, which in turn allows a steepening of the gradient [8]. In any case, it appears that a model that is able to accurately describe the L-H transition will likely require the capability of self-consistently determining turbulent transport, flow, and thermodynamic profiles in the edge region.

Another important issue in tokamaks is edge-localized modes (ELMs), which are instabilities found to occur periodically at the plasma edge when

in H-mode operation, leading to bursts of enhanced transport at the plasma edge [9, 10]. An understanding of these modes is of importance to the successful operation of a tokamak reactor like ITER because the heat flux to certain plasma-facing components during an ELM event may be greater than that which can be safely absorbed by those components, which could result in their rapid degradation and destruction. It has been suggested that fluid drift effects or resistively driven edge flows could be stabilizing to ELMs [11, 12]; one might also suspect that the effect of finite Larmor radii (FLR) may play some stabilizing role, as it been shown to do in other instabilities [13].

Various analytical plasma models have been developed in order to gain an improved understanding of the stability and transport properties of tokamak plasmas. In general, these models may be divided into two main categories: fluid models, which consist of equations for the evolution of the lowest few cumulants of the velocity distribution (particle density, mean velocity, temperature, etc.); and kinetic models, which retain equations for the evolution of velocity distribution itself in a five- or six-dimensional phase space. Due to their lower dimensionality, the calculation of magnetohydrodynamic equilibria and large-scale stability tends to be much simpler in fluid models. However, because fluid models derive from the moments of the Boltzmann equation, which is nonlinear, they suffer from the well-known *closure problem*, which can be rigorously overcome only in certain asymptotic regimes. This difficulty complicates the inclusion of non-ideal effects in many cases.

There are two major objectives of the work presented here. The first is to develop methods for solving non-ideal fluid plasma models numerically. These non-ideal models include effects such as collisional, two-fluid, finite Larmor radius effects, as well as flows. The second objective is to show that these effects may have important consequences for the stability and transport properties of magnetized plasmas, even in cases where they are formally of small order. In particular, the effects of non-ideal processes on the stability of several instances of general stratified plasmas are considered, as are their

effects on the axisymmetric steady-states of tokamak plasmas.

1.2 Computational Plasma Physics

In many cases of physical interest, both fluid and kinetic models are analytically intractable due to their nonlinearity, and must be solved numerically. Obtaining such solutions poses significant challenges in many cases. These challenges are due in large part to the vast disparities in temporal and spatial scales present in the models. For instance, kinetic models describe both plasma oscillations and drift waves; in NSTX, these phenomena have frequencies of orders 10^{11} and 10^4 Hz, respectively. Thus a numerical solution resolving both phenomena would have to involve at least 10^7 time steps. In general, not all of these scales are of interest, and rapid fluctuations may be removed from the models by making certain assumptions. For example, gyrokinetic models exclude gyrofrequency-scale physics by averaging over the gyro-motion of particles; plasma oscillations may be excluded by the assumption of quasineutrality; electromagnetic waves are excluded by the omission of the displacement current in Ampère's law.

There are cases where effects which are important only on very small physical scales are crucial in determining the large-scale behavior. One important example of such a case in plasma physics is the tearing mode, where resistive effects in a small boundary layer cause the magnetic field to "reconnect" there, leading to topological changes in the magnetic field on large scales [14]. Furthermore, two-fluid effects, which may be important only within this boundary layer, may dramatically affect the rate of magnetic reconnection [15]. Thus, even if one is only interested in the large-scale behavior of the plasma, it is necessary to resolve the physics occurring in this thin boundary layer in order to obtain an accurate global solution.

In order to resolve these small scales the spatial discretization must be made finer, which causes two problems when calculating numerical solutions.

The first is simply that this increases the degrees of freedom present in the discretized equations, which raises the computational cost of the calculation. The second is that the Courant-Friedrich-Lewy (CFL) condition—the limit on the maximum stable explicit time step which may be taken—is proportional to the spatial discretization scale length δx divided by the phase velocity of the fastest wave in a hyperbolic system. This problem is made even worse by the presence of dispersive waves, such as the whistler wave, the phase velocity of which increases at smaller scales, resulting in a highly onerous restriction on the maximum explicit time step size as the spatial resolution is increased.

The solution to the first problem is to use a spatial discretization method which has variable resolution throughout the spatial domain. For structured meshes, this may be accomplished either by subdividing logical partitions of the mesh [16] or by loosening the coupling between the logical structure of the mesh and the physical coordinates [17]. The adaptation of structured meshes is somewhat limited due to the constraint of their logical structure. Use of an unstructured mesh allows mesh elements simply to be packed in regions where resolution is needed, regardless of the shape of those regions or the shape of the domain. This is the method employed by M3D-C^1, described in chapter 3.

The solution to the problem of the stability limit on explicit time stepping methods is to use an implicit method. A time-step method is considered *explicit* if the difference between the solutions at the next time step and the current time step is not a function of the solution at the next time step. *Implicit* methods, where that difference depend on (as yet unknown) values of the solution at the next time step, require obtaining a self-consistent solution to the discretized system of physical equations. This solution is typically obtained by linearizing the equations about the current solution, leading to a matrix equation which may be solved either by direct or iterative methods. This linearization may be applied iteratively, as in a Newton method, to ob-

tain a more accurate solution to the nonlinear equations. Implicit methods do not suffer from the highly restrictive CFL condition and may therefore allow much larger time steps than explicit methods. Even though an implicit time step may be significantly more computationally expensive than an explicit one, implicit methods may be more efficient if the CFL limit is significantly shorter than the time scales of interest.

The focus of this work is on fluid plasma models. Many numerical codes have been written for the solution of fluid plasma models, each employing different numerical methods and focusing on different physical models. Some modern codes for time-dependent, nonlinear, non-ideal models include CTD [18], M3D [19], NIMROD [20], and SEL [17]. A new implicit finite element code, M3D-C^1 [21], which employs a flux/potential scalar representation of the magnetic and velocity fields similar to that used in M3D, is exclusively used for the results obtained in this work.

1.3 Overview

The two-fluid model is derived from velocity moments of a system of Boltzmann equations in chapter 2. The closure problem inherent in such a system of moment equations is discussed, and some methods of closure are presented. In particular, the ideal MHD model and the Braginskii model are examined, as well as methods of extending the fluid equations beyond the short mean-free-path asymptotic regime.

In chapter 3, the numerical code M3D-C^1, developed for the solution of the time-dependent, nonlinear two-fluid equations, is presented. The numerical methods and techniques employed by M3D-C^1 are discussed. Several benchmarks are presented. Some of these benchmarks and methods for an earlier version of M3D-C^1 have been previously published by Ferraro and Jardin [21] and Jardin, Breslau, and Ferraro [22]; the content of chapter 3 extends this work to include significant enhancements to the numerical meth-

ods, including an unstructured mesh, toroidal geometry, a more complete physical model, and improvements to the time-stepping algorithm.

Applications in which linear stability may be significantly affected by non-ideal effects are presented in chapter 4. These applications include the stability of a magnetized plasma with an inverted density or temperature profile, which may be unstable to a Rayleigh-Taylor-like instability (gravitational instability), or the magnetothermal instability (MTI), respectively; and astrophysical accretion disks, which may be unstable to the magnetorotational instability (MRI). It is shown that the stability of these systems may be strongly affected by two-fluid effects or, in particular, finite Larmor radius (FLR) effects. The results regarding the gravitational instability have been published by Ferraro and Jardin [21], and those regarding the MRI were published by Ferraro [23].

Finally, M3D-C^1 is used to calculate the axisymmetric steady-states of plasma held in a magnetic configuration typical of NSTX. This is accomplished by time-integrating the two-fluid equations from an initial condition until steady-state is reached. Current is driven inductively. The self-consistent steady-state flows are examined and compared with analytic theory or comparable simulation results, where possible. Gyroviscosity is found to lead to toroidal rotation and oscillation; these effects are considered in some detail. This recent work is currently in preparation for publication.

Chapter 2

The Two-Fluid Model

2.1 Moment Equations

The basic equation describing the evolution of the probability distribution functions $f_s(\mathbf{x}, \mathbf{v}, t)$ of a collection of one or more species s of indistinguishable particles is a system of Boltzmann equations for each species:

$$\partial_t f_s + \partial_{\mathbf{x}} \cdot (\mathbf{v} f_s) + \partial_{\mathbf{v}} \cdot (\mathbf{a}_s f_s) = C_s + S_s. \tag{2.1}$$

In a basic model of a plasma in which the species are of immutable, electrically charged particles, the acceleration $\mathbf{a}_s$ may be due to electric or magnetic fields or other external forces $\mathbf{F}$ (such as gravity):

$$m_s \mathbf{a}_s = q_s \left(\mathbf{E} + \frac{\mathbf{v}}{c} \times \mathbf{B} \right) + \mathbf{F}_s, \tag{2.2}$$

where m_s is the particle mass, q_s is the particle charge, and c is the speed of light. The electric and magnetic fields may be due to electrical charge densities or currents within the plasma, or external sources, and evolve according to Maxwell's equations. The collision operator, $C_s = \sum_{s'} C_{ss'}$, represents effects arising from correlations between particles of species s and s', which include scattering due to classical collisions and turbulence [24]. External

sources of particles and heat are represented by S_s.

Equations for the evolution of thermodynamic quantities may be obtained by taking velocity moments of equation (2.1). The first three such moments represent conservation of particle number, momentum, and energy. Specifically, the moments are formed by operating on equation (2.1) with $\int d\mathbf{v}$, $\int d\mathbf{v}\ m_s\mathbf{v}$, and $\int d\mathbf{v}\ m_s v^2/2$, respectively.

$$\frac{\partial n_s}{\partial t} + \nabla \cdot (n_s \mathbf{u}_s) = \sigma_s, \tag{2.3a}$$

$$\frac{\partial}{\partial t}(m_s n_s \mathbf{u}_s) + \nabla \cdot (m_s n_s \mathbf{u}_s \mathbf{u}_s) + \nabla p_s + \nabla \cdot \mathsf{\Pi}_s = q_s n_s \left(\mathbf{E} + \frac{\mathbf{u}_s}{c} \times \mathbf{B}\right) + n_s \mathbf{F}_s + \mathbf{R}_s, \tag{2.3b}$$

$$\frac{\partial}{\partial t}\left(\frac{3}{2}p_s + \frac{1}{2}m_s n_s u_s^2\right) + \nabla \cdot \left(\frac{1}{2}m_s n_s u_s^2 \mathbf{u}_s + \frac{5}{2}p_s \mathbf{u}_s + \mathsf{\Pi}_s \cdot \mathbf{u}_s + \mathbf{q}_s\right) = (\mathbf{R}_s + n_s \mathbf{F}_s + q_s n_s \mathbf{E}) \cdot \mathbf{u}_s + Q_s + Q_{\Delta_s}. \tag{2.3c}$$

The density, fluid velocity, scalar pressure, stress tensor, and heat flux density are defined as:

$$n_s = \int d\mathbf{v}\ f_s, \tag{2.4a}$$

$$\mathbf{u}_s = \frac{1}{n_s}\int d\mathbf{v}\ \mathbf{v} f_s, \tag{2.4b}$$

$$p_s = \frac{1}{3}\int d\mathbf{v}\ m_s |\mathbf{v} - \mathbf{u}_s|^2 f_s, \tag{2.4c}$$

$$\mathsf{\Pi}_s = \left[\int d\mathbf{v}\ m_s (\mathbf{v} - \mathbf{u}_s)(\mathbf{v} - \mathbf{u}_s) f_s\right] - p_s \mathsf{I}, \tag{2.4d}$$

$$\mathbf{q}_s = \frac{1}{2}\int d\mathbf{v}\ m_s |\mathbf{v} - \mathbf{u}_s|^2 (\mathbf{v} - \mathbf{u}_s) f_s. \tag{2.4e}$$

The temperature is defined to be $T_s = p_s/n_s$. The collisional sources of

momentum density and heat density are defined as

$$\mathbf{R}_s = \sum_{s'} \int d\mathbf{v}\ m_s(\mathbf{v}-\mathbf{u}_s)C_{ss'}, \tag{2.5a}$$

$$Q_{\Delta_s} = \frac{1}{2}\sum_{s'} \int d\mathbf{v}\ m_s|\mathbf{v}-\mathbf{u}_s|^2 C_{ss'}. \tag{2.5b}$$

Collisions neither create nor destroy energy or momentum, but only transfer energy or momentum between species. Assuming these collisions to be local processes due to short-range forces, this conservation property requires

$$\sum_s \mathbf{R}_s = \sum_s Q_{\Delta_s} = 0. \tag{2.6}$$

Formally, the external sources of particles and heat density are

$$\sigma_s = \int d\mathbf{v}\ S_s, \tag{2.7a}$$

$$Q_s = \frac{1}{2}\int d\mathbf{v}\ m_s|\mathbf{v}-\mathbf{u}_s|^2 S_s. \tag{2.7b}$$

Consider now an electrically neutral system of two species, electrons and ions, with electron charge $q_e = -e$ and ion charge $q_i = Ze$, and masses m_e and m_i respectively, such that $Zm_e/m_i \ll 1$. On scales larger than the Debye length quasineutrality is well satisfied, so $n = n_e = Zn_i$. In order that quasineutrality remain satisfied in the presence of particle sources, it is required that the particle source be quasineutral, so $\sigma = \sigma_e = Z\sigma_i$.

Deviations from single-fluid motion are typically small on hydrodynamic scales in most fusion devices, which are much longer and slower than the ion gyroradius and ion cyclotron period. Therefore it is useful to combine the ion and electron equations of motion to yield a single equation of motion for the full plasma. This is typically accomplished by the following procedure:

- A change of variables is made from the electron and ion velocities,

$\mathbf{u}_e$ and $\mathbf{u}_i$, to the fluid (mass) velocity and current density, defined respectively as

$$\mathbf{u} = \frac{m_e n_e \mathbf{u}_e + m_i n_i \mathbf{u}_i}{m_e n_e + m_i n_i}; \quad \mathbf{J} = n_i q_i \mathbf{u}_i + n_e q_e \mathbf{u}_e.$$

- The ion fluid equation of motion is replaced by the total fluid equation of motion, which is the sum of the electron and ion fluid equations of motion.

- The electron fluid equation of motion may then be used to define the electric field, which does not appear in the total fluid equation of motion.

- Similarly, the ion pressure equation is replaced by the total pressure equation, which is the sum of the electron and ion pressure equations, divided by the sum of the ion and electron mass.

Due to the restrictions of equations (2.5), one may define $\mathbf{R} = \mathbf{R}_e = -\mathbf{R}_i$ and $Q_\Delta = Q_{\Delta e} = -Q_{\Delta i}$, which drop out of the total momentum and total pressure equations, respectively.

Terms of order Zm_e/m_i may be dropped. By specializing to certain regimes of interest, other terms may be shown always to be negligible. In particular, by considering only systems in which the speed of light is much greater than any characteristic speed of the system, the displacement current may be neglected in Ampère's law, which may then may be used as the definition of $\mathbf{J}$. Doing this imposes the restriction that $\nabla \cdot \mathbf{J} = 0$, exactly, end eliminates electromagnetic waves from the model. Furthermore, when considering time and length scales larger than the electron cyclotron period and Larmor radius, the electron inertia will be small compared to the Lorentz force and can be dropped from the electron equation of motion. After making

these approximations, the resulting equations are:

$$\frac{\partial n}{\partial t} + \nabla \cdot (n\mathbf{u}) = \sigma \tag{2.8a}$$

$$mn\left(\frac{\partial \mathbf{u}}{\partial t} + \mathbf{u} \cdot \nabla \mathbf{u}\right) = \frac{\mathbf{J} \times \mathbf{B}}{c} - \nabla p - \nabla \cdot \Pi + n\mathbf{F} - \sigma \mathbf{u} \tag{2.8b}$$

$$\begin{aligned} \frac{3}{2}\left[\frac{\partial p}{\partial t} + \nabla \cdot (p\mathbf{u})\right] &= -p\nabla \cdot \mathbf{u} - \frac{3}{2}\left(\frac{5}{3}p_e\frac{\nabla n}{n} - \nabla p_e\right) \cdot \frac{\mathbf{J}}{ne} \\ &\quad - \Pi : \nabla \mathbf{u} + \Pi_e : \nabla \frac{\mathbf{J}}{ne} - \nabla \cdot \mathbf{q} \\ &\quad + \frac{1}{2}\sigma m u^2 - n\mathbf{F} \cdot \mathbf{u} + (n\mathbf{F}_e + \mathbf{R}) \cdot \frac{\mathbf{J}}{ne} + Q \end{aligned} \tag{2.8c}$$

$$\begin{aligned} \frac{3}{2}\left[\frac{\partial p_e}{\partial t} + \nabla \cdot (p_e\mathbf{u})\right] &= -p_e\nabla \cdot \mathbf{u} - \frac{3}{2}\left(\frac{5}{3}p_e\frac{\nabla n}{n} - \nabla p_e\right) \cdot \frac{\mathbf{J}}{ne} \\ &\quad - \Pi_e : \nabla\left(\mathbf{u} - \frac{\mathbf{J}}{ne}\right) - \nabla \cdot \mathbf{q}_e \\ &\quad - (n\mathbf{F}_e + \mathbf{R}) \cdot \left(\mathbf{u} - \frac{\mathbf{J}}{ne}\right) + Q_\Delta + Q_e \end{aligned} \tag{2.8d}$$

$$\mathbf{E} + \frac{\mathbf{u} \times \mathbf{B}}{c} = \frac{1}{ne}\left(\frac{\mathbf{J} \times \mathbf{B}}{c} - \nabla p_e - \nabla \cdot \Pi_e + n\mathbf{F}_e + \mathbf{R}\right) \tag{2.8e}$$

$$\frac{\partial \mathbf{B}}{\partial t} = -c\nabla \times \mathbf{E} \tag{2.8f}$$

$$\mathbf{J} = \frac{c}{4\pi}\nabla \times \mathbf{B} \tag{2.8g}$$

where $m = (m_i n_i + m_e n_e)/n \approx m_i/Z$, $p = p_i + p_e$, $\Pi = \Pi_i + \Pi_e$, $\mathbf{q} = \mathbf{q}_i + \mathbf{q}_e$, $Q = Q_i + Q_e$, and $\mathbf{F} = (n_i\mathbf{F}_i + n_e\mathbf{F}_e)/n$.

2.2 Closure and Transport Coefficients

Equations (2.8) are not a closed set of equations because the quantities Π, Π_e, $\mathbf{R}$, $\mathbf{q}$, $\mathbf{q}_e$, and Q_Δ are undetermined (ignoring the issue of external sources). In principle, these quantities may be determined by higher moments of equation (2.1). However, each moment of equation (2.1) will introduce a quantity

which is determined by the next-higher moment, and therefore in principle it is necessary to evaluate an infinite number of moments in order to retain all the information of the Boltzmann equation. This is the well-known closure problem. This problem can be overcome by appealing to kinetic theory. In certain asymptotic regimes, the closures take relatively simple forms, in which case the resulting fluid equations retain a significant advantage over the full kinetic system.

In particular, the closure relations may be written as (spatially) local functions of the thermodynamic and magnetic fields in the limit of short mean-free-path ($kv_{ts} \ll \nu_s$) or small gyro-radius and short parallel mean-free-path ($k_\perp \rho_s \ll 1$ and $k_\parallel v_{ts} \ll \nu_s$). (Here $v_{ts} = \sqrt{T_s/m_s}$ is the thermal velocity of species s, ν_s is the collision frequency, $\rho_s = v_{ts}/\omega_{cs}$ is the Larmor radius, and $\omega_{cs} = q_s B/m_s c$ is the cyclotron frequency.) It is typical to term plasmas satisfying the short mean-free-path condition "collisional," and those satisfying the small gyro-radius condition "magnetized." The behavior of unmagnetized plasmas may be very different than that of magnetized plasmas due to the strong anisotropic transport properties of magnetized plasmas. With the possible exception of hot fusion products, the plasma in most magnetic fusion reactors is well magnetized, and so here the unmagnetized limit will not be considered. However, due to the strong temperature dependence of the collision frequency, the core of a fusion plasma is collisionless, whereas the colder edge region is (typically) collisional; therefore both collisionality limits are of interest here.

2.2.1 Ideal MHD

The most basic closure is to set all unknown quantities to zero. This "truncation" of the moment equations, together with the omission of the two-fluid terms in equations (2.8c) and (2.8e), yields the ideal-MHD equations, which model a perfectly conducting, inviscid, adiabatic plasma. Ideal-MHD is valid in the highly collisional, strongly magnetized plasma limit, where the mean-

free-path and gyro-radius are small compared to all length scales present in the system, on timescales short compared to dissipative (resistive, viscous) timescales.

The major advantage of ideal-MHD is its simplicity. The ideal-MHD equations, linearized about a stationary equilibrium, may be cast into variational form [25],

$$\int dV\, mn \left(\frac{\partial \xi}{\partial t}\right)^2 - \int dV\, \xi \cdot \mathcal{L}_{MHD}(\xi) = 0 \tag{2.9}$$

where the linear displacement perturbation ξ is defined by $\mathbf{u} = \partial\xi/\partial t$, and

$$\mathcal{L}_{MHD}(\xi) = \frac{c}{4\pi}[\nabla \times \nabla \times (\xi \times \mathbf{B})] \times \mathbf{B} + \frac{c}{4\pi}(\nabla \times \mathbf{B}) \times [\nabla \times (\xi \times \mathbf{B})] + \nabla\left(\xi \cdot \nabla p + \frac{5}{3} p \nabla \cdot \xi\right). \tag{2.10}$$

The two terms of equation (2.9) are the perturbations to the kinetic and potential energies, respectively. In this form, the question of the stability of an equilibrium becomes a minimization problem for the potential energy; a negative perturbation to the potential energy indicates a positive perturbation to the kinetic energy and hence, linear instability. This formulation therefore represents a powerful and relatively simple method of determining the stability of ideal-MHD equilibria. However, it is only possible to cast the equations in the form of equation (2.9) because $\mathcal{L}$ is self-adjoint. The introduction of dissipative terms, for example, leads to a non-Hamiltonian system of equations for which an energy principle is not applicable.

2.2.2 Braginskii Equations

Closures more sophisticated than truncation may be obtained by appealing to the kinetic equations. In a collisional plasma, one may apply the Chapman-Enskog procedure to obtain correction equations for perturbations to the

distribution function expanded in some small parameter (typically the collisionality and magnetization parameters) [26]. This method requires that deviation of the distribution function from a Maxwellian (the solution to the zeroth-order equation) to be relatively small, and so its applicability is strictly valid only in the high-collisionality limit. Using this method, local asymptotic expressions for the thermodynamic force/flux relations depending only on the thermodynamic and magnetic fields may be obtained, thus solving the closure problem. This was carried out by Braginskii [27] using the Landau form of the collision operator. Toroidally confined fusion plasmas in this asymptotic regime are said to be in the "Pfirsch-Schlüter" regime.

Of some relevance to the results presented in later chapters are the gyroviscous and parallel viscous stresses, which are briefly described below. These stresses represent corrections to the ideal-MHD equations to include the lowest order effects of finite Larmor orbits and pressure anisotropy. If the electrons and ions in a plasma have similar temperatures and velocity scale lengths, the ratio of the electron to ion collisional parallel viscosity is $\nu_i/\nu_e \sim \sqrt{m_e/m_i}$; the ratio of electron to ion gyroviscosity is $\omega_{ci}/\omega_{ce} \sim m_e/m_i$; and the ratio of electron to ion collisional perpendicular viscosity is $\omega_{ci}^2\nu_e/\omega_{ce}^2\nu_i \sim (m_e/m_i)^{3/2}$. Therefore the ion viscous forces are generally dominant over the electron viscous forces.

Gyroviscosity

The gyroviscosity is defined as the components of the stress tensor $\mathsf{\Pi}$ which do not depend on the collision frequency. These components form a tensor, $\mathsf{\Pi}_\wedge$, which represents the FLR corrections to the fluid equations to lowest order in the magnetization parameter $\delta = \rho_s/L_0 \ll 1$. The form of $\mathsf{\Pi}_\wedge$ in the "fast" or "MHD" ordering used by Braginskii, which assumes that $u_s \sim v_{ts}$ and $\partial_t \sim \delta\,\omega_{cs}$ [28], is (for either species s)

$$\mathsf{\Pi}_{\wedge s} = \frac{p_s}{4\omega_{cs}} \left\{ \mathbf{b} \times \mathsf{W}_s \cdot (\mathsf{I} + 3\mathbf{bb}) + [\mathbf{b} \times \mathsf{W}_s \cdot (\mathsf{I} + 3\mathbf{bb})]^\top \right\}, \tag{2.11}$$

where the rate-of-strain tensor is

$$\mathsf{W}_s = \nabla \mathbf{u}_s + (\nabla \mathbf{u}_s)^\top - \frac{2}{3}\,\mathsf{I}\,\nabla \cdot \mathbf{u}_s. \tag{2.12}$$

In the "drift" ordering in which $u_s \sim \delta\, v_{ts}$ and $\partial_t \sim \delta^2 \omega_{cs}$, it is necessary to modify this form to include the effects of the heat flux gradient in addition to the velocity gradient [29]. The expression for the gyroviscous stress becomes significantly more complicated when extended to allow strongly anisotropic pressure [30]. The gyroviscosity is independent of the collision frequency, and retains the same form in all collisionality regimes.

Gyroviscous Cancellation The Braginskii form of the gyroviscous force may be written [30]

$$\begin{aligned} \nabla \cdot \mathsf{\Pi}_{\wedge s} \;=\; & -m_s n_s \mathbf{u}_* \cdot \nabla \mathbf{u}_s - \nabla \alpha_s \\ & - \nabla \times \left\{ \frac{p_s}{\omega_{cs}} \left[\mathbf{a}_s + \frac{1}{2} \left(\nabla \cdot \mathbf{u} - 3\mathbf{b} \cdot \mathbf{a}_s \right) \mathbf{b} \right] \right\} \\ & + \mathbf{B} \cdot \nabla \left\{ \frac{p_s}{\omega_{cs}} \mathbf{b} \times \left[3\mathbf{a}_s + \mathbf{b} \times \varpi_s \right] + \frac{\alpha_s}{B} \mathbf{b} \right\}, \end{aligned} \tag{2.13}$$

where

$$\mathbf{a}_s = \mathbf{b} \cdot \nabla \mathbf{u}_s \tag{2.14a}$$

$$\varpi_s = \nabla \times \mathbf{u}_s \tag{2.14b}$$

$$\alpha_s = \frac{p_s}{2\omega_{cs}} \mathbf{b} \cdot \varpi_s \tag{2.14c}$$

$$\mathbf{u}_{*s} = -\frac{1}{m_s n_s} \nabla \times \left(\frac{p_s}{\omega_{cs}} \mathbf{b} \right). \tag{2.14d}$$

A common approximation is to retain only the first term of equation (2.13), which is valid in the limit of vanishing parallel gradients. The equation of

motion for a species s may then be written (neglecting collisional forces)

$$m_s n_s \left(\frac{\partial \mathbf{u}_s}{\partial t} + (\mathbf{u}_s - \mathbf{u}_{*s}) \cdot \nabla \mathbf{u}_s \right) = n_s q_s \left(\mathbf{E} + \frac{\mathbf{u}_s \times \mathbf{B}}{c} \right) - \nabla p_s. \tag{2.15}$$

Typically, the further approximation is made of replacing $\mathbf{u}_{*s}$, the "magnetization velocity," with the diamagnetic velocity, $-\nabla p_s \times \mathbf{b}/n_s m_s \omega_{cs}$. This illustrates the "gyroviscous cancellation" effect: the cancellation of the advection of momentum due to the fluid magnetization velocity (or diamagnetic drift) by gyroviscosity.

A simple, and possibly novel, explanation for this cancellation is as follows. The perpendicular fluid velocity may be obtained by neglecting inertia in the perpendicular component of equation (2.15). Thus

$$\mathbf{u}_s \approx u_{\parallel_s} \mathbf{b} + c \frac{\mathbf{E} \times \mathbf{B}}{B^2} - \frac{\nabla p_s \times \mathbf{b}}{n_s m_s \omega_{cs}} \tag{2.16}$$

Braginskii has shown [27] that the drift velocity of guiding center motion, averaged over a Maxwellian distribution, can be written as

$$\langle \mathbf{v}_{cs} \rangle = u_{\parallel_s} \mathbf{b} + c \frac{\mathbf{E} \times \mathbf{B}}{B^2} + v_{ts}^2 \nabla \times \left(\frac{\mathbf{b}}{\omega_{cs}} \right) \tag{2.17}$$

and that the difference of the fluid and guiding center drifts is therefore

$$\mathbf{u}_s - \langle \mathbf{v}_{cs} \rangle \approx -\frac{1}{m_s n_s} \nabla \times \left(\frac{p_s}{\omega_{cs}} \mathbf{b} \right) = \mathbf{u}_{*s}. \tag{2.18}$$

Thus the difference between the fluid velocity and the guiding center motion is approximately the magnetization velocity. Braginskii used this fact to argue that the difference between fluxes calculated using the fluid and guiding center drifts is purely due to considerations at the boundary, since the integral over any surface or volume of equation 2.18 may be converted to an integral over the corresponding boundary via Stokes' theorem. However,

equation (2.18) also suggests a physical explanation of gyroviscous cancellation effect: namely, that the momentum flux represented by $m_s n_s \mathbf{u}$ is advected by the motion of the guiding centers $\langle \mathbf{v}_c \rangle$, and not by the fluid velocity $\mathbf{u}$. This is made clearer by using equation (2.18) to write equation (2.15) as

$$m_s n_s \left(\frac{\partial \mathbf{u}_s}{\partial t} + \langle \mathbf{v}_{cs} \rangle \cdot \nabla \mathbf{u}_s \right) = n_s q_s \left(\mathbf{E} + \frac{\mathbf{u}_s \times \mathbf{B}}{c} \right) - \nabla p_s. \tag{2.19}$$

It should be noted that similar relation holds for the pressure equation. In the Braginskii ordering, the component of $\mathbf{q}$ which is independent of the collision frequency is

$$\mathbf{q}_{\wedge s} = \frac{5}{2} \frac{n_s v_{ts}^2}{\omega_{cs}} \mathbf{b} \times \nabla T_s \tag{2.20}$$

Again, Braginskii shows that

$$\frac{5}{2} p_s \mathbf{u}_s + \mathbf{q}_{\wedge s} = \frac{5}{2} p_s \langle \mathbf{v}_{cs} \rangle - \nabla \times \left(\frac{5}{2} \frac{p_s v_{ts}^2}{\omega_{cs}} \mathbf{b} \right), \tag{2.21}$$

where the left-hand-side appears in the total heat flux in equation (2.3c). Therefore

$$\nabla \cdot \left(\frac{5}{2} p_s \mathbf{u}_s + \mathbf{q}_{\wedge s} \right) = \nabla \cdot \left(\frac{5}{2} p_s \langle \mathbf{v}_{cs} \rangle \right). \tag{2.22}$$

Thus $\mathbf{q}_\wedge$ acts to cancel the artificial convection of heat by fluid drifts which are not particle drifts, in a way analogous to the gyroviscous cancellation effect.

Parallel Viscosity

By definition, the parallel viscosity contains effects which regulate the parallel transport of parallel momentum. Again considering the collisional limit, the parallel viscosity takes the form

$$\Pi_{\parallel s} = \frac{\eta_{0s} p_s}{2\nu_s} \left(\mathbf{b} \cdot \mathsf{W}_s \cdot \mathbf{b} \right) \left(\mathsf{I} - 3\mathbf{b}\mathbf{b} \right) \tag{2.23}$$

where $\eta_{0i} \approx 0.96$ and $\eta_{0e} \approx 0.73$ [27], and W_s is the rate-of-strain tensor defined by equation (2.12). Essentially, this describes the diffusion of momentum along the magnetic field lines. In the collisional limit, this diffusion is due to a random walk along the field line having a "step size" equal to the mean-free-path $\lambda_s = v_{ts}/\nu_s$ and "step frequency" equal to the collision frequency ν_s, thus yielding a diffusion coefficient $\sim \lambda_s^2 \nu_s/2 = v_{ts}^2/2\nu_s$ (and hence a viscosity of $\sim m_s n_s v_{ts}^2/2\nu_s = p_s/2\nu_s$). Note that the diffusion constant becomes infinite in the limit $\nu_s \to 0$, and therefore must break down in low collisionality regimes.

The parallel viscosity is related to deviations from pressure isotropy. In the model of Chew, Goldberger, and Low (CGL) [31], the pressure tensor is taken to be diagonal, but with separate scalar pressures for the parallel and perpendicular directions:

$$\mathsf{P}_s = p_s \mathsf{I} + \frac{1}{3}(p_{\perp s} - p_{\parallel s})(\mathsf{I} - 3\mathbf{bb}) \tag{2.24}$$

$$= p_s \mathsf{I} + \mathsf{\Pi}_{CGLs}, \tag{2.25}$$

where $p_s = (p_{\parallel s} + 2p_{\perp s})/3$. Note that $\mathsf{\Pi}_{CGLs}$ has the same tensor structure as $\mathsf{\Pi}_{\parallel s}$, with

$$p_{\perp s} - p_{\parallel s} = \frac{3}{2}\frac{\eta_{0s} p_s}{\nu_s}\mathbf{b} \cdot \mathsf{W}_s \cdot \mathbf{b}. \tag{2.26}$$

Magnetic Pumping One important physical effect contained in the collisional form of the parallel viscosity is "magnetic pumping" [32]. This effect occurs when plasma is convected through a region of higher magnetic field. When entering such a region, the perpendicular pressure of the plasma rises due to the conservation of the magnetic moment of each particle. The pressure quickly and irreversibly isotropizes (in the collisional regime), raising the entropy at the expense of the kinetic energy in the plasma flow.

In a tokamak, the main effect of magnetic pumping is to damp the poloidal flow as it carries plasma through the poloidally varying magnetic field. The

true effect of a large collisional parallel viscosity is to reduce the magnitude of $\mathbf{b}\cdot\mathsf{W}\cdot\mathbf{b}$, in order that the term $-\Pi_{\parallel} : \nabla\mathbf{u} = 3\mu_{\parallel}(\mathbf{b}\cdot\mathsf{W}\cdot\mathbf{b}/2)^2$ becomes small enough to reach balance with the other terms in the pressure equation. (This can also be understood by noting that entropy production of the parallel viscosity is proportional to $-\Pi_{\parallel} : \nabla\mathbf{u}$.) In the same way, the effect of a large parallel thermal conductivity is to reduce the magnitude of $\mathbf{b}\cdot\nabla T$.

2.2.3 Long Mean-Free-Path Effects

The Coulomb collision time of a charged particle with energy T scales as $T^{3/2}$, and so as a plasma is heated, collisions become less frequent. Once the short mean-free-path condition is violated, the fluid description becomes significantly more complex. Because particles may travel a relatively large distance along the magnetic field in this regime before thermalizing, the transport coefficients are inherently nonlocal. The flux-averaged theory of these coefficients has been worked out in some detail; see the review by Hirshman and Sigmar [33], for example.

Magnetic Trapping An important effect which is not correctly treated by collisional closures is magnetic trapping. Magnetic trapping occurs when the conservation of energy and the magnetic moment exclude a particle orbit from a region of high magnetic field, causing its path to reflect from that region. At the point of reflection, the particle's parallel velocity is zero and the perpendicular velocity is maximized, and therefore one expects pressure anisotropies there. In the long mean-free-path regime, the pressure is not rapidly isotropized, and a trapped particle may bounce between regions of strong magnetic fields many times before collisions lead to scattering of its pitch angle sufficient for detrapping.

In neoclassical theory, the "banana regime" is defined by the condition that the detrapping frequency is less than the bounce frequency of trapped particles [34]. The transport properties in this regime differ somewhat from

the those in the collisional Pfirsch-Schlüter regime. Furthermore, important effects due to the interaction between trapped and passing particles arise. In particular, the bootstrap current is an effect which arises from such an interaction, and may be responsible for a significant fraction of the total plasma current in tokamaks.

Since trapping effects are necessarily described by pressure anisotropy, one approach to extending fluid models to include them is to evolve the parallel and perpendicular pressures separately [31, 35, 36, 28, 37]. This approach requires additional closures for the parallel and perpendicular heat flux density, and therefore does not solve the closure problem *per se*, though closures for this model have been obtained [31, 35]. However, even truncation of this fluid scheme, which gives the double-adiabatic theory of Chew Goldberger and Low, obtains magnetic trapping effects (though the condition of adiabaticity is generally not well satisfied in the collisionless limit). Another approach is to retain a single (isotropic) scalar pressure, and to modify the parallel viscosities to include the effects of pressure anisotropy [38]. This approach is perhaps easier from the standpoint of calculating stationary states, as the anisotropy is of course not changing in such state and so the extra dynamical equation for the anisotropy may be eliminated without introducing time-dependent contributions to the viscosity.

As noted above, trapping effects are inherently nonlocal, and rigorous closures must reflect that. Analytic expressions for these closures are generally given in terms of surface-averaged values of thermodynamic fluxes [33]. However, the poloidal dependence of these stresses is important in certain applications; for example, neoclassical tearing modes depend on the local perturbations to the bootstrap current resulting from local changes in the pressure gradient. Closures which are local in space have been devised for such purposes, but these are only approximate and not rigorously correct in any asymptotic limit [39].

Landau Damping Another issue arising in the collisionless limit is wave-particle interactions whereby particles having velocities resonant with waves in the system may exchange energy with those waves. This is not captured by collisional closures because collisions act quickly to move particles out of resonance and maintain a Maxwellian distribution in the collisional regime. These wave-particle interactions are important for damping out certain waves having phase velocities close to typical (thermal) particle velocities, such as the ion acoustic wave. The inverse effect—where particles excite waves resonant with their velocity—may also lead to instabilities, such as with the toroidal Alfvén eigenmode instability.

In the fluid picture, Landau damping does not lead to the direct thermalization of energy (as with collisional damping), but rather to the transfer of energy from lower to higher fluid moments *ad infinitum* [40]. Despite being a reversible processes, this damping can not be recovered though the introduction of non-dissipative fluid closures, and can only be exactly modeled in a set of fluid equations by the retention of an infinite number of moments [41]; a fluid model of Landau damping is therefore necessarily only an approximation. Landau-fluid models have been developed to approximate the effect of Landau damping by introducing an artificial parallel damping term in the highest fluid moment equation [40, 35]. The closures involved in the Landau-fluid model are local in wavenumber, as opposed to configuration space, and may be interpreted as a reduction in the parallel viscosity due to an enhanced collision rate—enhanced by "collisions" with perturbations in the electric or magnetic fields [42]. (An interesting illustration of this fact is the comparison of the calculation of linear growth rate of the magnetorotational instability from the Landau-fluid perspective [42, 43] and the Braginskii perspective [44].) Early Landau-fluid models overestimated the damping of axisymmetric Rosenbluth-Hinton flows, which are not damped by collisionless processes [45, 46]; however, modifications to the Landau-fluid closures were subsequently made to mitigate these errors [36].

2.2.4 Turbulent Transport

Many fluid closures, including those of Braginskii, are derived under the assumption of strong magnetization, where perturbations on the scale of the gyro-radius are negligible. Micro-instabilities, defined as instabilities at scale lengths such that $k_\perp \rho \gtrsim 1$, are therefore excluded from these models. Micro-instabilities are thought to be important to the transport properties of magnetically confined plasmas, as they may form convective eddies which efficiently transport energy across magnetic surfaces.

It is possible to construct fluid models which allow $k_\perp \rho \lesssim 1$. One method, which has been used particularly to study edge plasma turbulence [47], is to expand the fluid equations in the drift ordering. One may also carry out the Chapman-Enskog procedure on the Boltzmann equation to higher order in the small parameter $k_\perp \rho$, to improve the accuracy as $k_\perp \rho \to 1$ [48]. Another method is to build a fluid model with the appropriate closures based on moments of the gyrokinetic equations, which are valid for $k_\perp \rho_i \sim 1$, to yield the gyro-fluid equations [41, 49]. Still another technique is to replace the collisional transport coefficients in the two-fluid equations with values from transport models based either on inference from kinetic simulations (such as TGLF [50]), or from experiments. While this technique lacks the rigor of a unified model, it may be more useful for obtaining results on hydrodynamic timescales because turbulent fluctuations need not be resolved.

Finally, there are numerous other issues which are not naturally included in the version of the two-fluid framework discussed above, but which may be important in fusion plasmas. Among these are the issues of ionization and multiple charge states, impurities, thermal fluctuations, radiation (either from electronic transitions or bremsstrahlung), and plasma-wall interactions. Some of these effects may be handled by allowing more than two species (multiple charge states, impurities); others are more efficiently incorporated at a phenomenological level than with a comprehensive unified physical theory, due to the vast disparities of the scales on which they occur with the

hydrodynamic scales of interest.

Chapter 3

The M3D-C^1 Numerical Code

3.1 Overview

M3D-C^1 is a numerical code for the time-integration of the nonlinear two-fluid equations. This code has been designed with the purpose of obtaining solutions on both MHD and transport timescales, with the physics associated with both timescales accurately and self-consistently included.

The equations implemented in M3D-C^1, which are nearly the complete Braginskii equations described in chapter 2, are given in dimensionless vector form in section 3.2. The numerical methods employed by M3D-C^1, including the time-integration and spatial discretization techniques, are described in section 3.3. Ongoing efforts in the extension of M3D-C^1 to allow three-dimensional linear stability analysis are described in section 3.5.

3.2 Physical Equations

M3D-C^1 equations (2.8) in dimensionless form, normalized to an arbitrary characteristic density n_0, magnetic field strength B_0, and scale length L_0. All quantities in this chapter are normalized in this way, unless otherwise noted.

The implemented equations are:

$$\frac{\partial n}{\partial t} + \nabla \cdot (n\mathbf{u}) = \Sigma \tag{3.1a}$$

$$n\left(\frac{\partial \mathbf{u}}{\partial t} + \mathbf{u} \cdot \nabla \mathbf{u}\right) = \mathbf{J} \times \mathbf{B} - \nabla p - \nabla \cdot \Pi + \mathbf{F} - \Sigma \mathbf{u} \tag{3.1b}$$

$$\begin{aligned} \frac{1}{\Gamma - 1}\left[\frac{\partial p}{\partial t} + \nabla \cdot (p\mathbf{u})\right] &= -p\nabla \cdot \mathbf{u} - \nabla \cdot \mathbf{q} - \Pi : \nabla \mathbf{u} + \frac{1}{2}\Sigma u^2 \\ &\quad + d_i\left(\frac{n\nabla T_e}{\Gamma - 1} - T_e \nabla n + \mathbf{R}\right) \cdot \frac{\mathbf{J}}{n} + d_i \Pi_e : \nabla \frac{\mathbf{J}}{n} \end{aligned} \tag{3.1c}$$

$$\begin{aligned} \frac{1}{\Gamma - 1}\left[\frac{\partial p_e}{\partial t} + \nabla \cdot (p_e\mathbf{u})\right] &= -p_e\nabla \cdot \mathbf{u} - \nabla \cdot \mathbf{q}_e + Q_\Delta \\ &\quad + d_i\left(\frac{n\nabla T_e}{\Gamma - 1} - T_e \nabla n + \mathbf{R}\right) \cdot \frac{\mathbf{J}}{n} + d_i \Pi_e : \nabla \frac{\mathbf{J}}{n} \end{aligned} \tag{3.1d}$$

$$\frac{\partial \mathbf{B}}{\partial t} = -\nabla \times \mathbf{E} \tag{3.1e}$$

$$\mathbf{J} = \nabla \times \mathbf{B} \tag{3.1f}$$

$$\mathbf{E} + \mathbf{u} \times \mathbf{B} = \frac{d_i}{n}\left(\mathbf{J} \times \mathbf{B} - \nabla p_e - \nabla \cdot \Pi_e + \mathbf{R}\right) \tag{3.1g}$$

where $d_i = c/L_0\omega_{pi}$ (in cgs units) is the normalized collisionless ion skin depth, and $\omega_{pi} = \sqrt{4\pi n_0 e^2/m_i}$ (also in cgs units) is the characteristic ion plasma frequency. The ratio of specific heats Γ has been introduced in equations (3.1c) and (3.1d); $\Gamma = 5/3$ recovers equations (2.8c) and (2.8d), whereas $\Gamma = 1$ yields an isothermal equation of state. Here and henceforth it is assumed that $Z = 1$, so that $n_i = n_e = n$.

The closures implemented in M3D-C^1 mostly take the Braginskii [27] form, which are appropriate for collisional plasmas. Descriptions of the closures implemented in M3D-C^1 are given below. The choice to use collisional closures is motivated by the difficulty of implementing the nonlocal closures typical of plasmas in the long mean-free-path regime.

3.2.1 Thermodynamic Forces

Friction

The collisional force term $\mathbf{R}$ represents the transfer of momentum from one species to another through collisions. Due to conservation of total momentum, this term does not appear in equation (2.8b). The collisional force implemented in M3D-C^1 is the frictional force in the Braginskii closure

$$\mathbf{R} = \frac{1}{d_i} n\eta \mathbf{J}. \tag{3.2}$$

The resistivity η is left as an arbitrary scalar field. Note that $\mathbf{R}$ contains a factor of d_i^{-1}, and is therefore remains present (and finite) in equation (3.1g) in the limit that $d_i \to 0$. This term is responsible for the Joule heating of the plasma. The thermal force is not implemented.

Viscosity

The viscosity in M3D-C^1 is implemented as the sum of three parts,

$$\mathsf{\Pi} = \mathsf{\Pi}_{\parallel} + \mathsf{\Pi}_{\wedge} + \mathsf{\Pi}_{\circ} \tag{3.3}$$

where $\mathsf{\Pi}_{\parallel}$ takes the form of the collisional ion parallel viscosity, $\mathsf{\Pi}_{\wedge}$ is the Braginskii ion gyroviscosity, $\mathsf{\Pi}_{\circ}$ is a generic isotropic viscosity. Since the collisional perpendicular viscosity is smaller than the collisional parallel viscosity by a factor of $(\nu/\omega_c)^2 \ll 1$, the isotropic viscosity may accurately be used in place of the more complicated perpendicular viscosity.

$$\mathsf{\Pi}_{\parallel} = \frac{\mu_{\parallel}}{2} (\mathbf{b} \cdot \mathsf{W} \cdot \mathbf{b}) (\mathsf{I} - 3\mathbf{bb}) \tag{3.4a}$$

$$\mathsf{\Pi}_{\wedge} = d_i \frac{p_i}{4} \left\{ \mathbf{b} \times \mathsf{W} \cdot (\mathsf{I} + 3\mathbf{bb}) + [\mathbf{b} \times \mathsf{W} \cdot (\mathsf{I} + 3\mathbf{bb})]^{\top} \right\} \tag{3.4b}$$

$$\mathsf{\Pi}_{\circ} = -\mu \left(\nabla \mathbf{u} + \nabla \mathbf{u}^{\top} \right) - 2 (\mu_c - \mu) \ \mathsf{I} \ \nabla \cdot \mathbf{u}. \tag{3.4c}$$

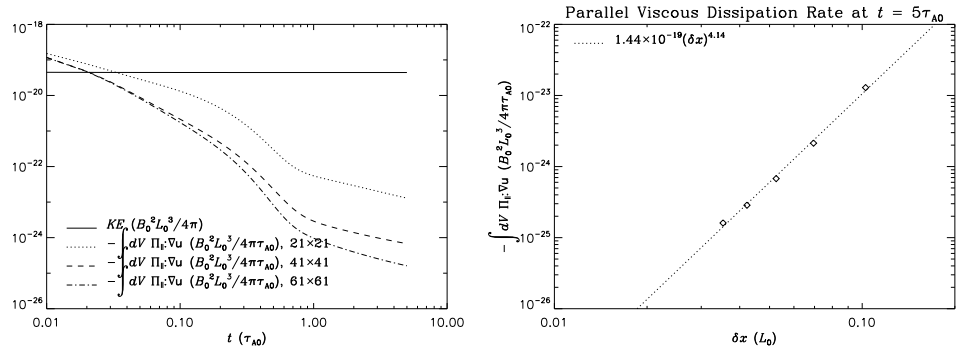

Figure 3.1: *Left*: Evolution of the total kinetic energy and the rate of parallel viscous damping in the magnetostatic test case, for various mesh resolutions. The rate of damping rapidly drops before significantly affecting the kinetic energy (which is due almost entirely to poloidal flows). *Right*: Rate of damping at $t = \tau_{A0}$ versus the mesh resolution δx.

The coefficients $\mu_\parallel$, μ, and μ_c are left as arbitrary scalar fields. Note that μ_c only damps compressional motion. The viscosities are constrained by the positivity requirements $\mu_c > \frac{2}{3}\mu$ and $\mu > 0$.

As a test of the implementation of the parallel viscous term in M3D-C^1, linear simulations have been run, initialized in the same NSTX-like GS equilibrium as the other simulations, but given a very small initial poloidal rotation ($\sim 10^{-10} v_{A0}$). The system is then evolved keeping density, pressure, and the magnetic field constant (*i.e.* only the momentum equation is evolved). The results of this test are shown in figure 3.1. It is found that $(\mathbf{b}\cdot\mathsf{W}\cdot\mathbf{b})^2$ rapidly drops several orders of magnitude, as expected from the argument given in section 2.2.2. The kinetic energy (which is due at all times almost entirely to poloidal flows) is found not to damp significantly; this is because the toroidal angular velocity is not constrained to remain constant within magnetic surfaces in the absence of Ohm's law in this test case. This demonstrates that the implementation of the parallel viscosity damps $\mathbf{b}\cdot\mathsf{W}\cdot\mathbf{b}$, as it should, but not simply by damping the kinetic energy.

Electron Viscosity

The electron stress tensor is taken to have the form

$$\Pi_e = \lambda n \nabla \mathbf{J}, \tag{3.5}$$

which has roughly the form of an isotropic electron viscosity. Its inclusion in equation (3.1g) leads to a biharmonic operator on the magnetic field, which may be called a "hyper-resistivity," and the above form is chosen specifically to yield this effect. This term has the effect of rapidly smoothing high-k frequencies while leaving lower frequencies relatively unaffected. Presently this term is included to improve numerical stability. In some nonlinear reconnection regimes, its inclusion is necessary to avoid mathematical singularity at the x-point.

Heat Flux Density

The heat flux densities are taken to have the collisional form

$$\mathbf{q} = -\kappa_\circ \nabla T - \kappa_\wedge \mathbf{B} \times \nabla T - \kappa_\parallel \mathbf{b}\mathbf{b} \cdot \nabla T \tag{3.6}$$

$$\mathbf{q}_e = -\kappa_\circ \nabla T_e - \kappa_\wedge \mathbf{B} \times \nabla T_e - \kappa_\parallel \mathbf{b}\mathbf{b} \cdot \nabla T_e. \tag{3.7}$$

The transport coefficients $\kappa_\circ$, $\kappa_\wedge$, and $\kappa_\parallel$ are left as arbitrary scalar fields.

Collisional Heat Transfer

The heat transferred from ions to electrons through collisions is

$$Q_\Delta = 3\frac{m_e}{m_i}\nu_e(p_i - p_e). \tag{3.8}$$

3.2.2 External Sources

Particles

The term Σ is taken to have the form

$$\Sigma = \sigma + D_n \nabla^2 n \tag{3.9}$$

where σ is an arbitrary quasineutral particle density source/sink field. The scalar D_n is an "anomalous" diffusion coefficient which both provides numerical stability and allows for the phenomenological modeling of enhanced rates of particle transport due to micro-turbulent effects not resolved in the MHD and transport-scale simulations considered here, such as ion temperature gradient modes.

Momentum

An external force of the form

$$\mathbf{F} = -\frac{1}{R^2} g_R \nabla R - g_Z \nabla Z \tag{3.10}$$

is implemented in M3D-C^1 which may be used to impose either a constant downward gravitational acceleration, or a radial gravitational acceleration which falls off as $1/R^2$. The corresponding external force on the electrons is proportional to the electron mass and is dropped from equations (3.1d) and (3.1g).

3.3 Numerical Methods

3.3.1 Finite Elements

Reduced quintic finite elements are used in M3D-C^1. These elements are triangular, fifth-order bivariate polynomial elements, constrained to enforce

continuity of values and first-derivatives across element boundaries (this is the C^1 property). These finite elements have the advantage of having only three degrees of freedom per node per field asymptotically [51], which leads to a highly compact matrix representation of the discretized equations.

The discretized equations are obtained by application of the Galerkin method. In this method, the equations are projected onto the space of finite elements by taking their inner product with each finite element. For example, the physical equation

$$\frac{\partial \nabla^2 U}{\partial t} = \mu \nabla^2 (\nabla^2 U) \tag{3.11}$$

is discretized into the system of equations obtained by representing U as a linear combination of the basis functions $\{\nu\}$,

$$U(\mathbf{x}, t) = \sum_j U_j(t) \nu_j(\mathbf{x}), \tag{3.12}$$

and integrating over the computational domain:

$$\frac{\partial U_j}{\partial t} \int dA \; \nu_i \nabla^2 \nu_j = U_j \int dA \; \nu_i \nabla^2 (\mu \nabla^2 \nu_j). \tag{3.13}$$

This is the discretized "weak form" of equation (3.11). Thus an equation of infinite dimension (equation (3.11) applies at each point in the domain) is discretized into a finite set of one-dimensional equations for each combination of ν_i and U_j. One advantage of the weak form is that equations having high-order derivatives can be transformed using integrations-by-parts. For example, equation (3.13) becomes

$$-\frac{\partial U_j}{\partial t} \int dA \; \nabla \nu_i \cdot \nabla \nu_j = U_j \int dA \; \mu \nabla^2 \nu_i \nabla^2 \nu_j. \tag{3.14}$$

Due to the C^1 property of the reduced quintic elements, the second derivative of the finite element representation of any field remains well-defined even at element boundaries, and so equation (3.14) may be computed directly.

Therefore, physical equations containing up to fourth derivatives may be computed directly using C^1 elements. In contrast, in the case of C^0 elements, for which only the first derivative is well-defined at element boundaries, the calculation of this equation would require the introduction of a new equation to define an auxiliary variable $\varpi = \nabla^2 U$, *e.g.*,

$$\begin{aligned} \varpi_j \int dA\ \nu_i \nu_j &= -U_j \int dA\ \nabla\nu_i \cdot \nabla\nu_j. \\ \frac{\partial U_j}{\partial t} \int dA\ \nabla\nu_i \cdot \nabla\nu_j &= \varpi_j \int dA\ \nabla\nu_i \cdot \nabla(\mu\nu_j) \end{aligned}$$

For an implicit time step, these two equations would have to be solved simultaneously in a single matrix equation, thereby doubling the rank of the matrix.

Spatial Integration

In M3D-C^1, the spatial integrations are now carried out numerically, not analytically as in previous work [52, 21]. (Analytic integrations, while competitive computationally when using a structured mesh in Cartesian geometry, are not feasible on an unstructured mesh in toroidal geometry where the Jacobian of each finite element is potentially different.) The numerical integration is done using a Gaussian quadrature, where the integral (over an individual element) is replaced by a weighted sum:

$$\int dA\ F \approx A \sum_{p=1}^{N_p} w_p F(\mathbf{x}_p) \tag{3.15}$$

where A is the area of the triangle, and $\mathbf{x}_p$ and w_p are an appropriately chosen set of sampling points and associated weights. The quadratures implemented in M3D-C^1use the weights and sampling points published by Dunavant [53].

Dunavant gives the sampling points $\{\mathbf{x}_p\}$ as a set of points in the "natural" coordinates of a triangle, (α, β, γ), where $\alpha = A_1/A$, $\beta = A_2/A$, and

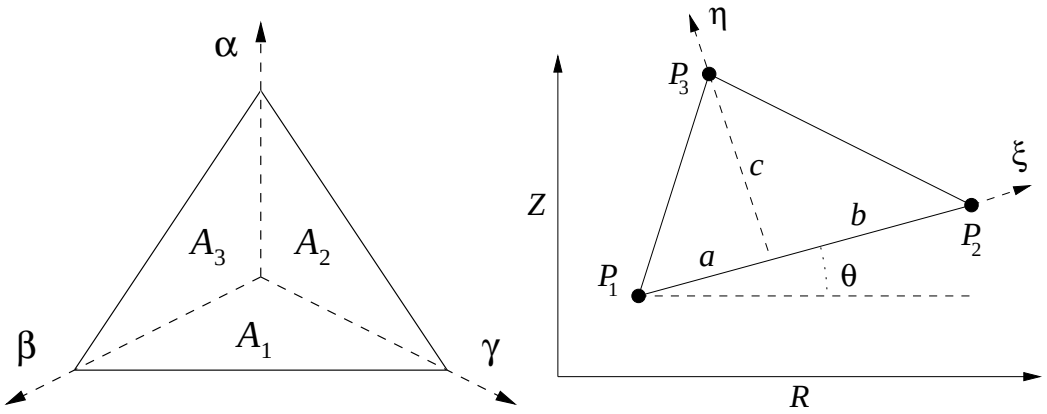

Figure 3.2: *Left*: The "natural" coordinate system of an equilateral triangle, (α, β, γ). *Right*: The local coordinate system on a finite element triangle used in M3D-C^1, (ξ, η).

$\gamma = A_3/A$, with the areas A_1, A_2, and A_3 as shown in figure 3.2. These coordinates may be converted to the standard form of the local coordinate system used on triangular elements by M3D-C^1, (ξ, η) by the linear transformation:

$$(\xi, \eta) = \left(\frac{1}{2} \left[(a+b)(\beta - \gamma) + (a-b)(1-\alpha) \right], c\alpha \right). \tag{3.16}$$

The area of the triangle is given simply by

$$A = \frac{1}{2}(a+b)c. \tag{3.17}$$

The most accurate quadrature implemented in M3D-C^1 uses 79 sampling points ($N_p = 79$). This quadrature is exact for polynomials of up to degree 25, and is therefore exact for discretized nonlinear products of up to four fields when represented using the reduced quintic elements (the integrand being the product of four fields and one basis function, each represented by a degree-five polynomial). The 25-point quadrature, though not exact for highly nonlinear terms, is found to be accurate even for relatively coarse meshes. The fractional mean differences between the kinetic energy time

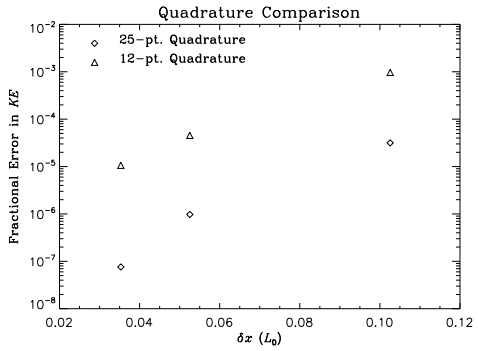

Figure 3.3: The fractional error in the kinetic energy, as calculated by $\langle |E_n - E_{79}| \rangle_t \,/\, \langle E_{79} \rangle_t$, is plotted for $n = 25$ and $n = 12$ for various element sizes δx. Here, E_n is the kinetic energy time series of a simulation using n-point integration quadrature, and $\langle \cdot \rangle_t$ indicates the time-average.

series obtained with the 79-point quadrature and those obtained with the 25-point and 12-point quadratures are shown in figure 3.3. The test case is a typical NSTX simulation with $\eta_0 = 10^{-4}$ (see chapter 5), run for 500 Alfvén times. The error introduced by the lower-order quadratures is small compared to the truncation error introduced by spatial discretization, which is on the order of a few percent for typical mesh resolutions used in the NSTX simulations. The truncation error is shown for the same case in figure 3.4.

Unstructured Mesh

The mesh of triangular elements in M3D-C^1 is fully unstructured, meaning that the index of the element is not in any way dependent on the position or orientation of the element. This differs from a logically rectangular mesh, for example, in which each element has a fixed number of neighbors (except at the boundaries), and in which each element's position and orientation is determined by some simple function of its logical indices. By eliminating these constraints, an unstructured mesh gains the following advantages:

1. any finite domain may be easily meshed, regardless of boundary shape;

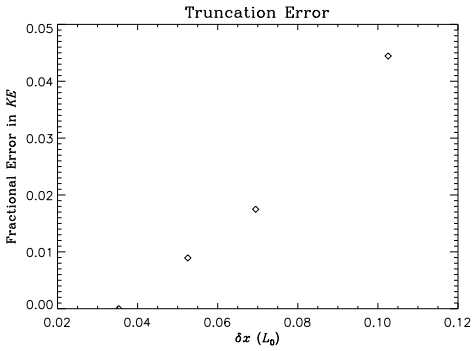

Figure 3.4: The fractional error in the kinetic energy due to truncation from spatial discretization, as calculated by $\left\langle |E(\delta x) - E_(\delta x_0)| \right\rangle_t / \left\langle E(\delta x_0) \right\rangle_t$ is plotted for various element sizes δx. Here $\delta x_0 \approx 0.035 L_0$, and $\langle \cdot \rangle_t$ indicates the time-average. These cases were run using the 79-point integration quadrature.

2. it is relatively simple to pack resolution in boundary layers of any shape and orientation; and

3. mesh adaptation in response to the development of boundary layers may be more aggressive.

The disadvantages of an unstructured mesh are that it is costly to determine in which element a particular spatial point falls, and that some care must be taken to avoid large changes in the size and aspect ratio of neighboring mesh elements. For the simulation of physical phenomena in which the position of a boundary layer is fixed and known *a priori*, a static mesh with resolution packed near the boundary layer works well to reduce the computational cost of obtaining a solution, without significantly reducing the accuracy.

A prime example of this type of phenomenon in plasma physics is magnetic reconnection. Magnetic reconnection is process whereby magnetic flux is transported across a magnetic surface (the "separatrix"). In the ideal MHD model, this process is prohibited by the "frozen-in" constraint of the ideal Ohm's law. However, resistive effects break this constraint within a

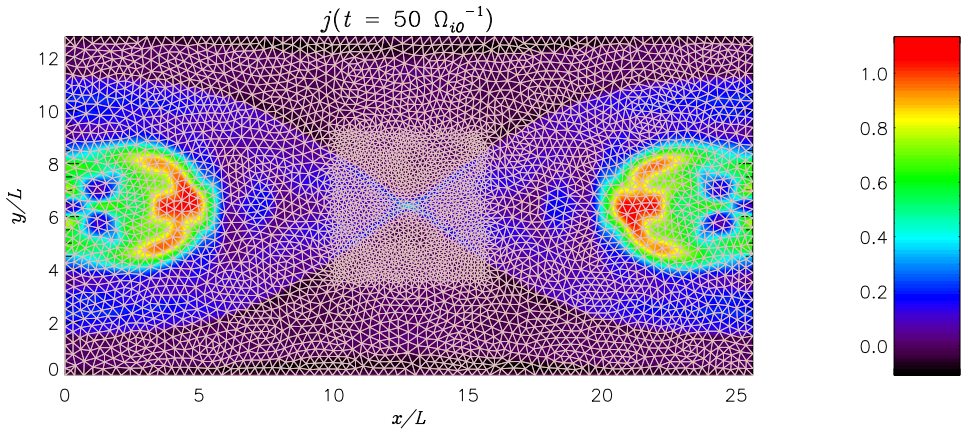

Figure 3.5: A simple example of a packed mesh, overlaying a plot of toroidal current density in the late stages of a reconnection simulation. The high-resolution area has a resolution equivalent to a 121×121 node structured mesh; the outer region has a resolution equivalent to a 61×61 node structured mesh.

thin resistive boundary layer, and allow reconnection to occur. It has been found that this layer collapses even further in two-fluid models [15], to a so-called "x-point" or "x-line." The rate at which reconnection occurs depends sensitively on the conditions in this boundary layer, and so that region must be well resolved for simulations to be accurate. If this small region is not well resolved, the large-scale solution over much of the domain will not be accurate. With an unstructured mesh, it is easy to pack resolution near the highly localized x-point without increasing the resolution elsewhere, where it is not needed. In this way, the accuracy of the solution may be increased without significantly increasing the computational cost of its calculation. Examples of M3D-C^1 simulation results employing this strategy are shown in figures 3.5 and 3.6.

The distribution of an unstructured mesh and the associated data structures onto multiple processors for the purpose of parallel computation is

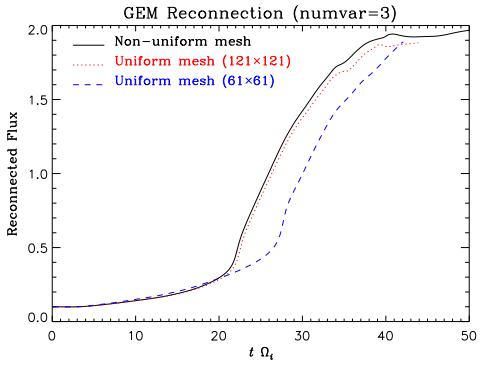

Figure 3.6: The total reconnected flux from reconnection simulations run using a a uniform mesh of 121 × 121 nodes, 61 × 61 nodes, and the non-uniform mesh shown in figure 3.5.

somewhat more difficult than the domain decomposition of a logical mesh. This is because in an unstructured mesh, the connectivity of elements cannot be inferred from their indices, and also because it may be challenging to decompose the mesh into contiguous domains of roughly equal numbers of elements while also ensuring that the boundaries between domains (which incur costs associated with inter-process communication) are as small as possible. Mesh generation, refinement, and distributed data structures are handled through software developed for M3D-C^1 by SCOREC at RPI. The mesh partitioning is done using ParMETIS [54], through Zoltan [55, 56].

3.3.2 Linear Semi-Implicit Time Step

In order to overcome the restrictive stability limits of explicit time-steps, M3D-C^1 employs an implicit time stepping method. Implicit methods can be computationally costly because they involve the calculating the solution of matrix equations which may involve a large number of unknowns. The computational cost may be reduced by re-writing the large matrix equation in which all quantities are advanced together as several smaller matrix equations in which the velocity, density, pressure, and magnetic field are advanced

separately. It is possible to do this while still retaining the stability properties of an implicit method. The semi-implicit method employed by M3D-C^1 described below, is closely related to the semi-implicit methods of Harned and Schnack [57] and Caramana [58]. These are methods of "parabolizing" a hyperbolic system of equations, transforming a large, ill-conditioned system of equations into a set of smaller, better-conditioned ones [59].

Velocity Advance

First, the momentum equation is evaluated at the θ-advanced time (*i.e.* $\mathbf{u} \rightarrow u + \theta\delta t\dot{\mathbf{u}}$, etc.) and terms of order δt^2 are dropped.

$$\begin{aligned} n\left[\frac{\partial \mathbf{u}}{\partial t} + \mathbf{u}\cdot\nabla\mathbf{u} + \theta\delta t(\dot{\mathbf{u}}\cdot\nabla\mathbf{u} + \mathbf{u}\cdot\nabla\dot{\mathbf{u}})\right] = \\ (\nabla\times\mathbf{B})\times\mathbf{B} - \nabla p + n\mathbf{g} - \nabla\cdot\Pi(\mathbf{u}) - \sigma\mathbf{u} \\ + \theta\delta t\left[(\nabla\times\dot{\mathbf{B}})\times\mathbf{B} + (\nabla\times\mathbf{B})\times\dot{\mathbf{B}} - \nabla\dot{p} + \dot{n}\mathbf{g} - \nabla\cdot\Pi(\dot{\mathbf{u}}) - \sigma\dot{\mathbf{u}}\right] \end{aligned} \tag{3.18}$$

Equations (2.8a),(2.8c), and (2.8f) are evaluated with the θ-advanced $\mathbf{u}$:

$$\frac{\partial n}{\partial t} = -\nabla\cdot(n\mathbf{u}) - \theta\delta t\nabla\cdot(n\dot{\mathbf{u}}) + \Sigma_n \tag{3.19}$$

$$\frac{\partial \mathbf{B}}{\partial t} = \nabla\times(\mathbf{u}\times\mathbf{B}) + \theta\delta t\nabla\times(\dot{\mathbf{u}}\times\mathbf{B}) + \Sigma_B \tag{3.20}$$

$$\frac{\partial p}{\partial t} = -\mathbf{u}\cdot\nabla p - \Gamma p\nabla\cdot\mathbf{u} - \theta\delta t(\dot{\mathbf{u}}\cdot\nabla p + \Gamma p\nabla\cdot\dot{\mathbf{u}}) + \Sigma_p, \tag{3.21}$$

where

$$\begin{aligned} \Sigma_n &= \sigma + D_n\nabla^2 n \\ \Sigma_B &= -\nabla\times\left[\eta\mathbf{J} + \frac{d_i}{n}(\mathbf{J}\times\mathbf{B} - \nabla p_e - \nabla\cdot\Pi_e)\right] \\ \Sigma_p &= d_i\left[n\nabla T_e + (\Gamma-1)(\mathbf{R} - T_e\nabla n)\right]\cdot\frac{\mathbf{J}}{n} + (\Gamma-1)\left(d_i\Pi_e : \nabla\frac{\mathbf{J}}{n} - \nabla\cdot\mathbf{q}\right). \end{aligned}$$

Now $\dot{n}$, $\dot{\mathbf{B}}$ and $\dot{p}$ in equation (3.18) may be eliminated using equations (3.19)–

(3.21).

$$
\begin{aligned}
n\left[\frac{\partial \mathbf{u}}{\partial t} + \mathbf{u}\cdot\nabla\mathbf{u} + \theta\delta t(\dot{\mathbf{u}}\cdot\nabla\mathbf{u} + \mathbf{u}\cdot\nabla\dot{\mathbf{u}})\right] = \\
(\nabla\times\mathbf{B})\times\mathbf{B} - \nabla p - \nabla\cdot\mathsf{\Pi}(\mathbf{u}) + n\mathbf{g} - \sigma\mathbf{u} \\
+ \theta\delta t\left[\mathcal{L}(\mathbf{u}) + \theta\delta t\mathcal{L}(\dot{\mathbf{u}}) - \nabla\cdot\mathsf{\Pi}(\dot{\mathbf{u}}) - \sigma\dot{\mathbf{u}}\right]
\end{aligned}
\tag{3.22}
$$

where

$$
\begin{aligned}
\mathcal{L}(\mathbf{u}) = [\nabla\times\nabla\times(\mathbf{u}\times\mathbf{B})]\times\mathbf{B} + (\nabla\times\mathbf{B})\times[\nabla\times(\mathbf{u}\times\mathbf{B})] \\
+ \nabla(\mathbf{u}\cdot\nabla p + \Gamma p\nabla\cdot\mathbf{u}) - \nabla\cdot(n\mathbf{u})\mathbf{g}.
\end{aligned}
\tag{3.23}
$$

Note that $\mathcal{L}$ is simply the ideal MHD operator defined by equation (2.10), aside from the gravitational term which is not present in ideal-MHD. Now letting $\dot{\mathbf{u}} = (\mathbf{u}^{n+1} - \mathbf{u}^n)/\delta t$ (where the superscripts index the time step),

$$
\begin{aligned}
n\left[\mathbf{u}^{n+1} + \theta\delta t(\mathbf{u}^{n+1}\cdot\nabla\mathbf{u}^n + \mathbf{u}^n\cdot\nabla\mathbf{u}^{n+1})\right] \\
+ \theta\delta t[\nabla\cdot\mathsf{\Pi}(\mathbf{u}^{n+1}) + \sigma\mathbf{u}^{n+1}] - \theta^2\delta t^2\mathcal{L}(\mathbf{u}^{n+1}) = \\
n\left[\mathbf{u}^n - (1-2\theta)\delta t\mathbf{u}^n\cdot\nabla\mathbf{u}^n\right] \\
+ \delta t[(\nabla\times\mathbf{B}^n)\times\mathbf{B}^n - \nabla p^n + n^n\mathbf{g}] \\
- (1-\theta)\delta t[\nabla\cdot\mathsf{\Pi}(\mathbf{u}^n) + \sigma\mathbf{u}^n] + (1-\theta)\theta\delta t^2\mathcal{L}(\mathbf{u}^n).
\end{aligned}
\tag{3.24}
$$

This discretization has the problem that the terms proportional to $\mathcal{L}$ do not cancel in steady-state (see section 3.4.1). This can be fixed by the method of Caramana [58], which is simply to subtract $\theta\delta t^2\mathcal{L}(\mathbf{u}^n)$ from the right hand side of equation (3.24). This has the effect of removing a numerical dissipation term from the discretized equations. The resulting discretization

for velocity is then

$$\begin{aligned} & n^n \left[\mathbf{u}^{n+1} + \theta\delta t(\mathbf{u}^{n+1}\cdot\nabla\mathbf{u}^n + \mathbf{u}^n\cdot\nabla\mathbf{u}^{n+1})\right] \\ & \quad + \theta\delta t[\nabla\cdot\Pi(\mathbf{u}^{n+1}) + \sigma\mathbf{u}^{n+1}] - \theta^2\delta t^2\mathcal{L}(\mathbf{u}^{n+1}) = \\ & \quad n^n\left[\mathbf{u}^n - (1-2\theta)\delta t\mathbf{u}^n\cdot\nabla\mathbf{u}^n\right] \\ & \quad + \delta t[(\nabla\times\mathbf{B}^n)\times\mathbf{B}^n - \nabla p^n + n^n\mathbf{g}] \\ & \quad - (1-\theta)\delta t[\nabla\cdot\Pi(\mathbf{u}^n) + \sigma\mathbf{u}^n] - \theta^2\delta t^2\mathcal{L}(\mathbf{u}^n). \end{aligned} \tag{3.25}$$

which may be solved independently of the equations for $\mathbf{B}$, n, and p, since the only advanced-time variable it contains is $\mathbf{u}^{n+1}$.

It is convenient to write equation (3.25) in the form:

$$\begin{aligned} & V_{\mathbf{u}n}(\mathbf{u}^{n+1}, n^n) - \theta\delta t\left[\begin{array}{l} V_{\mathbf{uu}n}(\mathbf{u}^{n+1},\mathbf{u}^n,n^n) + V_{\mathbf{uu}n}(\mathbf{u}^n,\mathbf{u}^{n+1},n^n) \\ \quad + V_{\mathbf{u}\Pi}(\mathbf{u}^{n+1}) + V_{\mathbf{uu}\sigma}(\mathbf{u}^{n+1}) \end{array}\right] \\ & \qquad - \theta^2\delta t^2\mathcal{L}(\mathbf{u}^{n+1}) = \\ & V_{\mathbf{u}n}(\mathbf{u}^n, n^n) + (1-2\theta)\delta t V_{\mathbf{uu}n}(\mathbf{u}^n,\mathbf{u}^n,n^n) \\ & \qquad + (1-\theta)\delta t\left[V_{\mathbf{u}\Pi}(\mathbf{u}^n) + V_{\mathbf{uu}\sigma}(\mathbf{u}^n)\right] \\ & \qquad + \delta t\left[V_{\mathbf{BB}}(\mathbf{B}^n,\mathbf{B}^n) + V_p(p^n) + V_{n\mathbf{g}}(n^n)\right] \\ & \qquad - \theta^2\delta t^2\mathcal{L}(\mathbf{u}^n). \end{aligned} \tag{3.26}$$

$$\begin{aligned} V_{\mathbf{u}n}(\mathbf{u},n) &= n\mathbf{u} \\ V_{\mathbf{uu}n}(\mathbf{u},\mathbf{u},n) &= -n\mathbf{u}\cdot\nabla\mathbf{u} \\ V_{\mathbf{u}\Pi}(\mathbf{u}) &= -\nabla\cdot\Pi(\mathbf{u}) \\ V_{\mathbf{uu}\sigma}(\mathbf{u}) &= -\sigma\mathbf{u} \\ V_{\mathbf{BB}}(\mathbf{B},\mathbf{B}) &= (\nabla\times\mathbf{B})\times\mathbf{B} \\ V_p(p) &= -\nabla p \\ V_{n\mathbf{g}}(n) &= n\mathbf{g} \end{aligned} \tag{3.27}$$

Density Advance

The density equation, which is coupled only to the velocity, may now be solved implicitly since the advanced-time velocity is known. Taylor expanding n and $\mathbf{u}$ in the density equation, dropping terms of order δt^2, and discretizing yields:

$$\begin{aligned} N_n(n^{n+1}) - \theta\delta t \left[N_{n\mathbf{u}}(n^{n+1},\mathbf{u}^n) + N_{n\mathbf{u}}(n^n,\mathbf{u}^{n+1}) + N_{nD_n}(n^{n+1})\right] = \\ N_n(n^n) + (1-2\theta)\delta t N_{n\mathbf{u}}(n^n,\mathbf{u}^n) + (1-\theta)\delta t N_{nD_n}(n^n) + \delta t N_\sigma \end{aligned} \tag{3.28}$$

$$\begin{aligned} N_n(n) &= n \\ N_{n\mathbf{u}}(n,\mathbf{u}) &= -\nabla\cdot(n\mathbf{u}) \\ N_\sigma &= \sigma \\ N_{nD_n}(n) &= D_n\nabla^2 n \end{aligned} \tag{3.29}$$

Pressure Advance

Similarly, the pressure advance is found by taking the θ-advanced $\mathbf{u}$ and p fields and discretizing:

$$\begin{aligned} P_p(p^{n+1}) - \theta\delta t \left[\begin{array}{l} P_{p\mathbf{u}}(p^{n+1},\mathbf{u}^n) + P_{p\mathbf{u}}(p^n,\mathbf{u}^{n+1}) \\ + P_{\mathbf{uu}\sigma}(\mathbf{u}^{n+1},\mathbf{u}^n) + P_{\mathbf{uu}\sigma}(\mathbf{u}^n,\mathbf{u}^{n+1}) \\ + P_{p\kappa}(p^{n+1}) \end{array}\right] = \\ P_p(p^n) + (1-2\theta)\delta t\left[P_{p\mathbf{u}}(p^n,\mathbf{u}^n) + P_{\mathbf{uu}\sigma}(\mathbf{u}^n,\mathbf{u}^n)\right] \\ + (1-\theta)\delta t\left[P_{p\kappa}(p^n)\right] \\ + \delta t\left[P_{p_e\mathbf{B}}(p_e^n,\mathbf{B}^n) + P_{\mathbf{BB}\eta}(\mathbf{B}^n,\mathbf{B}^n) + P_{\mathbf{B}\Pi_e}(\mathbf{B}^n) + P_{\mathbf{u}\Pi}(\mathbf{u}^n)\right] \end{aligned} \tag{3.30}$$

$$
\begin{aligned}
P_p(p) &= p \\
P_{p\mathbf{u}}(p,\mathbf{u}) &= -\mathbf{u}\cdot\nabla p - \Gamma p\nabla\cdot\mathbf{u} \\
P_{p_e\mathbf{B}}(p_e,\mathbf{B}) &= d_i\left[\tfrac{1}{n}\nabla p_e + \Gamma p_e\nabla\tfrac{1}{n}\right]\cdot\nabla\times\mathbf{B} \\
P_{\mathbf{BB}\eta}(\mathbf{B},\mathbf{B}) &= \eta(\nabla\times\mathbf{B})\cdot(\nabla\times\mathbf{B}) \\
P_{\mathbf{B}\Pi_e}(\mathbf{B}) &= (\Gamma-1)d_i\Pi_e : \nabla\left(\tfrac{1}{n}\nabla\times\mathbf{B}\right) \\
P_{p\kappa}(p,n) &= (\Gamma-1)\nabla\cdot\left[\left(\kappa_\circ + \kappa_\wedge\mathbf{B}\times + \kappa_\parallel\mathbf{bb}\cdot\right)\nabla\left(\tfrac{p}{n}\right)\right] \\
P_{\mathbf{uu}\sigma}(\mathbf{u},\mathbf{u}) &= \tfrac{1}{2}(\Gamma-1)\sigma\mathbf{u}\cdot\mathbf{u} \\
P_{\mathbf{u}\Pi}(\mathbf{u}) &= -(\Gamma-1)\Pi : \nabla\mathbf{u}
\end{aligned}
\tag{3.31}
$$

Note that for this advance, $\mathbf{B}$, p_e, and n appear but are not evaluated at the θ-advanced time. This allows the pressure to be advanced independently after the velocity advance, at the expense of some terms (electron convection, $P_{p_e\mathbf{B}}$, and ohmic heating, $P_{\mathbf{BB}\eta}$) not being treated implicitly. The viscous- and electron-viscous heating terms ($P_{\mathbf{u}\Pi}$ and $P_{\mathbf{B}\Pi_e}$) are treated explicitly because they contain spatial derivatives of higher than fourth order (see section 3.3.1).

Magnetic field and Electron Pressure Advance

The electron pressure and magnetic field advance equations are calculated using the θ-advanced values for $\mathbf{B}$, $\mathbf{u}$, and p_e, and therefore must be solved together. This is done to ensure that the kinetic Alfvén wave is treated implicitly.

$$
\begin{aligned}
P_p(p_e^{n+1}) - \theta\delta t\left[\begin{array}{l} P_{p\mathbf{u}}(p_e^{n+1},\mathbf{u}^n) + P_{p\mathbf{u}}(p_e^n,\mathbf{u}^{n+1}) \\ + P_{\mathbf{BB}\eta}(\mathbf{B}^{n+1},\mathbf{B}^n) + P_{\mathbf{BB}\eta}(\mathbf{B}^n,\mathbf{B}^{n+1}) \\ + P_{p_e\mathbf{B}}(p_e^{n+1},\mathbf{B}^n) + P_{p_e\mathbf{B}}(p_e^n,\mathbf{B}^{n+1}) \\ + P_{p\kappa}(p_e^{n+1}) \end{array}\right] = \\
P_p(p_e^n) + (1-2\theta)\delta t\left[P_{p\mathbf{u}}(p_e^n,\mathbf{u}^n) + P_{\mathbf{BB}\eta}(\mathbf{B}^n,\mathbf{B}^n) + P_{p_e\mathbf{B}}(p_e^n,\mathbf{B}^n)\right] \\
+ (1-\theta)\delta t\left[P_{p\kappa}(p_e^n)\right] \\
+ \delta t P_{\mathbf{B}\Pi_e}(\mathbf{B}^n)
\end{aligned}
\tag{3.32}
$$

$$
\begin{aligned}
P_p(p) &= p \\
P_{p\mathbf{u}}(p,\mathbf{u}) &= -\mathbf{u}\cdot\nabla p - \Gamma p\nabla\cdot\mathbf{u} \\
P_{p_e\mathbf{B}}(p_e,\mathbf{B}) &= d_i\left[\tfrac{1}{n}\nabla p_e + \Gamma p_e\nabla\tfrac{1}{n}\right]\cdot\nabla\times\mathbf{B} \\
P_{\mathbf{BB}\eta}(\mathbf{B},\mathbf{B}) &= \eta(\nabla\times\mathbf{B})\cdot(\nabla\times\mathbf{B}) \\
P_{\mathbf{B}\Pi_e}(\mathbf{B}) &= (\Gamma-1)d_i\Pi_e : \nabla\left(\tfrac{1}{n}\nabla\times\mathbf{B}\right) \\
P_{p\kappa}(p,n) &= (\Gamma-1)\nabla\cdot\left[\left(\kappa_\circ + \kappa_\wedge\mathbf{B}\times + \kappa_\parallel\mathbf{bb}\cdot\right)\nabla\left(\tfrac{p}{n}\right)\right] \\
P_{\mathbf{uu}\sigma}(\mathbf{u},\mathbf{u}) &= \tfrac{1}{2}(\Gamma-1)\sigma\mathbf{u}\cdot\mathbf{u} \\
P_{\mathbf{u}\Pi}(\mathbf{u}) &= -(\Gamma-1)\Pi : \nabla\mathbf{u}
\end{aligned}
\tag{3.33}
$$

$$
\begin{aligned}
B_{\mathbf{B}}(\mathbf{B}^{n+1}) - \theta\delta t\left[\begin{array}{l} B_{\mathbf{Bu}}(\mathbf{B}^{n+1},\mathbf{u}^n) + B_{\mathbf{Bu}}(\mathbf{B}^n,\mathbf{u}^{n+1}) \\ \quad + B_{\mathbf{BB}}(\mathbf{B}^{n+1},\mathbf{B}^n) + B_{\mathbf{BB}}(\mathbf{B}^n,\mathbf{B}^{n+1}) \\ \quad + B_{\mathbf{B}\eta}(\mathbf{B}^{n+1}) + B_{p_e}(p_e^{n+1}) + B_{\mathbf{B},\Pi_e}(\mathbf{B}^{n+1}) \end{array}\right] = \\
B_{\mathbf{B}}(\mathbf{B}^n) + (1-2\theta)\delta t\left[B_{\mathbf{Bu}}(\mathbf{B}^n,\mathbf{u}^n) + B_{\mathbf{BB}}(\mathbf{B}^n,\mathbf{B}^n)\right] \\
+ (1-\theta)\delta t\left[B_{\mathbf{B}\eta}(\mathbf{B}^n) + B_{p_e}(p_e^n) + B_{\mathbf{B},\Pi_e}(\mathbf{B}^n)\right]
\end{aligned}
\tag{3.34}
$$

$$
\begin{aligned}
B_{\mathbf{B}}(\mathbf{B}) &= \mathbf{B} \\
B_{\mathbf{Bu}}(\mathbf{B},\mathbf{u}) &= \nabla\times(\mathbf{u}\times\mathbf{B}) \\
B_{\mathbf{B}\eta}(\mathbf{B}) &= -\nabla\times(\eta\nabla\times\mathbf{B}) \\
B_{\mathbf{BB}}(\mathbf{B},\mathbf{B}) &= -d_i\nabla\times\left[\tfrac{1}{n}(\nabla\times\mathbf{B})\times\mathbf{B}\right] \\
B_{p_e}(p_e) &= d_i\nabla\times\left(\tfrac{1}{n}\nabla p_e\right) \\
B_{\mathbf{B}\Pi_e}(\mathbf{B}) &= d_i\nabla\times\left[\tfrac{1}{n}\nabla\cdot\Pi_e(\mathbf{B})\right]
\end{aligned}
\tag{3.35}
$$

Iteration of Magnetic Field Advance It is found that, for low values of resistivity, when ohmic heating, strongly anisotropic thermal conductivity, and flow are included, this method may be nonlinearly unstable at unacceptably small values of δt. The instability is characterized by temperature becoming negative in the core region. This limitation may be overcome by iterating the magnetic field advance. Specifically, after the magnetic field is advanced, the transport coefficients (η, κ, μ) are recalculated, and the magnetic field advance is redone using the new transport coefficients and the old

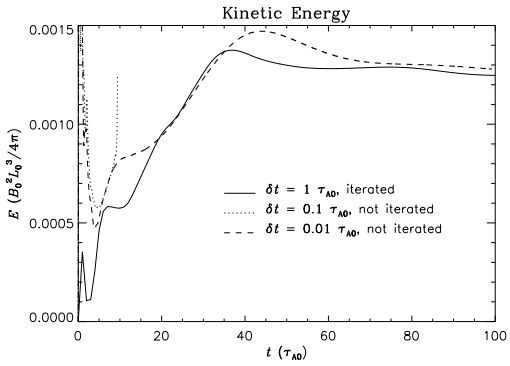

Figure 3.7: The time evolution of the kinetic energy in an NSTX simulation for various values of δt. In this case, the method without iterating the field-solve is stable for $\delta t = 0.01\tau_{A0}$, but not for $\delta t = 0.1\tau_{A0}$. When the field-solve iteration is used, $\delta t = \tau_{A0}$ is stable.

velocity and field values. This may reduce the time-accuracy of the timestep, but has no effect on the steady-state. A single iteration of this type increases the computational cost of a time step by roughly 50%, but may improve the maximum stable time step by several orders of magnitude. Figure 3.7 shows that the iteration method raises the maximum value of $\delta t/\tau_{A0}$ from $\mathcal{O}(10^{-2})$ to $\mathcal{O}(1)$, for a typical NSTX case (see section 5).

Scalar Representation

Equations (3.26), (3.28), (3.32), (3.34) constitute the discretized equations to be solved each time step. To solve these equations, a coordinate system and scalar representation for $\mathbf{B}$ and $\mathbf{u}$ must be chosen. Two such choices are implemented. The first is for Cartesian coordinates (x, y, z) with y the direction of axisymmetry and

$$\mathbf{B} = \nabla\psi \times \nabla y + I\nabla y \tag{3.36a}$$

$$\mathbf{u} = \nabla U \times \nabla y + V\nabla y + \nabla\chi. \tag{3.36b}$$

The other is curvilinear coordinates (R, φ, Z) with φ the direction of axisymmetry, and

$$\mathbf{B} = \nabla\psi \times \nabla\varphi + I\nabla\varphi \tag{3.37a}$$

$$\mathbf{u} = \nabla U \times \nabla\varphi + V\nabla\varphi + \nabla\chi. \tag{3.37b}$$

The flux/potential representations of equations (3.36) and (3.37) have several advantages over the coordinate component representation. First, the magnetic field is completely determined by the values of only two fields, ψ and I, and the condition $\nabla \cdot \mathbf{B} = 0$ is always exactly satisfied. Second, the solenoidal, toroidal, and compressible parts of the velocity are naturally separated. Third, there exist two subsets of the full system of equations which are easily recovered using this representation: one is the "two-field" equations of reduced-MHD which are recovered by evolving only ψ and U; the other is the "four-field" equations of Fitzpatrick [60] which are recovered by evolving only ψ, U, I, and V. It can be shown that each of these subsets is self-consistent and conserves energy (excluding dissipative terms).

The main disadvantage of the flux/potential representation is that it requires more spatial derivatives than would simply breaking $\mathbf{B}$ and $\mathbf{u}$ into their spatial coordinate components. Use of C^1 elements eliminates this concern, as almost no physical term has more than four spatial derivatives using the flux/potential representation, and therefore no auxiliary variables need be defined.[1]

Now each equation must be broken into scalar components, and cast in the weak form necessary for computation using finite elements. Another disadvantage of the flux/potential representation is that the these scalar equations can be quite complicated, especially when terms like the gyroviscosity are included. The end result of this process is a set of equations which can

[1]The viscous and electron-viscous heating terms do contain terms having more than four derivatives; however, these terms are generally small and may be treated explicitly without affecting numerical stability.

be written in the following block-matrix form:

$$\begin{pmatrix} S_{UU} & S_{UV} & S_{U\chi} \\ S_{VU} & S_{VV} & S_{V\chi} \\ S_{\chi U} & S_{\chi V} & S_{\chi\chi} \end{pmatrix} \begin{pmatrix} U \\ V \\ \chi \end{pmatrix}^{n+1} = \begin{pmatrix} D_{UU} & D_{UV} & D_{U\chi} \\ D_{VU} & D_{VV} & D_{V\chi} \\ D_{\chi U} & D_{\chi V} & D_{\chi\chi} \end{pmatrix} \begin{pmatrix} U \\ V \\ \chi \end{pmatrix}^{n} + \begin{pmatrix} Q_{U\psi} & Q_{UI} & Q_{Up} & Q_{Un} \\ Q_{V\psi} & Q_{VI} & Q_{Vp} & Q_{Vn} \\ Q_{\chi\psi} & Q_{\chi I} & Q_{\chi p} & Q_{\chi n} \end{pmatrix} \begin{pmatrix} \psi \\ I \\ p \\ n \end{pmatrix}^{n} + \begin{pmatrix} O_U \\ O_V \\ O_\chi \end{pmatrix} \tag{3.38}$$

$$\begin{aligned} S_{nn} n^{n+1} = D_{nn} n^n &+ \begin{pmatrix} R_{nU} & R_{nV} & R_{n\chi} \end{pmatrix} \begin{pmatrix} U \\ V \\ \chi \end{pmatrix}^{n+1} \\ &+ \begin{pmatrix} Q_{nU} & Q_{nV} & Q_{n\chi} \end{pmatrix} \begin{pmatrix} U \\ V \\ \chi \end{pmatrix}^{n} + O_n \end{aligned} \tag{3.39}$$

$$\begin{aligned} S_{pp} p^{n+1} = D_{pp} p^n &+ \begin{pmatrix} R_{pU} & R_{pV} & R_{p\chi} \end{pmatrix} \begin{pmatrix} U \\ V \\ \chi \end{pmatrix}^{n+1} \\ &+ \begin{pmatrix} Q_{pU} & Q_{pV} & Q_{p\chi} \end{pmatrix} \begin{pmatrix} U \\ V \\ \chi \end{pmatrix}^{n} + O_p \end{aligned} \tag{3.40}$$

$$\begin{pmatrix} S_{\psi\psi} & S_{\psi I} & S_{\psi p_e} \\ S_{I\psi} & S_{II} & S_{Ip_e} \\ S_{p_e\psi} & S_{p_eI} & S_{p_ep_e} \end{pmatrix} \begin{pmatrix} \psi \\ I \\ p_e \end{pmatrix}^{n+1} = \begin{pmatrix} D_{\psi\psi} & D_{\psi I} & D_{\psi p_e} \\ D_{I\psi} & D_{II} & D_{Ip_e} \\ D_{p_e\psi} & D_{p_eI} & D_{p_ep_e} \end{pmatrix} \begin{pmatrix} \psi \\ I \\ p_e \end{pmatrix}^{n} + \begin{pmatrix} R_{\psi U} & R_{\psi U} & R_{\psi U} \\ R_{IV} & R_{IV} & R_{IV} \\ R_{p_e\chi} & R_{p_e\chi} & R_{p_e\chi} \end{pmatrix} \begin{pmatrix} U \\ V \\ \chi \end{pmatrix}^{n+1} + \begin{pmatrix} Q_{\psi U} & Q_{\psi U} & Q_{\psi U} \\ Q_{IV} & Q_{IV} & Q_{IV} \\ Q_{p_e\chi} & Q_{p_e\chi} & Q_{p_e\chi} \end{pmatrix} \begin{pmatrix} U \\ V \\ \chi \end{pmatrix}^{n} + \begin{pmatrix} O_\psi \\ O_I \\ O_{p_e} \end{pmatrix}. \quad (3.41)$$

The elements of these matrices are each linear operators defined in appendix D. The two-field or four-field reduced MHD equations may be obtained simply by taking the upper-left 1×1 or 2×2 sub-matrices of the S, D, R, and Q matrices above.

These matrix equations may be solved in a number of ways. In M3D-C^1 they are typically solved using direct LU decomposition, using the distributed LU factorization software SuperLU_dist [61]. Recently M3D-C^1 has been modified to use PETSc [62, 63], which provides an abstraction layer through which a number of algorithms for the solution of matrix equations, among other things, are made available.

3.4 Benchmarks

M3D-C^1 has been used to simulate phenomena in which the solution to the dynamical equations is exactly or approximately known, either from analytic theory or through the consensus results of various other comparable, independent numerical codes. Some confidence in the veracity of the numerical methods of M3D-C^1 may be gained by comparing simulation results with these known results. There are few preexisting results against which the solutions of the full two-fluid equations may be compared, but in cases where

an equilibrium solution is known it is straightforward to derive asymptotic expressions for the linear eigenmodes in the limit where the mode wavelength is small compared to the equilibrium gradient scale length. This has been done for several types of equilibria in the presence of a gravitational force, which may be unstable to various modes of physical interest; the analytic linear theory of these modes is presented in chapter 4, and M3D-C^1 simulations are shown to be in excellent agreement with the analytic results. This is also done in detail for the normal modes of a homogeneous equilibrium in the next section.

It is more difficult to obtain analytic results for nonlinear phenomena against which simulation results can be compared. One useful diagnostic is the degree to which particle number and energy are conserved in the simulation results. While this data is calculated and output by M3D-C^1, no systematic study of energy conservation has yet been done. It is shown in section 5 that stationary steady-states obtained with M3D-C^1 do satisfy density, angular momentum, and energy balance to a high degree of accuracy (this is determined by independent post-processing and not by internal M3D-C^1 diagnostics). Benchmarks against other comparable codes may also be helpful. Such a comparison of solutions to a standard nonlinear reconnection problem [15] has been done with M3D-C^1 and the JFNK-FD [64], SEL [17], and NIMROD [20] codes; the kinetic energy in these simulations was found to agree to within a few percent over the course of the simulations [65].

3.4.1 Normal Modes of an Homogeneous Equilibrium

The normal modes of a homogeneous equilibrium were calculated by Ferraro and Jardin [21] using a non-dissipative two-fluid model including gyroviscosity in Cartesian coordinates. These results are briefly reviewed here, and new numerical results obtained with the numerical methods described in this chapter (which differ from those used in reference [21]) are presented.

In a Cartesian coordinate system (x, y, z), consider the two-fluid model

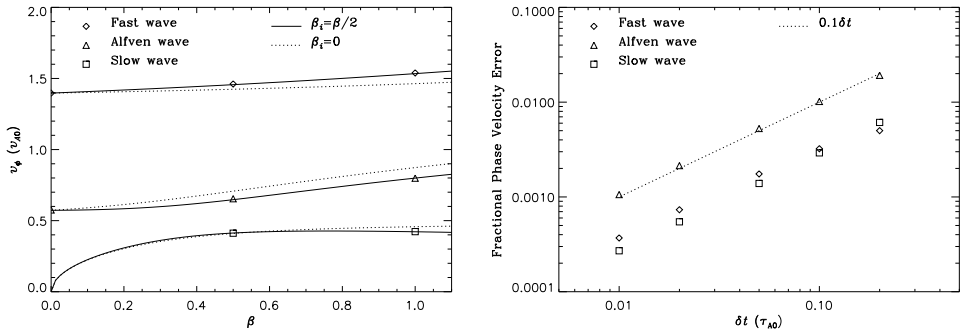

Figure 3.8: *Left*: The phase velocity of linear waves from M3D-C^1 simulations are plotted against the analytic solutions as a function of $\beta = 8\pi p_0/B^2$. *Right*: The fractional difference between the M3D-C^1 result for the phase velocity and the analytic result is plotted versus δt, with $\beta = 0.5$.

given by equations (2.8), with no external sources ($\sigma = 0$), and no thermodynamic forces except ion gyroviscosity $\mathbf{R} = \mathbf{q} = \Pi_e = Q_\Delta = 0$, $\Pi = \Pi_\wedge$, with $\Pi_\wedge$ defined by equation (2.11). Consider also the linear dispersion relation of the homogeneous, static equilibrium with $\mathbf{B} = B_{x0}\hat{\mathbf{x}} + B_{z0}\hat{\mathbf{z}}$, $p = p_0$, $p_i = p_{i0}$, and $n = n_0$. Of course, the normal modes of this system must be plane waves, with frequency ω and wavenumber $\mathbf{k}$. The dispersion relation for the normal modes with $\mathbf{k} = k\hat{\mathbf{x}}$ is

$$0 = W^2 \times \left\{ \begin{array}{l} W^6 \\ -W^4\left[1 + C^2 + (1+H^2)b_x^2 + F^2(1 + 6b_x^2 - 3bx^4)\right] \\ +W^2 b_x^2 \left[\begin{array}{l} 1 + 2C^2 - 2FH(1+b_x^2) \\ \quad + F^2\left(4[1-b_x^2] + C^2[1-3b_x^2]^2\right) \\ \quad + H^2\left(C^2 + F^2[1 + 6b_x^2 - 3b_x^4]\right) \end{array} \right] \\ -b_x^4 C^2\left[1 + FH(1-3b_x^2)\right], \end{array} \right\} \quad (3.42)$$

where the following definitions have been made

$$W = \frac{\omega}{kv_A} \tag{3.43}$$

$$C = \frac{c_s}{v_A} \tag{3.44}$$

$$H = \frac{kv_A}{\omega_{ci}} \tag{3.45}$$

$$F = \frac{k\rho_i^2\omega_{ci}}{2v_A} \tag{3.46}$$

with $c_s = \sqrt{\Gamma p_0/n_0}$, $v_A = |\mathbf{B}|^2/(4\pi n_0 m)$ (in cgs units) and $b_x = B_{x0}/|\mathbf{B}|$. Equation (3.42) has four doubly-degenerate solutions for W, representing the stationary entropy mode, and a fast (magnetosonic), Alfvén, and slow (acoustic) wave. The degeneracy corresponds to the symmetry $k \rightarrow -k$ (*i.e.* the wave may travel in either direction at the same phase velocity).

Given the scalar representation as defined in equations (3.36), the eigenmode has the form

$$\begin{aligned}
\frac{k\tilde{U}}{v_A} &= \frac{\frac{b_x}{W}\left\{W^2(X-1)+b_x^2C^2+FH[W^2(1+b_x^2)+b_x^2C^2Z]\right\}}{(1-W^2)X+C^2Y+F^2\left[W^2(1+6b_x^2-3b_x^4)-4b_x^2Y-b_x^2C^2Z^2\right]}\frac{k\tilde{\psi}}{|\mathbf{B}|} \\
\frac{\tilde{V}}{v_A} &= b_x\frac{Hb_xX\frac{k\tilde{\psi}}{|\mathbf{B}|}-FW[2Y-XZ]\frac{k\tilde{u}}{v_A}}{(1-W^2)X+C^2Y} \\
\frac{\tilde{I}}{|\mathbf{B}|} &= \frac{\frac{b_x}{W}X(\frac{\tilde{V}}{v_A}-H\frac{k\tilde{\psi}}{|\mathbf{B}|})+FYZ\frac{k\tilde{u}}{v_A}}{Y-X} \\
\frac{ik\tilde{\chi}}{Wv_A} &= \frac{b_z}{X}\left[\frac{\tilde{I}}{|\mathbf{B}|}-FZ\frac{k\tilde{U}}{v_A}\right] \\
\frac{\tilde{n}}{n_0} &= \frac{ik\tilde{\chi}}{Wv_A} \\
\frac{\tilde{p}}{p_0} &= \frac{ik\tilde{\chi}}{Wv_A} \\
\frac{\tilde{p_e}}{p_{e0}} &= \frac{ik\tilde{\chi}}{Wv_A}
\end{aligned}$$

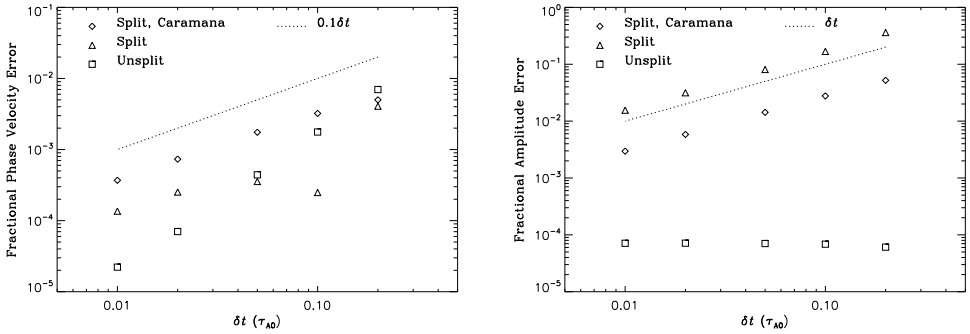

Figure 3.9: The fractional difference between the M3D-C^1 result and the analytic results for the phase velocity (left) and the amplitude of the fast wave (*i.e.* amplitude should remain constant) for various time-stepping methods.

where tildes denote the perturbed portions of each quantity, $b_z = B_{z0}/|B|$, $X = W^2 - C^2$, $Y = 1 - b_x^2$, and $Z = 1 + 3b_x^2$. The magnitude of the magnetic flux perturbation, $\tilde{\psi}$, remains arbitrary. Using these results, M3D-C^1 may be initialized in any of the propagating eigenmodes. Since the phase velocity $v_\phi = \omega/k$ of these eigenmodes is known precisely, this provides a useful benchmark for the numerical code. Such simulations have been used to benchmark earlier implementations of M3D-C^1 [21]; these benchmarks are repeated here with the methods described earlier in this chapter (see figure 3.8).

The phase velocity and amplitude errors for various time-stepping methods are plotted in figure 3.9. The methods plotted are: the "Split, Caramana" method, which is the method described in section 3.3.2; "Split", which the same as the previous method, except the dissipative term proportional to $\theta\delta t^2\mathcal{L}$ in equation (3.24) is retained; and "Unsplit", for which no time-step splitting is done, and all the fields are advanced together in a single linear θ-implicit time step. As expected, the unsplit method offers the best accuracy for this dynamical problem, both in terms of phase velocity (which converges as δt^2) and amplitude dissipation. The two "split" methods yield results roughly similar to each other, with the Caramana method being somewhat

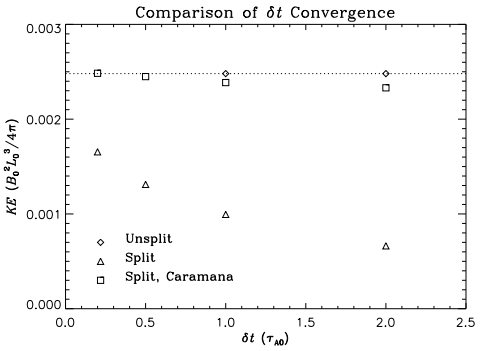

Figure 3.10: The steady-state kinetic energy of an NSTX simulation for various time-stepping methods.

less dissipative. A major advantage of the Caramana method over the non-Caramana split method is its accuracy in calculating the steady-state. This can be seen in figure 3.10, in which the steady-state kinetic energy for an NSTX simulation is shown using the various time-stepping methods. The steady-state solution obtained by the unsplit method is nearly independent of δt, and for this method the time step is limited by stability, rather than accuracy considerations when obtaining a steady-state. In contrast, the split non-Caramana split method has a very large error in steady-state which converges slowly with δt. The Caramana method is dramatically more accurate than the non-Caramana split method, is more computationally efficient than the unsplit method for an equivalent time step, and is found in many cases to be significantly more stable than the unsplit method.

3.5 Extension to Three Dimensions

Originally developed only for axisymmetric geometry, M3D-C^1 is in the process of being extended to allow linear calculations in three dimensions [66], and will eventually be extended to allow fully nonlinear calculations in three dimensions. The extension to three-dimensional linear calculations is accom-

plished by the following changes:

1. The curvilinear scalar form of the magnetic field given in equation (3.37a) is appropriate only if the magnetic field is independent of φ. Therefore a more general form is used:

$$\mathbf{B} = \nabla\psi \times \nabla\varphi + (R^2\nabla^2 f)\nabla\varphi - \nabla\left(\partial_\varphi f\right). \tag{3.48}$$

   This form derives from the expression of the vector potential $\mathbf{A} = R^2\nabla\varphi \times \nabla f + \psi\nabla\varphi$.

2. The fluid velocity is represented in curvilinear coordinates as

$$\mathbf{u} = R^2\nabla U \times \nabla\varphi + \omega R^2\nabla\varphi + \frac{1}{R^2}\nabla_\perp\chi \tag{3.49}$$

   where $\nabla_\perp = \nabla - \hat{\varphi}\hat{\varphi}\cdot\nabla$. This form has properties advantageous for calculating linear eigenmodes. In particular, in this form only χ is coupled to the toroidal field when $B_\varphi \propto R^{-1}$. In tokamak geometry, even slight compression of the toroidal field is highly stabilizing. By separating compressive flows from non-compressive flows, this form helps avoid artificial stabilization of modes from truncation error in the finite element representation of the flow leading to toroidal field compression.

3. The equations are linearized, and Fourier transformed in the φ direction. The Fourier transform is done by simply letting scalar to be complex and letting $\partial_\varphi \to in$. Only a single Fourier mode n is retained.

The three-dimensional linear stability capability is in the process of being benchmarked with simulations of external kink modes. These benchmarks have shown promising preliminary results. However, since none of the results in the rest of this dissertation involve three-dimensional stability calculations, these preliminary results will not be discussed in detail here.

Chapter 4

Weak Instabilities

Rosenbluth, Krall, and Rostoker (RKR) [13] showed using kinetic theory that FLR effects can be stabilizing to "weakly unstable" modes—defined as modes having a linear growth rate much smaller than the ion cyclotron frequency—even when the normal mode wavelength is much larger than the ion Larmor radius. It was later shown by Roberts and Taylor (RT) [67] that this result could be obtained from fluid theory by retaining the gyroviscous stress component of the ion pressure tensor; that is, the finite Larmor radius correction to the MHD equations are contained in the gyroviscous stress.

The following sections contain linear fluid theory analysis of three instabilities: the gravitational instability, which is the instability originally considered by RKR and RT; the magnetorotational instability (MRI), which may occur in astrophysical accretion disks; and the magnetothermal instability (MTI), which affects thermally stratified magnetized plasmas. Each of these analyses is carried out using fluid theory, while retaining two-fluid effects through the Hall term, and FLR effects though the gyroviscous stress. The purpose of these analyses is to demonstrate the significant impact that these effects can have on the stability of equilibria, even in the case of strong magnetization. Indeed, the results of the MRI analysis contradicts the common belief that FLR effects are negligible in all accretion systems of physical

interest.

The sections discussing the gravitational instability and the MRI essentially repeat analyses previously published by Ferraro and Jardin [21] and Ferraro [23], respectively. The analysis of the MTI has not previously been published.

4.1 Gravitational Instability

Fluids having a density gradient opposite to the gravitational field are generally unstable. In neutral fluids, this is the well known Rayleigh-Taylor instability. If the fluid is magnetized, the behavior of the fluid may differ significantly from that of a neutral fluid. Rosenbluth, Krall and Rostoker [13] were the first to calculate, by kinetic analysis, the stabilizing effect on this instability of FLR effects. Roberts and Taylor [67] recovered RKR's result in the fluid formalism by including the gyroviscous stress.

RT's simple fluid analysis showed that both gyroviscosity and the two-fluid effects represented by the Hall term may independently stabilize the gravitational instability. The gyroviscous stabilization is due to the fact that gyroviscosity transports the z-directed momentum across the x-direction—that is, finite Larmor orbits transfer some vertical momentum from upward-flowing regions into downward-flowing regions, and vice-versa [13, 68]. The stabilization due to the Hall term results from the electrons sweeping the magnetic field perturbations out of phase with the fluid velocity perturbations.

Both RKR and RT assumed that $k_z = 0$ (where $\hat{\mathbf{Z}}$ is the direction of the density gradient), and considered only the very low-β limit, where $\beta = 8\pi p/B^2$, in order to justify the electrostatic assumption. Below is presented a linear analysis of the gravitational instability which extends the RT result to arbitrary β and $k_z \neq 0$.

4.1.1 Local Linear Analysis

Model

The effects of gyroviscosity and Hall currents in the gravitational instability may be understood using a simple two fluid model:

$$\frac{\partial n}{\partial t} + \nabla \cdot (n\mathbf{u}) = 0 \tag{4.1a}$$

$$mn\left(\frac{\partial \mathbf{u}}{\partial t} + \mathbf{u} \cdot \nabla \mathbf{u}\right) = \frac{\mathbf{J} \times \mathbf{B}}{c} - \nabla p - \nabla \cdot \Pi - mng\hat{\mathbf{z}} \tag{4.1b}$$

$$\frac{\partial \mathbf{B}}{\partial t} = -c\nabla \times \mathbf{E}. \tag{4.1c}$$

The current density is defined by equation (2.8g), as usual. The isothermal limit ($\Gamma = 1$) will be considered here, so that the pressure is determined by the equation of state $p = nT$, with T constant. In order to exclude two-fluid effects arising from ∇p_e for simplicity, it is assumed that $p = p_i$. Only the low-collisionality limit in which resistivity and perpendicular viscosity may be neglected is considered here. Ohm's law in this case is

$$\mathbf{E} + \frac{\mathbf{u} \times \mathbf{B}}{c} = \frac{1}{ne}\frac{\mathbf{J} \times \mathbf{B}}{c}. \tag{4.2}$$

Formally the ion pressure tensor will be taken to be of the Braginskii form $\Pi = \Pi_{\parallel} + \Pi_{\wedge}$ as defined in equations (3.4), though $\Pi_{\parallel}$ does not affect the linear dispersion relation for the gravitational mode in the equilibrium geometry described below. The subsequent analysis will be carried out in a Cartesian coordinate system (x, y, z) with axisymmetry assumed in the y direction.

Equilibrium

Schnack [69] pointed out that it is necessary for the equilibrium to be supported by a magnetic field gradient, and not a thermal pressure gradient, in order to ensure that $\partial p/\partial n$ is positive definite. Therefore the following

equilibrium is used:

$$\begin{aligned} n(z) &= n_0 e^{z/L_n} && (4.3a)\\ p(z) &= Tn(z) && (4.3b)\\ B_y(z) &= \sqrt{B_{y0}^2 - 2(gL_n + T)[n(z) - n_0]}. && (4.3c) \end{aligned}$$

Dispersion Relation

In the local limit, $(kL_n)^{-1} \sim \delta \ll 1$, the eigenfunctions are plane waves of the form $\exp[i(k_x x + k_z z - \omega t)]$ to lowest order in δ. The gravitational mode can be isolated by choosing the frequency to be on the order of the ideal growth rate, $\omega \sim \sqrt{g/L_n} \sim \delta$. Furthermore, the viscous closure considered here is only valid in the magnetized limit, and so only the ordering $k\rho_i \lesssim \delta$ is considered here. Given these orderings, to lowest order in δ the dispersion relation is found to be:

$$\begin{aligned} 0 \;=\; & (1+C)\,W^2 \\ & -[2F(1+G+C)(1+C)+2FG+H]\,W \\ & +(1+G+C) \end{aligned} \qquad (4.4)$$

where

$$\begin{aligned} W &= \frac{k\omega}{k_x\sqrt{g/L_n}} && (4.5a)\\ H &= \frac{k\sqrt{gL_n}}{\omega_{ci}} && (4.5b)\\ F &= \frac{\rho_i^2\omega_{ci}k}{2\sqrt{gL_n}} && (4.5c)\\ C &= c_s^2/v_A^2 && (4.5d)\\ G &= gL_n/v_A^2 && (4.5e) \end{aligned}$$

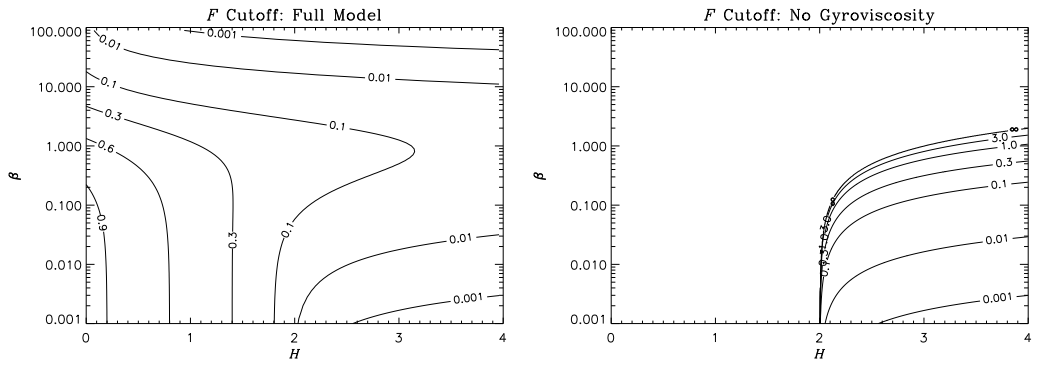

Figure 4.1: Contour plots of the value of F at which the gravitational mode is stabilized, versus the two other independent parameters in the dispersion relation, equation (4.4). *Left*: the result of the full model; *right*: the result with gyroviscosity omitted.

and where $k = |\mathbf{k}|$, $c_s^2 = T/m_i$, and $v_A^2 = B_{y0}^2/4\pi n_0 m_i$. Note that the definition of H here is the inverse of that in ref. [21]. RT's dispersion relation,

$$0 = W^2 + (2F + H)W + 1, \tag{4.6}$$

is recovered from equation (4.4) in the limit where $\beta \ll 1$ and $G \ll 1$. (RT's original definition of F is half of that defined by equation (4.5c). This discrepancy has previously been attributed to the fact that equation (4.4) was derived under the assumption that $p = p_i$ [21]. However, repeating this derivation without invoking that assumption does not resolve the discrepancy. In fact, it appears that RT's expression for the gyroviscous force includes an erroneous factor of 1/2, as their expression for this force differs both from that of Thompson [70], which RT cite as the source for their expression, and Braginskii [27]. For proper comparison with the results here, equation (4.5c) is used to define F in their dispersion relation. Also, strictly, RT's result is equation (4.6) evaluated at $k = k_x$.)

Aside from the normalized frequency W, equation (4.4) contains only three independent dimensionless parameters, chosen in the following analysis

to be F, H, and C. In both equations (4.4) and (4.6), the terms containing F are due to gyroviscosity, and those containing H are due to the Hall effect. Note that G is not independent of F, H, and C, since $G = CH/2F$. The value of F at which the gravitational mode is stabilized may be calculated as a function only of H and $\beta = 2C$ by eliminating G in favor of F, H, and β. (This is not done in equation (4.4) so as not to imply that terms otherwise containing G are due to the Hall effect or the gyroviscous force.) Contours of these cutoff values are shown in figure 4.1, both for the full dispersion relation (equation (4.4)), and for the case where gyroviscosity is omitted ($F \to 0$ in equation (4.4)). From that figure, it can be seen that the Hall term is responsible for stabilizing modes having both $\beta \ll 1$ and $H \gtrsim 2$, but does not stabilize modes outside this region of parameter space. FLR effects independently stabilize all modes at $F = 1$, and are especially stabilizing at high β. Note that the gravitational mode can be stabilized by gyroviscosity even when $FH = k^2\rho_i^2/2 \ll 1$. This is possible because of the relatively slow growth rate of the gravitational instability [13].

It is important to realize that it is not the case that, in these diagrams, neglecting the the gyroviscous stress is equivalent to letting $F = 0$, nor is it the case that neglecting the Hall effect is equivalent to letting $H = 0$. In equation (4.4), terms due entirely to gyroviscosity or the Hall effect are explicitly proportional to F or H, respectively, only because other occurrences of these factors have been suppressed by the introduction of the dependent variable G there.

4.1.2 Numerical Simulation

Linear Simulation results

Linear simulations of the gravitational instability have been run using M3D-C^1. The simulation domain has dimensions $L_x \times L_z$, with periodic boundaries at $x = \pm L_x/2$ and conducting, no-normal-flow boundaries at $z = \pm L_z/2$.

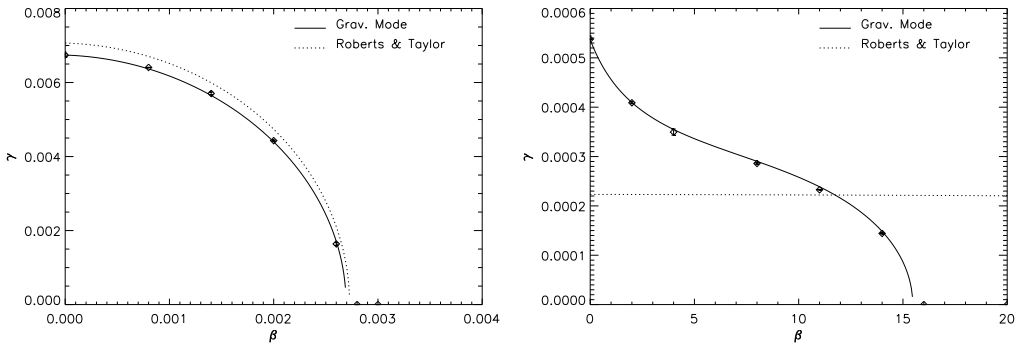

Figure 4.2: The linear growth rate of the gravitational instability as a function of β, as calculated from equation (4.4) (solid line), from RT's dispersion relation (dotted line), and as calculated from numerical simulations using M3D-C^1(diamonds).

The dimensions are chosen to exclude wavenumbers smaller than $k_x = 2\pi/L_x$ (smaller wavenumbers are more unstable). Dissipative terms can strongly affect the growth rate, but in these linear cases M3D-C^1 is able to run stably with $\eta = \mu = 0$. The density gradient scale length is taken to be large ($L_n \gg L_z$) to keep the equilibrium fields approximately constant over the entire box.

The initial conditions are seeded with a small ($\sim 10^{-6} n_0$) perturbation to the density density equilibrium with $k_x = 2\pi/L_x$ and $k_z = \pi/L_z$. The simulation is allowed to proceed until the growth rate of the density and stream function perturbations equalize and become independent of time. The growth rate is measured by

$$\gamma = \frac{1}{2}\frac{\partial}{\partial t} \ln \left[\int_0^{L_x} dx\, A^2(x, z = 0, t) \right] \tag{4.7}$$

where A is the density or the stream function. The data points in the figures actually represent the average of the density and stream function growth rates, and the discrepancy between the two values is illustrated by the error

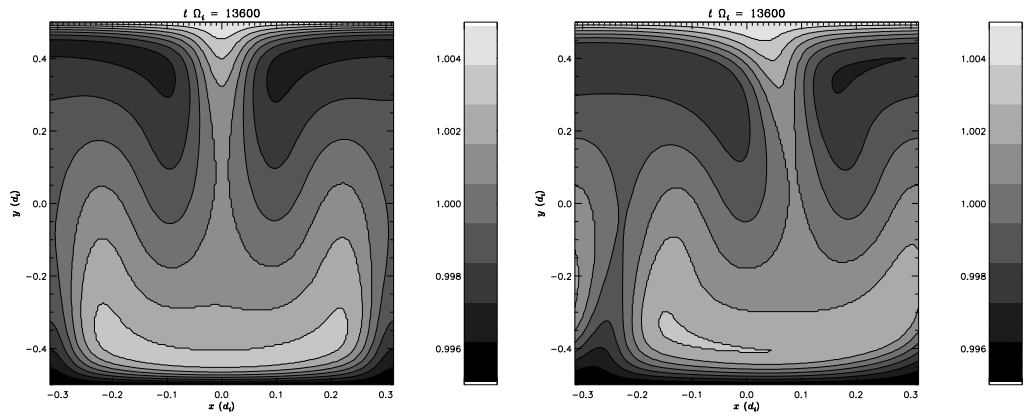

Figure 4.3: The density profile in the nonlinear phase of the gravitational instability. *Left*:Gyroviscosity is omitted; *right*: gyroviscosity is included.

bars (this discrepancy is generally smaller than the data point symbol itself).

Two distinct cases are presented here: a low-β case to which RT's result is applicable, and a high-β case in which the effects of compressibility and electromagnetism are important. Specifically, for the low-β case, $L_x = 2\pi/10$, $L_z = 1$, $L_n = 100$, $g = 0.005$, and $B_{y0} = 100$. For the high-β case, $L_x = 2\pi/0.05$, $L_z = \pi/0.01$, $L_n = 10^5$, $g = 0.0005$, and $B_{y0} = 1$. Here length scales are normalized to d_i and time scales to ω_{ci}. As expected, RT's result is fairly accurate only for the low-β case (the discrepancy is due to the fact that $k_z = 0$ in Roberts and Taylor's analysis). In both cases the simulation results are quite close to the exact solution to equation (4.4).

Nonlinear Simulation Results

Some simulations of the gravitational instability have been run far into the nonlinear regime. The parameters for these simulations are $B_{y0} = 20$, $L_n = 100$, $g = 0.05$, $p_0 = 0.5$, $\eta = 10^{-3}$, $\mu = 10^{-5}$, $\kappa = 10^{-5}$, and $\delta t = 800$. The simulations are started with a density perturbation ($\epsilon = 10^{-3}$), and allowed to proceed until the density gradient is essentially quenched.

Images of the density profile at a time far into the nonlinear evolution

of the instability are shown in figure 4.3. In the figure, the inclusion of gyroviscosity can be seen to cause the density perturbation to advect in the x-direction. This is due to the gyroviscous cancellation effect (see section 2.2.2). The shear in this advection velocity is due to the fact that the magnetization velocity v_* is not constant over the simulation domain.

4.2 Magnetorotational Instability

In astrophysical accretion disks, gravitationally bound matter orbits, and may eventually fall into, a central massive object. In order for orbiting matter to move inward toward the central object, it must lose angular momentum. The rate of this inward transport of matter (and hence outward transport of angular momentum) is observed to be much larger than can be accounted for by classical viscosity, assuming the flow of the rotating matter is laminar. It is presumed that some process causes this rotation to be turbulent, and that this turbulence is responsible for the increased viscosity leading to large rates of angular momentum transport.

A leading candidate for the catalyst of this turbulence is the magnetorotational instability (MRI) [71]. This instability may be present in ionized, rotating disks having sheared azimuthal flow (such as is the case for a Keplerian rotation profile) and a weak magnetic field. In most physical scenarios the MRI is weakly unstable in the sense of Rosenbluth *et al.*, and therefore may be expected to be affected by FLR effects, even though typical wavelengths of this instability in astrophysical scenarios may be vastly larger than the ion Larmor radius. In this section the the effect of non-ideal processes on the MRI in the linear regime is explored, and it is shown that indeed the MRI may be stabilized by gyroviscous effects at scales much larger than the ion Larmor radius. In some cases this stabilization substantially constrains the spectrum of linearly unstable modes.

The effect of the Hall term, which accounts for differences between the

electron and ion fluid velocities, has been examined previously by several authors [72, 73, 74, 75]. In particular, it was found that the Hall effect may be either stabilizing or destabilizing, depending on whether the equilibrium magnetic field is aligned or anti-aligned to the equilibrium angular velocity. It was also found that the Hall effect is important only when the ion cyclotron frequency is comparable to, or smaller than, the orbital frequency. This situation may occur in early galaxy formation where the magnetic fields are still weak, or in weakly ionized protostellar disks. Krolik and Zweibel [75] have suggested that, in this limit, short-wavelength modes are likely suppressed by viscous or resistive damping, leaving only slowly growing, long-wavelength modes as the magnetic field get sufficiently weak. However, their analysis is restricted to low-β_i plasmas as they do not consider FLR effects, which are shown to be much more important than the Hall effect in the weak-field limit. The strong FLR stabilization of the MRI in the weak-field limit may have important implications for the possible role of the MRI in the amplification of weak, primordial magnetic fields.

The MRI in the collisionless regime, where the collisional mean free path is greater than the mode wavelength, has been explored by Quataert, Dorland, and Hammett [42], and Sharma, Hammett, and Quataert [43] using kinetic closures. Islam and Balbus [44, 76] have extended the single-fluid MHD treatment to lower collisionality regimes by including the Braginskii form of the parallel viscosity, and have obtained results similar to those obtained using kinetic closure. These various analyses have found the linear growth rate to be enhanced by a factor of order unity at lower collisionality when an azimuthal component of the magnetic field is present, but the criterion for instability was found not to differ from the MHD result. The parallel viscous stress is included for completeness in the following analysis, as formally it may be larger than the gyroviscous stress. However, for the sake of simplicity the MRI mode wavevector and magnetic field are restricted to be normal to the accretion disk, in which case the parallel viscosity has no effect on the

linear growth of the MRI. This case is the most unstable one in the collisional limit, which is the limit considered here.

4.2.1 Local Linear Analysis

Model

The effect of parallel viscosity, gyroviscosity, and the Hall term may be determined by examining a simplification of equations (2.8). Specifically, the following model is used:

$$\frac{\partial n}{\partial t} + \nabla \cdot (n\mathbf{u}) = 0 \tag{4.8a}$$

$$nm\left(\frac{\partial \mathbf{u}}{\partial t} + \mathbf{u}\cdot\nabla\mathbf{u}\right) = \frac{\mathbf{J}\times\mathbf{B}}{c} - \nabla p - \nabla\cdot\mathsf{\Pi} - ng(R)\hat{\mathbf{R}} \tag{4.8b}$$

$$\frac{\partial \mathbf{B}}{\partial t} = -c\nabla\times\mathbf{E}. \tag{4.8c}$$

$$dp_\alpha = \Gamma T_\alpha dn \tag{4.8d}$$

$$\mathbf{E} + \frac{\mathbf{u}\times\mathbf{B}}{c} = \frac{1}{ne}\left(\frac{\mathbf{J}\times\mathbf{B}}{c} - \nabla p_e\right) \tag{4.8e}$$

where collisional forces ($\mathbf{R}$) have been neglected, and the pressure is assumed to obey a simple equation of state ($\Gamma = 5/3$ represents the adiabatic equation of state; $\Gamma = 1$ represents the isothermal equation of state). The electron pressure tensor has also been neglected, which is valid to lowest order in m_e/m_i. The ion pressure tensor is assumed to take the Braginskii form, with $\mathsf{\Pi} = \mathsf{\Pi}_\parallel + \mathsf{\Pi}_\wedge$ as defined in equations (2.23) and (2.11). Again, $\mathsf{\Pi}_\wedge$ is the gyroviscous force, which represents the lowest-order FLR correction to the fluid equations. The perpendicular viscosity is smaller than the gyroviscosity by a factor of ω_{ci}/ν_i, and may therefore be neglected in the low-collisionality limit where $\nu_i \ll \omega_{ci}$. Together with the short mean-free-path condition ($k_\parallel v_{ti} \ll \nu_i$) necessary to justify the use of the Braginskii form of $\mathsf{\Pi}$, this restricts the validity of these results to the parameter regime where $k_\parallel v_{ti} \ll$

$\nu_i \ll \omega_{ci}$. In the case of an accretion disk where $k_\parallel \gtrsim 1/d$ is limited by the disk height $d \sim v_{ti}/\Omega$, where Ω is the angular frequency of the disk, this validity condition becomes $\Omega \ll \nu_i \ll \omega_{ci}$.

Equilibrium

Curvilinear coordinates (R, φ, Z) are used, with the assumption of axisymmetry in φ. For simplicity, it is assumed that the equilibrium magnetic field is perpendicular to the disk, $\mathbf{B}_0 = B_0\hat{\mathbf{Z}}$, and that the equilibrium fluid velocity is purely toroidal, $\mathbf{u}_0 = R\Omega(R)\hat{\varphi}$. Without loss of generality, the coordinate system is oriented so that $\Omega(R) > 0$ at the radius of interest. In this case, radial force balance is satisfied when

$$g(R) = R\Omega^2(R) + \frac{\rho_i^2\omega_{ci}}{2R^2}\frac{\partial}{\partial R}\left[R^3\Omega'(R)\right]. \tag{4.9}$$

Equilibrium structure in the Z-direction is neglected. In the following derivation, equation (4.9) is used to eliminate $g(R)$ in favor of $\Omega(R)$ (hereafter the explicit dependence of Ω on R will be dropped).

Dispersion Relation

Consider linear perturbations about this equilibrium having scale lengths $1/k$ much smaller than the equilibrium flow gradient scale length $L = \Omega/\Omega'$, so that $\delta = 1/|kL| \ll 1$. In this limit, the normal modes of the system are plane waves to lowest order in δ. This analysis is restricted to perturbations $\propto e^{i(kz-\omega t)}$ (*i.e.* $\mathbf{k} = k\hat{\mathbf{Z}}$) for simplicity, as this is the most unstable case in both the MHD and collisionless limits [42]. Carrying out the linearization of equations (4.8) yields the following dispersion relation, to lowest order in δ:

$$\begin{aligned} 0 \;=\; & (W^2 + W\frac{8i\eta_{0i}}{3}\frac{\omega_{ci}}{\nu_i}A - C) \times \\ & \times \left\{W^4 - W^2\left[2(2+R+K) - 2A(4+R-2A) + H(R+H)\right] + \right. \\ & \left. + \left[K - A(R+2H) + 2(R+H)\right]\left[K - A(R+2H) + H(2+R)\right]\right\} \end{aligned} \tag{4.10}$$

where the following dimensionless quantities are defined:

$$W = \omega/\Omega \tag{4.11a}$$
$$K = (v_A k/\Omega)^2 \tag{4.11b}$$
$$A = \frac{1}{2}k^2\rho_i^2(\omega_{ci}/\Omega) \tag{4.11c}$$
$$H = K(\Omega/\omega_{ci}) \tag{4.11d}$$
$$C = (c_s k/\Omega)^2 \tag{4.11e}$$
$$R = r\Omega'/\Omega. \tag{4.11f}$$

and characteristic velocities $v_A^2 = B_0^2/4\pi n_0 m_i$ and $c_s^2 = \Gamma T/m_i$. The dimensionless parameter A measures the importance of the gyroviscous force, and setting $A = 0$ is equivalent to omitting $\Pi_\wedge$ in the ion momentum equation. Similarly, H measures the importance of the Hall term in Ohm's law, and K measures the importance of magnetic tension. R is the ratio of the radial coordinate to the equilibrium flow gradient scale length, and is taken to be $\sim \mathcal{O}(1)$. For a Keplerian disk, $R = -3/2$. In order to quantify the importance of the gyroviscous force with a dimensionless variable independent of the wavenumber, the quantity

$$F = \frac{A}{K} = \frac{\beta_i}{4}\frac{\Omega}{\omega_{ci}},$$

is defined, where $\beta_i = 8\pi p_{i0}/B_0^2$ is the ratio of ion thermal pressure to magnetic pressure.

Equation (4.10) contains two uncoupled modes. The first factor contains the compressive acoustic mode, which is damped by the parallel viscosity, and is not of interest here. The second factor, enclosed in braces, contains the incompressible MRI mode. In the limit where $A \to 0$ (no FLR effects), and $H \to 0$ (no Hall effect), the ideal dispersion relation is recovered [77]. Note that the parallel viscosity ($\propto \eta_{0i}$) affects only the acoustic mode and not the MRI. Evidently, there is no $\mathcal{O}(\Omega/\nu_i)$ correction to the MHD result

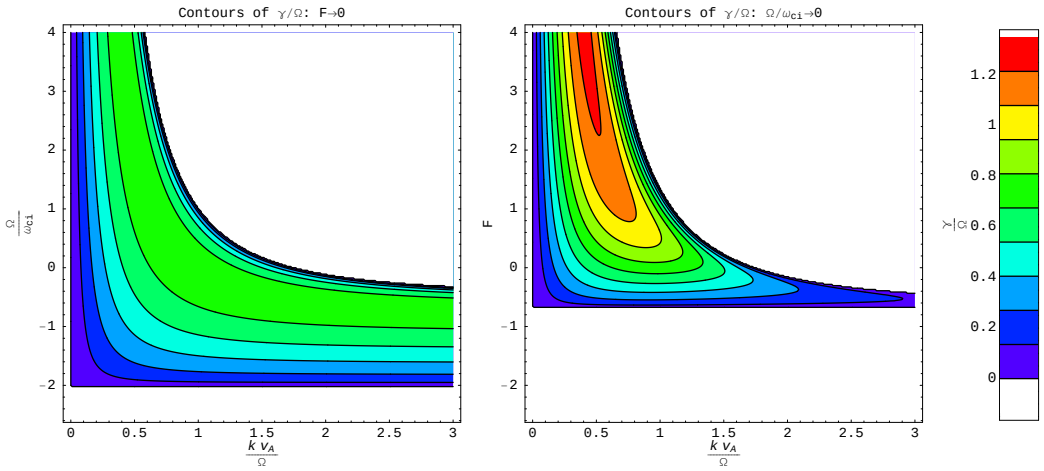

Figure 4.4: The linear growth rate of the MRI in the limits $F \to 0$ (left) and $H \to 0$ (right).

for the MRI when $\mathbf{B}_0 = B_0\hat{\mathbf{Z}}$, which is in agreement with previous findings [43, 44]. In the collisional case, the $\mathbf{B}_0 = B_0\hat{\mathbf{Z}}$ case is the most unstable and is therefore the one of interest here. Extending this analysis to a more general magnetic field configuration substantially complicates the analysis.

It should also be noted that ω_{ci} is a signed quantity since it is proportional to B_0, which may be positive or negative. Since the coordinate system has been chosen so that Ω is positive, sign ω_{ci} = sign $\mathbf{B} \cdot \mathbf{\Omega}$ = sign F. It has been shown previously that the effect of the Hall term on the MRI depends strongly on the sign of ω_{ci} [72]. The effect of the gyroviscous force has a similarly strong dependence.

The growth rate $\gamma = \text{Im}\,\omega$ of the unstable solution to equation (4.10) is plotted in figure 4.4 for a Keplerian rotation profile ($R = -3/2$). Note that the abscissa should be read as a normalized wavenumber and not a normalized magnetic field strength, because F and Ω/ω_{ci} are dependent on B. When $\omega_{ci} > 0$, and hence $F > 0$ also, both the FLR and the Hall effects can be seen to move the most unstable mode to lower wavenumbers, and to reduce the value of K at which the MRI is completely stabilized. Also,

FLR effects increase the growth rate of the most unstable mode. When $\omega_{ci} < 0$, and hence $F < 0$, both effects are seen instead to increase the cutoff value of K all the way to the point where modes of any wavelength are unstable. When F or Ω/ω_{ci} becomes sufficiently negative ($F < -2/3$ when $\Omega/\omega_{ci} \to 0$, or $\Omega/\omega_{ci} < -2$ when $F \to 0$), all values of k are suddenly completely stabilized. (It has been shown that this stabilization is less sudden when finite resistivity is included [73].)

Instability Criterion

Applying the Routh-Hurwitz theorem to equation (4.10), it is found that the condition for stability of an MRI mode is that the following inequalities are satisfied:

$$\begin{aligned} 0 &< 2(2+R+K) - 2A(4+R-2A) + H(R+H) \\ 0 &< [K - A(R+2H) + 2(R+H)]\,[K - A(R+2H) + H(2+R)] \end{aligned}$$

This criterion is highly complicated, and for general values of A and H, there may be multiple stable and unstable regions of in K-space.

In the ideal limit, when $A \to 0$ and $H \to 0$, the ideal instability criterion, $K < -2R$, is recovered [77]. This limit is well understood, and in this case stabilization at high-K is due to the effect of magnetic tension. In this limit, instability does not exist in flows in which the angular velocity increases with radius ($R > 0$).

The limit $A \to 0$, in which case the Hall effect is dominant over the FLR effects, has also been considered before [72]. Since $A/H = F/(\Omega/\omega_{ci}) = \beta_i/4$, this limit describes accretion disks having $\beta_i \ll 1$. Formally, the instability criterion in this case remains somewhat complicated because the signs and relative magnitudes of most of the terms are undetermined in general. The

criterion for instability

$$K\left[\left(1+2\frac{\Omega}{\omega_{ci}}\right)\left(1+\frac{\Omega}{\omega_{ci}}(2+R)\right)\right] < -2R\left[1+\frac{\Omega}{\omega_{ci}}(2+R)\right] \tag{4.13}$$

has been derived from an analysis of the physical forces involved by Balbus and Terquem [73]. There is some discussion of this criterion in the articles by [72] and [73], as well as insight into its physical meaning. This discussion will not be repeated here, except to mention a few interesting points. The first is that there may exist some values of Ω/ω_{ci} for which modes of any wavelength are unstable (this is true in the Keplerian case for $-2 < \Omega/\omega_{ci} < -1/2$). Also, some unstable modes may be present in disks in which angular velocity increases with radius ($R > 0$), in contrast to the ideal result [73].

Of more physical interest in the opposite limit, $\beta_i \gg 1$, in which FLR effects are dominant over the Hall effect. Taking $H \to 0$, the dispersion relation for the MRI reduces to

$$0 = W^4 - 2\left[2+R+K-A(4+R-2A)\right]W^2 + \left[K-AR+2R\right]\left[K-AR\right] \tag{4.14}$$

and the criterion for instability is found to be

$$K < -\frac{2R}{1-FR}. \tag{4.15}$$

For the usual case where $R < 0$, all modes are completely stabilized if $F < -1/|R|$. For the case where $R > 0$, unstable modes may exist when $F > 1/R$. In the limit where the gyroviscous force dominates the force of magnetic tension, $F \gg 1$, the instability criterion becomes simply

$$A < 2 \tag{4.16}$$

or, equivalently, $(k\rho_i)^2 < 4\Omega/\omega_{ci}$. Note that this condition closely agrees with RKR's hypothesis that instabilities are stabilized by FLR effects when

$(k\rho_i)^2 \gtrsim \gamma_H/\omega_{ci}$, where γ_H is the ideal growth rate of the instability.

An important point is that the FLR effects are dominant in the weak-field limit. Of course, FLR effects are dominant over magnetic tension in this limit, which can be seen by noting that $A/K = F \propto B^{-3}$. FLR effects also are dominant over the Hall effect, since $A/H = \beta_i/4 \propto B^{-2}$; therefore previous analyses of the MRI in the weak-field limit (in the sense that $\Omega/\omega_{ci} \gtrsim 1$) which did not consider FLR effects are valid only for $\beta_i \ll 1$. Looking at equation (4.16), which is the proper instability criterion for the weak-field limit, one can see that the MRI is cut off at sufficiently weak fields, because $A \propto B^{-1}$. This is the proper resolution to the inconsistency of the ideal MHD result that the MRI remains unstable as $B \to 0$ in the non-dissipative case. Because the MRI is not present at arbitrarily low magnetic fields, its role in the amplification of primordial magnetic fields is severely restricted.

In the FLR-dominated case, MRI modes are stabilized when $(k\rho_i)^2 > 4(\Omega/\omega_{ci})$, where Ω/ω_{ci} is typically small in astrophysical accretion disks. The importance of this stabilization may increased by the fact that, in an accretion disk, the lower bound on k is set by the width of the disk d, which may be much smaller than the equilibrium flow gradient scale length L. Although a proper understanding of this phenomenon must take into account the z-stratification of the disk equilibrium, one may estimate that the smallest wavenumber present in the disk to be $\sim \pi/d$. The criterion for complete stabilization by FLR effects of *all* MRI modes within an accretion disk at some distance from the central mass is

$$\pi^2(\rho_i/d)^2 \gtrsim 4\Omega/\omega_{ci}. \tag{4.17}$$

In the typical case where $d \sim v_t/\Omega$ this inequality reduces to $\omega_{ci}/\Omega \lesssim \pi^2/4$. While this is not typically satisfied in astrophysical accretion disks, it may be satisfied in nascent galaxies with weak magnetic fields, or weakly ionized protostellar disks [75].

4.3 Magnetothermal Instability

Balbus [78] showed that a thermally stratified, magnetized plasma in a gravitational field, such that $\mathbf{g} \cdot \nabla T > 0$, and such that the magnetic field is transverse to the temperature gradient, may be unstable. This magnetothermal instability (MTI) depends on the presence of a weak magnetic field perpendicular to the thermal gradient, and anisotropic thermal conduction that is much greater along the magnetic field than perpendicular to it, as is typical for a magnetized plasma [27]. The MTI is significant because it may be present even when the Schwarzschild condition for convective stability, $\mathbf{g} \cdot \nabla S < 0$, where S is the entropy density of the plasma, is satisfied.

4.3.1 Local Linear Analysis

Equilibrium

Consider an equilibrium having a constant horizontal field and a pressure and density varying in the vertical direction in a Cartesian coordinate system (x, y, z):

$$\begin{aligned} \mathbf{B} &= B\hat{\mathbf{x}} \\ n &= n(z) \\ p &= p(z) \end{aligned}$$

where $p' = -ng$ to satisfy hydrostatic equilibrium.

The Brunt-Väisälä frequency of the equilibrium, N, is defined by

$$N^2 = -\frac{1}{\Gamma}\frac{\partial p}{\partial z}\frac{\partial \ln S}{\partial z},$$

where the entropy density is $S = pn^{-\Gamma}$. For a neutral fluid, the condition for stability is that N is real and positive (*i.e.* entropy increases with height); however, a magnetized plasma in such an equilibrium will have a different

stability criterion due to the MTI.

Model

This analysis is carried out in the low-collisionality regime where η, and perpendicular viscosity may be neglected, though within the short mean-free-path limit. The only component of the pressure tensor which affects the linear stability of this equilibrium is the gyroviscosity. For simplicity, the assumption that p_e is a constant fraction of p everywhere is made. Therefore the following model is used consists of equations (2.8a)–(2.8c), (2.8f), (2.8g), and (2.8e), with

$$\mathbf{F} = -g\hat{\mathbf{z}} \tag{4.19a}$$

$$\mathbf{q} = -\kappa_\circ \nabla T - \kappa_\parallel \mathbf{b}\mathbf{b} \cdot \nabla T \tag{4.19b}$$

$$\mathbf{R} = 0 \tag{4.19c}$$

$$\Pi_e = 0. \tag{4.19d}$$

The ion pressure tensor is assumed to take the Braginskii form, with

$$\Pi = \Pi_\parallel + \Pi_\wedge \tag{4.20}$$

as defined in equations (3.4).

Linear Dispersion Relation

Consider modes having wavelengths much shorter than equilibrium gradient scale lengths, $kL \sim \delta \ll 1$, where $L = p/p'$; and with plane-wave eigenfunctions of the form $\exp(\gamma t + ikx)$. The dispersion relation is found to be, to lowest order in δ,

$$0 = W^3 + XW^2 + (1+Z)W - X(Y-Z) \tag{4.21}$$

where the following dimensionless quantities have been defined:

$$W = \gamma/N \tag{4.22a}$$

$$X = \frac{\Gamma - 1}{\Gamma}\frac{k^2(\kappa_\parallel + \kappa_\circ)}{Nn} \tag{4.22b}$$

$$Y = -\Gamma\frac{\partial \ln T}{\partial \ln S}\frac{\kappa_\parallel}{\kappa_\parallel + \kappa_\circ} \tag{4.22c}$$

$$Z = k^2 v_A^2/N^2 + (k\rho_i)^4(\omega_{ci}/N)^2. \tag{4.22d}$$

The condition for hydrostatic equilibrium, $p' = -ng$, is has been used to eliminate g. In contrast to the derivation of this dispersion relation differs from that of Balbus [78], it is necessary to retain the component of the momentum equation in the direction of axisymmetry (y) because of the coupling between the various flow components introduced by the gyroviscous force. Letting $\rho_i \to 0$, equation (4.21) reduces to the dispersion relation given by Balbus [78].

It can readily be seen from equation (4.21) that there are no growing solutions (Re $W > 0$) when

$$Z \geq Y, \tag{4.23}$$

and therefore such modes are stable. The first term of Z in equation (4.22d) represents the effect of magnetic tension, and the second term represents the FLR (*i.e.* gyroviscous) effect. Both terms are positive definite, and are therefore always stabilizing. Comparing the two terms reveals that the FLR effects dominate the magnetic tension force when $(k\rho_i)^2 \gtrsim 1/\beta$. In the limit where the magnetic tension force dominates the stability criterion given by Balbus [78] is recovered. In the opposite limit, in which the FLR effects are dominant, the condition for stability reduces to

$$k\rho_i \gtrsim 1/(kL). \tag{4.24}$$

Thus, for normal modes where $kL \gg 1$ (*i.e.* for modes where equation (4.21)

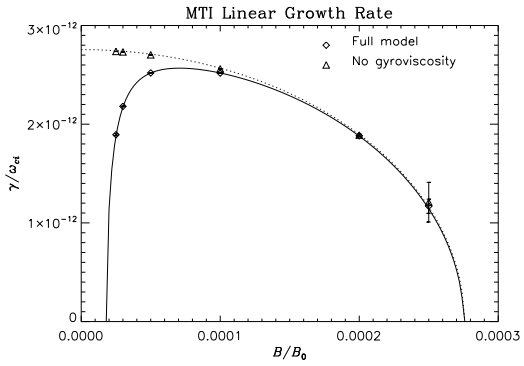

Figure 4.5: The solution to equation (4.21) is plotted versus normalized equilibrium magnetic field strength, both including (solid line) and omitting (dotted line) the FLR contribution. The growth rate is normalized to the ion cyclotron frequency associated with B_0. The data points are results from two-dimensional linear simulations.

is valid), the stabilization due to FLR effects occurs at scales much larger than the ion Larmor radius. Specifically, the equilibrium is stable to perturbations having wavelengths smaller than $\sim \sqrt{\rho_i L}$.

4.3.2 Numerical Simulation

Linear simulations with M3D-C^1 of the MTI using an axisymmetric, extended-MHD code which includes anisotropic heat flux and the full Braginskii form of the gyroviscous stress tensor are presented here. The equilibrium is that considered by Parrish and Stone [79]:

$$n(z) = n_0(1 - z/L_n)^2 \tag{4.25a}$$

$$p(z) = p_0(1 - z/L_n)^3. \tag{4.25b}$$

Physical parameters have been chosen such that the dimensionless parameters $X = 800\pi\sqrt{5/3}$ and $Y = 5$. B/B_0 is varied from $\approx 10^{-5}$–3×10^{-4}, where B_0 is an arbitrary field strength, which leads to values of Z in a range ≈ 0.7–

16. Note that $Z < 5$ (unstable) in the range $1.8 \times 10^{-5} \lesssim B/B_0 \lesssim 2.8 \times 10^{-5}$, and $Z > 5$ (stable) elsewhere. The simulations were run both with and without gyroviscosity, to highlight the difference at low values of B/B_0. Linear growth rates are determined from the simulation results by measuring the exponential growth time of the perturbation amplitudes. The results of these simulations are plotted in figure 4.5 against the solution to equation (4.21), with which they are in excellent agreement.

Chapter 5

Axisymmetric Toroidal Steady-States

As mentioned in chapter 1, an understanding of the steady-states of fusion plasmas, and how to affect that state, is of great importance for designing a fusion reactor. By steady-state is meant the asymptotic statistical behavior of the plasma at infinite time, which may be static (no flow), stationary (a fixed point in parameter space), oscillatory (as with a limit cycle) or turbulent. Ideally one would like to have a predictive capability of what the steady-state of a plasma should be given the external magnetic fields and driving forces in which all quantities are self-consistently determined.

Typically, magnetic equilibria are calculated with pressure and current profiles assumed known *a priori*. Assuming that inertial forces are small, the requirement of force balance is approximately given by $\nabla p = \mathbf{J} \times \mathbf{B}$. In an axisymmetric configuration, this leads to the well-known Grad-Shafranov (GS) equation,

$$\Delta^* \psi = -R^2 p' - II', \tag{5.1}$$

and the condition that p and I are free functions which are constant on magnetic surfaces. (Here primes represent derivatives with respect to ψ.) By specifying the boundary conditions on ψ and the profiles of p and I

(by fitting to experimental data, for example), equation (5.1) determines the magnetic configuration. Numerical methods for the solution of equation (5.1) are well developed and a number of numerical codes exist for its efficient solution [80, 81, 82]. Aside from the fact that there are infinitely many solutions to equation 5.1 when p and I are not both specified, this method gives an incomplete picture of the steady-state, as it only enforces the satisfaction of steady-state force balance. The issues of resistivity, flows, and thermodynamic fluxes are ignored.

It is known that a static toroidal equilibrium is unstable to rotation [83], and therefore flows will be present in the steady-state. While the magnetostatic equilibrium of magnetically confined fusion plasmas are relatively insensitive to the flows, the stability and transport properties of the plasma may be strongly affected by them [84, 85, 86]. More recently, it has been found that strong flows at the plasma edge are stabilizing to resistive wall modes [87, 88] and are correlated with the important L-H transition in tokamaks [89]. Also, it is thought that flow shear may significantly reduce transport due to turbulence by suppressing eddy formation [4, 5]. Therefore it is desirable to develop a method for obtaining steady-states with flow self-consistently included. Here the focus is on obtaining axisymmetric steady-states of a two-fluid plasma model with flow, which may then be used as the basis for three-dimensional stability calculations.

Early steps toward addressing the issue of stationary axisymmetric toroidal equilibria with self-consistent flows were taken by Greene *et al* [90], who obtained equations governing the equilibrium including flows to first order in the inverse aspect ratio using a resistive single-fluid model. These results do not uniquely determine the flows, however; the equilibrium density profile, electrostatic potential, and parallel velocity are left arbitrary. Zehrfeld and Green [91] obtained reduced sets of equations determining ideal MHD equilibria including flow for arbitrary β and magnetic configurations. Hazeltine sought to determine uniquely the electrostatic potential through kinetic the-

ory [92]. Hazeltine's work has been revisited recently by others [93, 94, 95] using drift-ordered fluid theory, including viscosity. The problem of equilibria with flows can also be recast as a problem of minimization of the plasma energy subject to the constraints of invariants like helicity [96, 97] and boundary conditions, which can be shown to yield unique solutions in some cases.

One approach to the numerical calculation of steady-states with flow is the extension of the Grad-Shafranov (GS) method of casting the steady-state ideal MHD equations in terms of free functions of the poloidal flux. This yields the Grad-Shafranov-Bernoulli equations, which are elliptic in the absence of supersonic flows. As with the GS method, the free functions must then be fit to experimental data to obtain a unique equilibrium. This method is complicated by the fact that density is not constant on a magnetic surface in the presence of flows, and the free functions may be complicated combinations of physical variables, and not necessarily continuous. Attempts have been made to include two-fluid effects by assuming that the perturbations introduced by such effects are small [98, 99]. None of these methods include resistive or viscous effects, or sources.

The numerical codes CLIO [100], FINESSE [101], and FLOW [102] have been developed to obtain the stationary equilibria of ideal MHD with flow. Because dissipationless models do not have a unique solution [96], the solutions obtained by these methods requires the *a priori* specification of various thermodynamic profiles. Therefore it is more accurate to say that these codes "reconstruct" rather than "predict" the stationary states. Note also that because these methods solve the time-independent equations, non-stationary steady-states cannot be recovered. CLIO and FLOW have been able to reconstruct such stationary states for JET and NSTX-geometry plasmas, respectively [100, 103].

A more physically motivated method is to evolve numerically the dynamical equations from some initial condition until a steady-state is reached. This method had several advantages over solving directly for the equilib-

rium, as with the Grad-Shafranov-Bernoulli method. First, this method readily admits the inclusion of dissipative and other more complicated terms relatively easily and generally without any algorithmic changes. Second, the same method may be used to observe and investigate the dynamics of the plasma evolution and oscillations in the steady-state. The disadvantages of this method are the relatively large amount of processing time that must be spent to arrive at a steady-state when multiple time-scales are present, and the difficulty of calculating steady-states with very small values of resistivity and viscosity. This approach was taken by Aydemir, who has recently obtained quasi-steady-states of a visco-resistive single-fluid model in low-β plasmas using the numerical code CTD [18, 12].

This general approach is used here, with a significantly more comprehensive physical model than has been used previously for this purpose, including two-fluid effects, gyroviscosity, parallel viscosity, and realistic β. Furthermore, the numerical methods employed in M3D-C^1 allow large enough time steps that steady-states are truly steady on all timescales present in the system, throughout the entire simulation domain. This has not previously been accomplished.

Specifically, the following method for obtaining steady-states is used. The initial conditions for the magnetic field are determined using an ideal-MHD equilibrium with boundary conditions determined by currents in external magnetic coils (outside the simulation domain) appropriate to NSTX, and a specified toroidal current within the simulation domain. The method for obtaining this solution is described in detail in reference [51]. This initial condition satisfies equation (5.1), and is not, in general, a steady-state solution of the two-fluid equations. The system is then time-advanced according to the full two-fluid equations. In order to counteract the resistive dissipation of current, a loop voltage V_L is applied by ramping the value of the poloidal flux ψ on the boundary at a rate $\dot{\psi} = V_L/2\pi$. The loop voltage is regulated by a proportional-integral-derivative (PID) controller to keep the

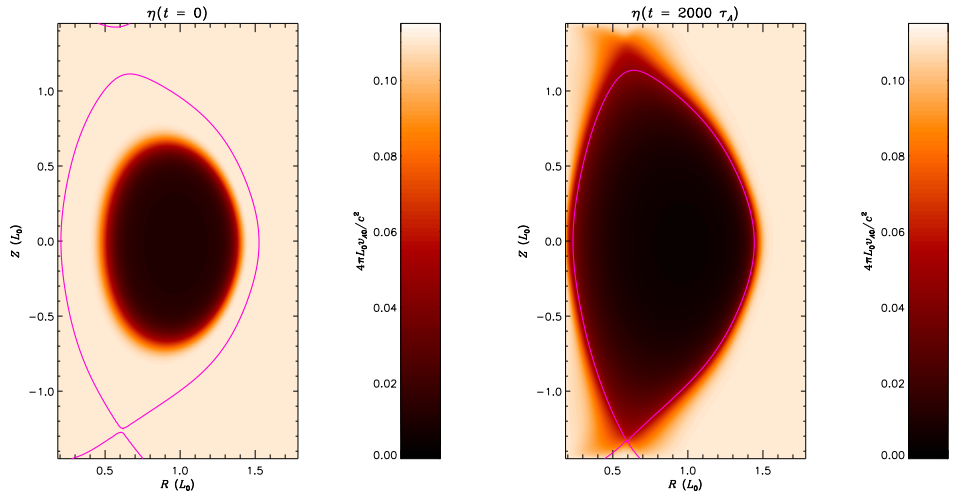

Figure 5.1: The normalized resistivity in the initial conditions (left) and in the final steady-state (right) is shown. In both cases, η ranges from roughly 0.1 at the edge to .004 at the magnetic axis.

toroidal current at a fixed value. This loop voltage also serves to counteract the diffusion of thermal energy out of the domain by causing ohmic (Joule) heating. The thermal conductivity is chosen so that the temperature attains a realistic value in steady-state. Particle loss due to diffusive flux out of the domain is counteracted by a localized particle density source σ near the magnetic axis.

The system of equations considered here are a driven, nonlinear system, and therefore may not have a stationary steady-state, or even a unique steady-state. However, for the cases presented below, which are carried out with relatively large values of dissipation, the system is typically found to relax to a steady-state within $5-10$ resistive periods (η^{-1}). These steady-states are statistically stationary on all timescales present in the model: hydrodynamic, diffusive, and resistive.

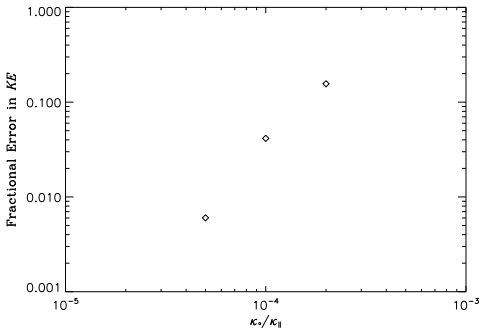

Figure 5.2: The fractional error in steady-state kinetic energy is plotted versus the ratio of the isotropic to parallel heat conduction. The error is calculated relative to the solution for the case where $\kappa_\parallel/\kappa_\circ = 4 \times 10^4$.

5.1 Simulation Parameters

The simulations presented in this chapter have a diverted magnetic field configuration, with geometry, plasma current, temperature, and density profiles typical of NSTX. Resistivity was taken to have the standard collisional form $\eta = \eta_0/T_e^{3/2}$, with results here obtained with η_0 in the range 10^{-4}–10^{-6}. The other transport parameters, $\kappa_\circ$, $\kappa_\parallel$, D_n, μ, and μ_c, were taken to be constant and uniform. Unless otherwise specified, $\kappa_\circ = 200\eta_0$, $\kappa_\parallel/\kappa_\circ = 10^4$, $D_n = 10^{-4}$, $\mu = 10^{-4}$, $\mu_c = 10^{-3}$, and $\mu_\parallel = 0$. (κ is scaled with resistivity in order to achieve temperature profiles roughly independent of η_0.) For two-fluid simulations, the ion skin depth was a realistic value of $d_i = 5.1 \times 10^{-2}$. One-fluid simulations were done by letting $d_i = 0$. Since the gyroviscous force scales with d_i, it is not included in one-fluid simulations. The total plasma current is kept at a (normalized) value of 3.14 by a PID controller. Using the normalization values for NSTX given in appendix A, this is approximately 750 kA.

The heat conduction anisotropy is limited by nonlinear numerical stability considerations. It is found that in NSTX simulations the maximum stable

time step begins to be reduced when $\kappa_\parallel/\kappa_\circ \gtrsim 10^4$. (Simulations of ITER configurations and other higher-aspect ratio geometries allow anisotropies of $\kappa_\parallel/\kappa_\circ \gtrsim 10^6$ without placing onerous restrictions on the time step; this may be to be due to the increased distance between the LCFS and the simulation domain boundary in those cases.) In the simulations presented here, where the perpendicular heat conduction is much greater than the Braginskii value, the solution does not depend strongly on the value of the heat conduction anisotropy above $\sim 10^4$ (see figure 5.2). If the Braginskii values of the thermal conductivities were used, the solution might not be so insensitive, since the perpendicular heat transport would be due primarily to the component of $\mathbf{q}_\wedge$ proportional to the parallel thermal gradient [104]. In the simulations here, where $\kappa_\circ$ is anomalously large, the contribution of $\mathbf{q}_\wedge$ is negligible and $\kappa_\wedge$ is assumed to be zero.

Diffusive particle loss through the boundary is compensated by a localized density source σ, which takes the form

$$\sigma = \frac{\nu_n}{2\pi R \ell_n} \exp\left[-\frac{(R-R_n)^2 + (Z-Z_n)^2}{2\ell_n^2}\right] \tag{5.2}$$

with the injection rate $\nu_n = 6 \times 10^{-4}$ and $\ell_n = 0.1$. The density injection is centered on the high-field side (HFS) of the magnetic axis ($R_0 \approx 0.9$) with $(R_n, Z_n) = (0.6, 0)$, unless otherwise specified.

5.1.1 Boundary Conditions

M3D-C^1 allows a wide range of boundary conditions to be applied. Let $\hat{\mathbf{n}}$ be a vector normal to the simulation domain boundary, and $\hat{\mathbf{t}} = \hat{\mathbf{n}} \times \hat{\varphi}$. For the simulation results presented here, the following boundary conditions were used:

1. No-normal-flow: $\hat{\mathbf{n}} \cdot \mathbf{u} = 0$;
2. No-slip: $\hat{\varphi} \cdot \mathbf{u} = \hat{\mathbf{t}} \cdot \mathbf{u} = 0$;

3. No-current: $\hat{\mathbf{n}} \cdot \mathbf{J} = \hat{\mathbf{t}} \cdot \mathbf{J} = \nabla\varphi \cdot \mathbf{J} = 0$;

4. Constant-density and temperature $\partial_t n = \partial_t T = 0$.

5. Conducting boundaries with toroidal loop voltage: $\partial_t I = 0$, $\partial_t \psi = V_L/2\pi$.

The no-normal-flow boundary ensures that particles are lost (or gained) through the domain boundary only through diffusion. This condition is perhaps not realistic; edge modeling codes such as UEDGE [105] typically employ a sheath boundary condition to model the loss of particles to the divertor plates [47]. No-normal-flow boundary conditions may yield a reasonable approximation to the particle density dynamics assuming that particles lost to the divertor are quickly recycled and re-ionized close to the point at which they are lost. However, because in reality recycled particles are recycled at a much lower temperature than that at which they at lost, the no-normal-flow boundary conditions cause the thermal flux to the divertor to be underestimated.

The no-slip boundary condition is used because it is found to improve numerical stability, though the results are qualitatively the same if this condition is omitted. The boundary condition on the current density is also found to have little effect. It is essential that the temperature be held constant at the boundary in the absence of thermal sinks within the domain; otherwise the system tends toward thermal equilibrium (*i.e.* spatially uniform temperature). Keeping density constant is useful for numerical stability and perhaps more realistic than a no-flux condition, but the results are relatively insensitive to the density boundary conditions.

Recently it has been shown that currents flowing in the scrape-off layer (SOL) and through conducting walls may be destabilizing to resistive wall modes [106] and ideal kink modes [107]. While these instabilities are not present in the absence of non-axisymmetric perturbations, it should be noted that these effects would be excluded by the no-current boundary conditions

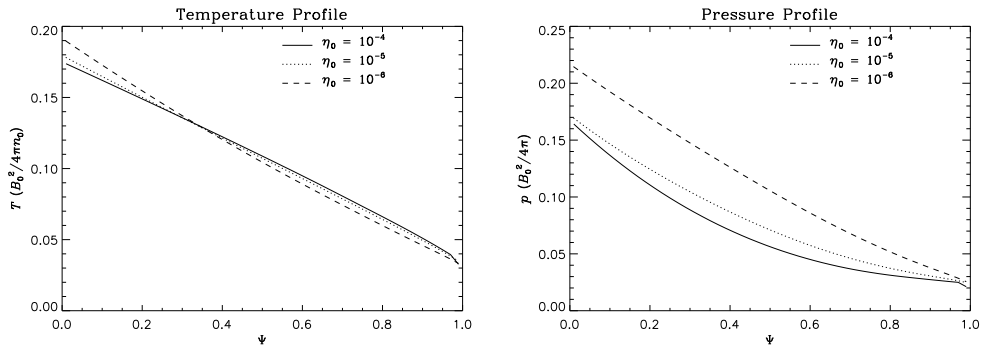

Figure 5.3: The flux-averaged steady-state temperature (left) and pressure (right) profiles as a function of normalized flux Ψ. The magnetic axis is $\Psi = 0$, and the LCFS is $\Psi = 1$.

considered here.

5.2 Thermodynamic Profiles

In steady-state for the parameters investigated here, the energy balance within the last closed flux surface (LCFS)—the magnetic surface farthest from the magnetic axis which does not intersect the domain boundary—is dominated by the balance between ohmic heating and perpendicular thermal diffusive losses (see figure 5.4):

$$\frac{\eta_0}{T^{3/2}} J^2 \approx \nabla \cdot (\kappa_\circ \nabla T). \tag{5.3}$$

Therefore, by keeping $\kappa_\circ/\eta_0$ the same for each simulation, the temperature profile in each simulation is essentially the same in each, as can be seen in figure 5.3. However, the pressure and density profiles differ somewhat among simulations with varying η_0. Due to the increased Pfirsch-Schlüter convective losses at higher resistivity (see section 5.3.1), the core density (and hence pressure) is higher in the low-resistivity cases.

The current profile is determined by the parallel component of Ohm's

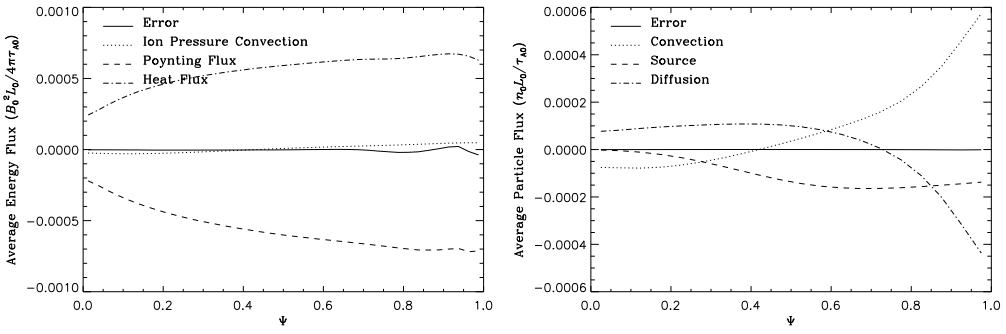

Figure 5.4: The energy balance (left) and particle balance (right) in the steady-state of a two-fluid simulation with $\eta_0 = 10^{-5}$. Positive values indicate outward flux. Smaller terms in the energy balance such as electron pressure convection and viscous heating are suppressed. The Poynting flux is $V_L I_p$, where V_L is the loop voltage and I_p is the plasma current, and represents the energy transferred to the plasma by ohmic heating.

law. The higher core pressure in the low-resistivity cases causes the safety factor at the magnetic axis to drop slightly in those cases, from roughly $q_0 \approx 0.9$ at $\eta_0 = 10^{-4}$ case to $q_0 \approx 0.8$ at $\eta_0 = 10^{-6}$. Two-fluid terms and gyroviscosity are entirely negligible in the particle, radial momentum, and energy balances, and do not directly contribute to cross-field fluxes; therefore the thermodynamic and magnetic profiles are not sensitive to the inclusion of these effects.

The radial electric field, shown in figure 5.5, is found to be negative (inward) throughout the plasma. This is due primarily to the relatively large radial ion pressure gradient. While the Lorentz force is significant in the high-resistivity case in which the resistively driven Pfirsch-Schlüter flows are large, it is negligible in low-resistivity simulations. In other words, the poloidal components of the electric ($\mathbf{E} \times \mathbf{B}$) and diamagnetic drifts are roughly equal and opposite in the low-resistivity cases. In experiments with auxiliary methods of heating (other than ohmic heating) operating in H-mode, it is found that the radial electric field exhibits a dramatic drop at the

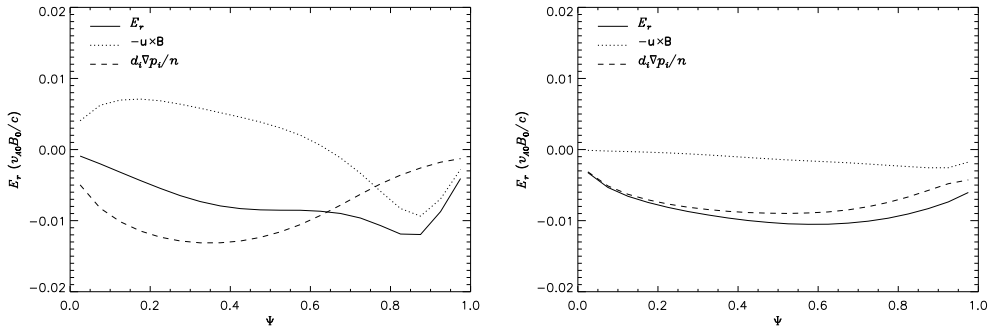

Figure 5.5: The surface-averaged radial electric field in the steady-state with $\eta_0 = 10^{-4}$ (left) and $\eta_0 = 10^{-5}$ (right), as calculated from equation (3.1g). The curve labeled $d_i\hat{\mathbf{r}} \cdot \nabla p_i/n$ is actually $d_i\hat{\mathbf{r}} \cdot (\mathbf{J} \times \mathbf{B} - \nabla p_e)/n$, which is equivalent to $d_i\hat{\mathbf{r}} \cdot \nabla p_i/n$ up to small inertial and viscous effects. Here $\hat{\mathbf{r}} = -\nabla\psi/|\nabla\psi|$ is the outward minor-radial direction.

edge concurrent with the formation of the sharp thermodynamic gradients. The thermodynamic profiles in the simulation results presented here lack such sharp gradients, and are more characteristic of ohmically heated L-mode discharges.

To lowest order, the parallel and poloidal flows depend on the radial electric field. Hazeltine [92] was able to calculate the self-consistent parallel and poloidal flows in the collisional regime from the drift-kinetic equation, and gives an explicit expression for the radial electric field in the large aspect-ratio limit. Attempts have been made to obtain Hazeltine's result from fluid equations by using Mikhailovskii and Tsypin's corrections to the Braginskii equations which are valid in the drift ordering [29, 93]. Much more complicated, implicit results are obtained by Catto and Simakov using this formalism, who find results which differ somewhat from Hazeltine's [94, 95]; these differences are ascribed to improper assumptions about the poloidal variation of the electrostatic potential in Hazeltine's original derivation. It is difficult to compare the results presented here directly with these theories because the theoretical results derive generally from drift-ordered equations

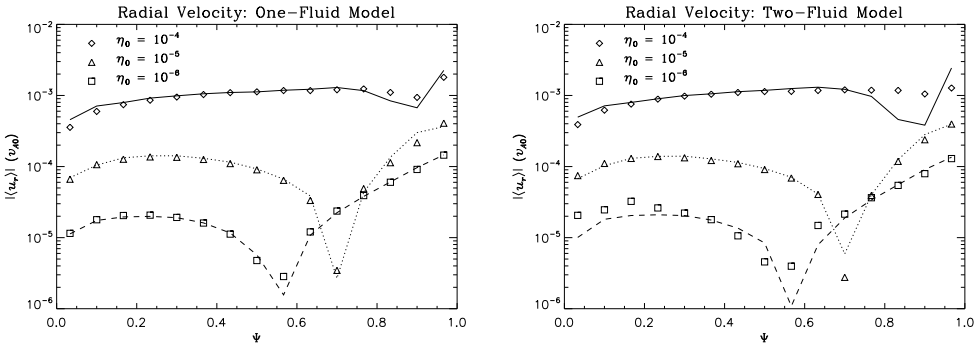

Figure 5.6: The surface-averaged value of $u_r = -\mathbf{u} \cdot \nabla\psi/|\nabla\psi|$ is plotted versus normalized flux ($\Psi = 0$ at the magnetic axis, $\Psi = 1$ at the LCFS), for various values of η_0. *Left*: one-fluid simulations; *right*: two-fluid simulations (including gyroviscosity). Symbols indicate the value of the left side of equation (5.4), and the lines indicate the value of the right side of equation (5.4); both are calculated using simulation results. The minimum in each line represents the point at which the sign of $\langle u_r \rangle$ changes from inward (near the magnetic axis) to outward (near the LCFS).

in the absence of sources, and explicit results are given only in the low-β, circular cross-section limit.

5.3 Flows

5.3.1 Radial Flows

It is well known that resistive diffusion in a toroidal magnetic configuration leads to parallel currents and cross-field convective transport [108]. The radial flows responsible for this transport may be derived from the resistive Ohm's law, assuming ideal force balance and $\nabla \cdot \mathbf{J} = 0$, to be (see appendix B)

$$\mathbf{u} \cdot \nabla\psi = -\frac{V_L}{2\pi}\left(1 - \frac{\langle B_\varphi^2 \rangle}{\langle B^2 \rangle}\right) - \eta p' R^2 \left(1 - \frac{B_\varphi^2}{\langle B^2 \rangle}\right), \tag{5.4}$$

where

$$\langle f \rangle = \frac{\oint_C d\ell \, f/B_p}{\oint_C d\ell / B_p} \tag{5.5}$$

denotes the magnetic surface average. Here $B_p = |\nabla\psi|/R$ is the poloidal magnetic field strength and $d\ell$ is a differential along the curve C formed by the intersection of a magnetic surface with a poloidal plane ($\varphi = const$). In figure 5.6, the actual values of $\mathbf{u} \cdot \nabla\psi$ obtained by M3D-C^1 are compared with the values obtained from equation (5.4) given the computed steady-state magnetic field. For the cases which reach a steady-state, the agreement is generally excellent, with some discrepancy near the LCFS where stronger poloidal variations in pressure begin to occur. The $\eta_0 = 10^{-6}$ case remains oscillatory in the core in the two-fluid model, and $\langle u_r \rangle$ is seen to disagree slightly with the Pfirsch-Schlüter theory in that case.

5.3.2 Toroidal Flows

The steady-state toroidal flow patterns in a series of simulations are shown in figure 5.7. The dominant feature of the high-resistivity cases is the roughly up-down antisymmetric edge flow. As resistivity is uniformly decreased, the strength of the up-down antisymmetric edge flow decreases, and is dominated by an up-down symmetric toroidal flow in the core when $\eta_0 = 10^{-6}$. (Though there exist small oscillations in this particular case, this toroidal rotation feature is persistent and essentially stationary.) This rotation is a consequence of gyroviscosity and is explained in section 5.3.3. This effect becomes more evident at lower resistivity, when the resistively driven flows are smaller. In the absence of gyroviscosity, the toroidal flow in the core is very weak and essentially up-down antisymmetric throughout (*i.e.* no net toroidal flow in the core). It is also shown in section 5.3.3 that this rotation is dependent on the location and magnitude of density injection.

Gyroviscosity is also found to cause highly regular oscillations in some high-resistivity steady-states. These oscillations are damped by isotropic

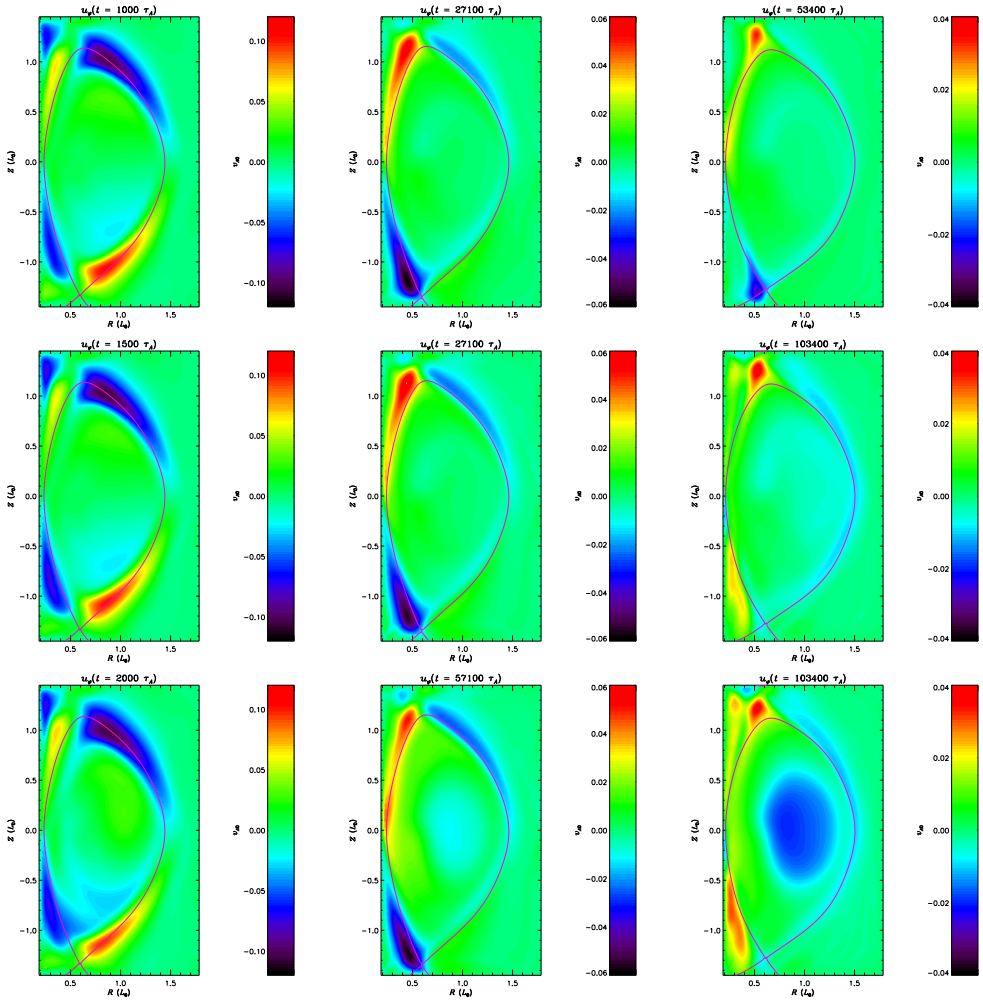

Figure 5.7: Plots of the toroidal velocity for (from left to right) $\eta_0 = 10^{-4}$, 10^{-5}, and 10^{-6}. *Top row*: one-fluid model, without gyroviscosity. *Middle row*: two-fluid model, without gyroviscosity. *Bottom row*: two-fluid model, with gyroviscosity.

viscosity, and may persist for long periods when the isotropic viscosity is relatively small (see figure 5.13). The frequency and amplitude of this oscillation are independent of δt and δx. Furthermore, the amplitude appears to be independent of the initial conditions, which suggests that the oscillations are nonlinear in nature. This phenomenon is not yet understood, and is described in more detail in section 5.3.5. Neither the core toroidal rotation nor the steady oscillation phenomenon are present in the absence of gyroviscosity.

The isotropic viscosity plays an important role in the character and magnitude of the toroidal flows. An analysis of simulation results shows that the dominant terms in the local angular momentum balance changes as viscosity is decreased. For the $\eta_0 = 10^{-4}$ cases without gyroviscosity or parallel viscosity, the balance is between the $\mathbf{J} \times \mathbf{B}$ force and the viscosity when $\mu \lesssim 10^{-4}$; when $\mu \gtrsim 10^{-4}$, the balance is dominantly between the $\mathbf{J} \times \mathbf{B}$ torque and convection. For most of the simulation results presented here, the isotropic viscosity is dominantly limiting the toroidal flow because only in these cases is the kinetic energy found to come to a fully stationary equilibrium.

Edge Flows

Up-down antisymmetric flows were found to occur in the resistive SOL in simulations of a resistive one-fluid model by Aydemir [12]. These flows were found to be quite strong, with maximum speeds of order 100 km/s, when the Lundquist number of the SOL is of order 10. Results found here exhibit toroidal edge flows, similar in both character and magnitude to those found by Aydemir, in cases where the SOL Lundquist number is comparable.

It is well known that the angular velocity of the plasma must be constant on a magnetic surface given an ideal, one-fluid Ohm's law [109]. In a resistive plasma, this restriction is lifted, and the poloidal variation of the angular velocity may be expected to be proportional to the resistivity. This poloidal variation is determined by the toroidal component of Faraday's law (equa-

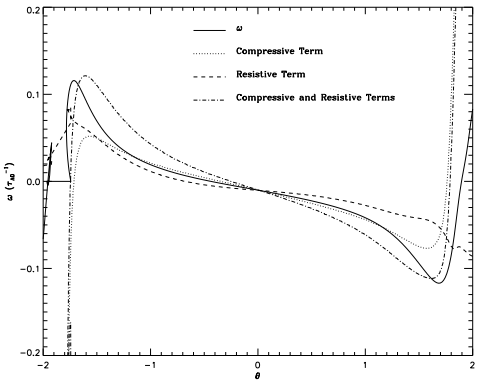

Figure 5.8: Comparison of the terms of equation (5.9) after field-line integration, using data from just outside the LCFS ($\Psi = 1.01$) of a two-fluid simulation. The θ coordinate is simply the polar angle from the LFS horizontal midplane ($\theta = 0$) about the magnetic axis. The field lines intersect the computational domain boundary at roughly $\theta \approx \pm 1.8$.

tion (2.8f)), the dominant balance of which is, in a resistive steady-state,

$$\mathbf{B} \cdot \nabla \omega = -\nabla \cdot \left[\frac{1}{R^2} \eta \nabla I \right] + \frac{1}{R^2} I \nabla \cdot \mathbf{u} \tag{5.6}$$

$$= \eta \frac{1}{R} J_\varphi I' - (\eta I')' B_p^2 - \frac{1}{R^2} n' I \mathbf{u} \cdot \nabla \psi, \tag{5.7}$$

where primes represent derivatives with respect to ψ. The $I \nabla \cdot \mathbf{u}$ term may be important in cases with a strong density gradient at the edge, and is therefore retained. Equation (5.7) is obtained using equation (2.8a) and assuming I, η, n are constant along field lines, which is generally well satisfied throughout most of the simulation domain (including outside the separatrix). Thus, in the resistivity dominated case (as in the plasma edge), the toroidal angular velocity scales linearly with resistivity. Equation (5.7) may be simplified by using equation (5.4). The flows are observed to be strongest just outside the LCFS, where equation (5.4) is not well-defined, since surface-averages cannot be correctly performed outside there. However, one may simplify

equation (5.4) under the assumptions that $|B| \sim |B_\varphi| = I/R$, and $\langle R \rangle \approx R_0$, where R_0 is the major radius of the magnetic axis, yielding

$$\mathbf{u} \cdot \nabla \psi \approx -\eta p'(R^2 - R_0^2). \tag{5.8}$$

Using this equation, and making the further assumption that J_φ is negligible in the SOL, one may write equation (5.7) as

$$\mathbf{B} \cdot \nabla \omega_e \approx -(\eta I')' B_p^2 + I \eta p' \frac{n'}{n} \left(1 - \frac{R_0^2}{R^2}\right). \tag{5.9}$$

This equation may then be integrated along a field line to obtain the edge angular velocity, ω_e. The result of doing this using data from the two-fluid simulation with $\eta_0 = 10^{-4}$ is shown in figure 5.8. It can be seen from that figure that equation (5.9) gives a good estimate of the poloidal variation of the angular velocity in this case. This equation is useful because it does not depend on any other component of the flow or on the electrostatic potential, but only on quantities which may be measured relatively accurately in experiment or determined accurately through magnetostatic equilibrium reconstruction.

5.3.3 Core Flows

Within the core of the plasma column, the situation differs from that in the edge due to the lower resistivity in the core. Therefore the core may be more closely approximated by the ideal MHD description. The Pfirsch-Schlüter theory for the radial flows shows that $\mathbf{u} \cdot \nabla \psi \sim \eta$. Thus to zeroth order in the resistivity, one may write

$$\mathbf{u}_0 = \Omega R^2 \nabla \varphi + G \mathbf{B}. \tag{5.10}$$

In a stationary steady-state, Ampère's law together with the ideal Ohm's law,

$$0 = -\nabla \times (\mathbf{u}_0 \times \mathbf{B}), \tag{5.11}$$

yields the constraint that $\Omega = \Omega(\psi)$. Continuity, equation (3.1a), then requires

$$\mathbf{B} \cdot \nabla(nG) = \sigma + D_n \nabla^2 n. \tag{5.12}$$

In the absence of diffusion or a density source, one would then have $K = nG$ constant on magnetic surfaces, which is the standard result [109, 110]. It is then typically argued that K, to which the rate of poloidal rotation is proportional, must be negligible due to the neoclassical poloidal damping. This does not hold in the case considered here, however, where a density source exists and therefore $\mathbf{B} \cdot \nabla K = \sigma + D_n \nabla^2 n$. The poloidal variation of the toroidal angular momentum density is therefore

$$\mathbf{B} \cdot (nV) = \Omega \mathbf{B} \cdot \nabla(nR^2) + (\sigma + D_n \nabla^2 n) I, \tag{5.13}$$

assuming that I is constant on magnetic surfaces. (This is satisfied to $\mathcal{O}(u^2/v_{ti}^2)$ due to inertial corrections to force balance, or $\mathcal{O}(\sigma \tau_c u / n v_{ti})$ due to the σ correction, where $\tau_c = L_0/v_{ti}$ and L_0 is the pressure gradient scale length.)

Note that surface-averaging equation (5.12) yields the solubility condition that $0 = \langle \sigma + D_n \nabla^2 n \rangle$. Therefore no stationary steady-state can exist in this ordering without $D_n \gtrsim L_n^2/n$. Of course, this is due to the fact that particles injected into a magnetic surface may only leave through diffusion or through cross-field convective flux, the magnitude of which is proportional to resistivity.

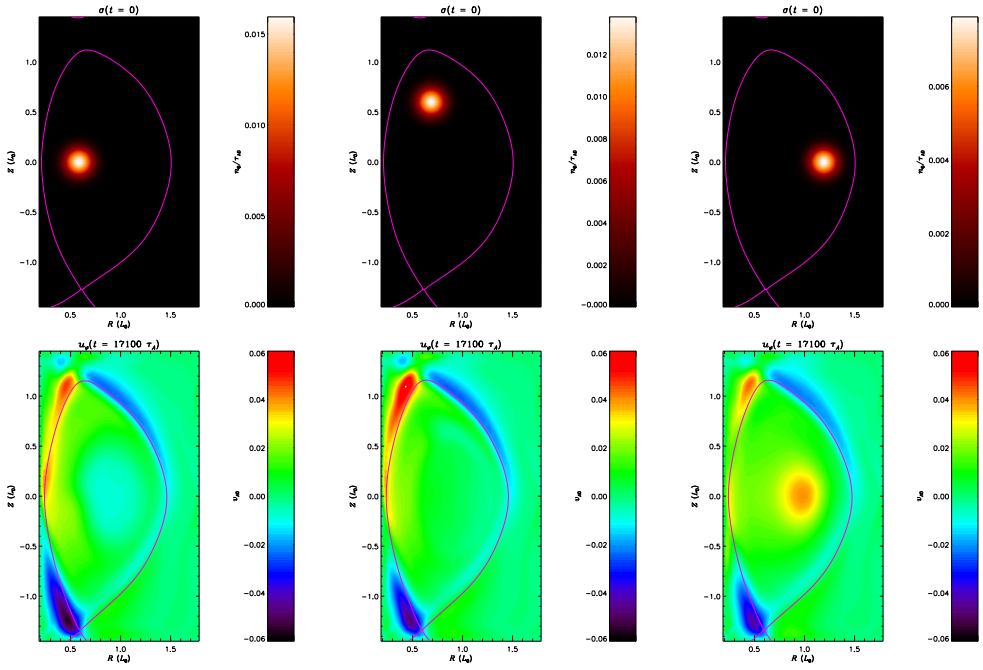

Figure 5.9: The gyroviscous core rotation is shown to be dependent on the density injection location. *Top row*: the density source, σ is shown for three different simulations, all with $\eta_0 = 10^{-5}$. *Bottom row*: the steady-state toroidal velocity corresponding to the density sources in the top row.

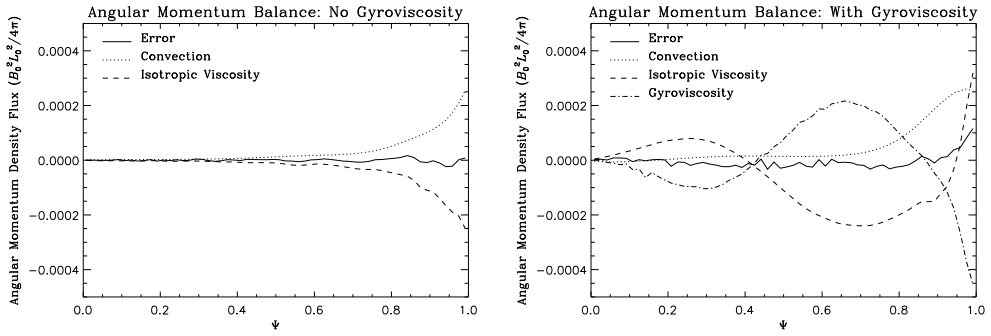

Figure 5.10: The angular momentum density flux, integrated over each flux surface, is shown for the steady-state without (*left*) and with (*right*) gyroviscosity. Positive values represent outward flux.

Gyroviscous Core Rotation

The inclusion of gyroviscosity is found to lead to significant changes to the toroidal flows in the plasma core in many cases. As can be seen in figure 5.7, the most prominent effect of gyroviscosity is an up-down symmetric toroidal rotation in the core. The direction and magnitude of this rotation is dependent on the position and magnitude of the density source, as will be shown below.

The angular momentum balance calculated from the steady-state solutions obtained by simulations with and without gyroviscosity is shown in figure 5.10. In this figure the angular momentum flux due to gyroviscosity is

calculated using an approximate form of the gyroviscosity:

$$
\begin{aligned}
-R^2\nabla\varphi\cdot\nabla\cdot\Pi_\wedge \approx & \left[\frac{R^2p_iI}{B^2}\left(1-\frac{3B_p^2}{2B^2}\right),\frac{u_\varphi}{R}\right] \\
& + \frac{p_i}{2B^2}\left[u_p,|\nabla\psi|^2\right] - u_p\left[\frac{p_i}{2B^2},|\nabla\psi|^2\right] \\
& - \frac{p_i}{B^2}\left(\frac{1}{R}\left\langle R\left[u_p,\psi\right],\psi\right\rangle + \Delta^*\psi\left[u_p,\psi\right]\right) \\
& + u_p\left(\frac{1}{R}\left\langle R\left[\frac{p_i}{B^2},\psi\right],\psi\right\rangle + \Delta^*\psi\left[\frac{p_i}{B^2},\psi\right]\right) \\
& - \frac{3Rp_i}{B^2}\left(1-\frac{B_p^2}{B^2}\right)\left[\frac{1}{R^2}\psi_R u_p,\psi\right] + \frac{1}{R^4}\left[R^4K_1,\psi\right] - \left[\frac{3B_p^2}{B^2}K_1,\psi\right] \\
& - R^2\left[\frac{1}{R^2}K_2,\psi\right] + R\left[\frac{1}{R^2},K_3\right] - \left(K_4\Delta^*\psi + \langle K_4,\psi\rangle\right)
\end{aligned}
\tag{5.14}
$$

where

$$
\begin{aligned}
K_1 &= \frac{p_i}{2B^2}\left(\langle u_p,\psi\rangle + u_p\Delta^*\psi\right) && \text{(5.15a)}\\
K_2 &= u_p\left(\left\langle\frac{p_i}{B^2},\psi\right\rangle + \frac{p_i}{B^2}\Delta^*\psi\right) && \text{(5.15b)}\\
K_3 &= 3v_p\frac{p_i}{B^4}\left(B_p^2\Delta^*\psi - \frac{1}{2}\left\langle B_p^2,\psi\right\rangle\right) && \text{(5.15c)}\\
K_4 &= \frac{p_i}{2B^2}\left(R^3\left[\frac{u_p}{R^3},\psi\right] - \frac{3RB_p}{B^2}\left[\frac{u_pB_p}{R},\psi\right]\right) && \text{(5.15d)}
\end{aligned}
$$

and

$$
u_p = \frac{\mathbf{u}\cdot\mathbf{B}_p}{B_p^2}. \tag{5.16}
$$

(Note that u_p does not have units of velocity.) Here the following shorthand "Poisson bracket" and "inner product" notation has been used:

$$
\begin{aligned}
[a,b] &= \nabla\varphi\cdot(\nabla a\times\nabla b)\\
\langle a,b\rangle &= \nabla a\cdot\nabla b.
\end{aligned}
$$

Equation (5.14) is equivalent to the Braginskii form in the limit that $\mathbf{u}\cdot\nabla\psi = 0$. The full form and the above approximate form are somewhat unwieldy to deal with analytically; therefore it is advantageous to use the gyroviscous cancellation approximation (see section 2.2.2), which in normalized units is given by:

$$\nabla \cdot \Pi_\wedge \approx d_i \nabla \times \left(\frac{p_i}{B^2}\mathbf{B}\right) \cdot \nabla \mathbf{u}. \tag{5.18}$$

The toroidal component of the gyroviscous force is therefore approximately

$$-R\nabla\varphi \cdot (\nabla \cdot \Pi_\wedge) \approx d_i \left[\frac{p_i I}{B^2}, u_\varphi\right] + d_i(\mathbf{u}\cdot\nabla R)\nabla \cdot \left(\frac{p_i}{B^2}\frac{\nabla\psi}{R^2}\right). \tag{5.19}$$

Near the magnetic axis one may assume that p_i and I are essentially constant, and $B \approx B_\varphi = I/R$. Thus

$$-R\nabla\varphi \cdot (\nabla \cdot \Pi_\wedge) \approx -2d_i\frac{p_i}{I}\frac{\partial u_\varphi}{\partial Z} + d_i\frac{p_i}{I^2}(\mathbf{u}\cdot\nabla R)\nabla^2\psi. \tag{5.20}$$

And finally, assuming that $|\nabla\psi|/R \ll |\nabla^2\psi|$, which must be true near the magnetic axis, one may write $J_\varphi = -\Delta^*\psi/R \approx -\nabla^2\psi/R$, so that

$$-R\nabla\varphi \cdot (\nabla \cdot \Pi_\wedge) \approx -d_i\frac{p_i}{I}\frac{\partial u_\varphi}{\partial Z} - d_i\frac{Rp_i}{I^2}(\mathbf{u}\cdot\nabla R)J_\varphi. \tag{5.21}$$

The second term on the RHS of equation (5.21) provides a force that is always dominantly in the counter-current direction since the resistive Pfirsch-Schlüter flows are always such that $\mathbf{u}\cdot\nabla R$ is dominantly positive (at least, in a flux-averaged sense).

However, the first term on the RHS of equation (5.21) is by far the dominant term in the simulations presented here, due to the predominantly toroidal direction of the flow in the core. In the core, an inverse aspect ratio expansion becomes accurate even for low aspect-ratio devices. It may also be assumed that the flux surfaces are concentric and circular to the lowest order in the inverse aspect ratio $\epsilon = r/R_0$. Defining the coordinate system

(r, ϕ, θ), such that

$$r = \sqrt{(R - R_0)^2 + (Z - Z_0)^2} \tag{5.22}$$

$$\theta = \arctan\left[(Z - Z_0)/(R - R_0)\right], \tag{5.23}$$

Then using equation (5.13) and assuming that n is constant on magnetic surfaces, then to lowest order in ϵ,

$$-2d_i \frac{p_i}{I} \frac{\partial u_\varphi}{\partial Z} = -2d_i p_i \frac{\sigma + D_n \nabla^2 n}{n\psi'} \cos\theta. \tag{5.24}$$

Here $\psi' = \partial_r \psi$, which has the opposite sign of I_φ (assuming ψ is a monotonic), and therefore $\psi' = -\text{sign}(J_\varphi)|\nabla\psi|$ to lowest order in ϵ. Surface-averaging gives

$$-\left\langle 2d_i \frac{p_i}{I} \frac{\partial u_\varphi}{\partial Z} \right\rangle = \frac{2d_i p_i}{n|\nabla\psi|} \text{sign}(J_\varphi) \left\langle \sigma \cos\theta \right\rangle. \tag{5.25}$$

Thus the direction of toroidal force in the core due to gyroviscosity is dependent only on $\text{sign}(J_\varphi) \langle \sigma \cos\theta \rangle$, and therefore results in a counter-current rotation for HFS fueling, or a co-current rotation for LFS fueling. This is in agreement with the results presented in figure 5.9, and also with other simulation results (not shown) which show that for a given fueling location, the direction of rotation is independent of the toroidal field direction, but flips when the toroidal current is flipped.

While this gyroviscous torque is strongest at the location of the density source, the resulting rotation spreads inward to the magnetic axis through isotropic (perpendicular) viscous coupling, since there are no strong competing torques there. Thus the steady-state rotation is roughly uniform within the fueling surface. The magnitude of the rotation in steady-state is determined by the viscosity in the simulations presented here (see figure 5.10). In cases where the viscosity is sufficiently small, the steady-state rotation rate may be limited instead by the ion inertial force, but is unlikely to reach a stationary steady-state in that case.

It should also be noted that it has been shown that the Mikhailovskii-Tsypin corrections to the gyroviscous stress, which are not considered here, have been shown in some cases to diminish the importance of the gyroviscosity in toroidal angular momentum transport, sometimes significantly [93]. It is not obvious how these corrections should affect the phenomenon described above, which depends on the presence of a particle source; this is a matter for future research.

5.3.4 Poloidal Rotation

Vector plots of the poloidal velocity for various resistivities and models are shown in figure 5.11. In the high resistivity ($\eta_0 = 10^4$) case, these flows are dominated by the Pfirsch-Schlüter flows across the magnetic surfaces from the HFS to the LFS, with strong vertical return flows along the center stack toward the horizontal mid-plane. These observations are in agreement with both the observations that fuel injection is significantly more efficient from the HFS than from the LFS, and that the injection from the HFS corners is as efficient as injection from the HFS mid-plane [111]. As resistivity is decreased, this convection pattern is no longer permitted since the cross-surface flows are proportional to the resistivity; the poloidal flows are instead dominated by a poloidal rotation in the electron diamagnetic drift direction.

When gyroviscosity is included, a new rotation in the core becomes apparent. This is due to the gyroviscous rotation effect described in section 5.3.3, in which the density injection leads to a toroidal force, the sign of which depends on the location of the density injection and on the sign of the toroidal current density. This toroidal force drives a parallel flow. The simulations in figure 5.11 are such that the toroidal gyroviscous force is in the negative $\hat{\varphi}$ direction. Since $B_\varphi < 0$ in this case, the poloidal component of this flow is in the ion diamagnetic direction. In the case where the density injection is moved to the LFS, for example, this poloidal rotation would be in the electron diamagnetic direction, thereby enhancing the ambient poloidal flow.

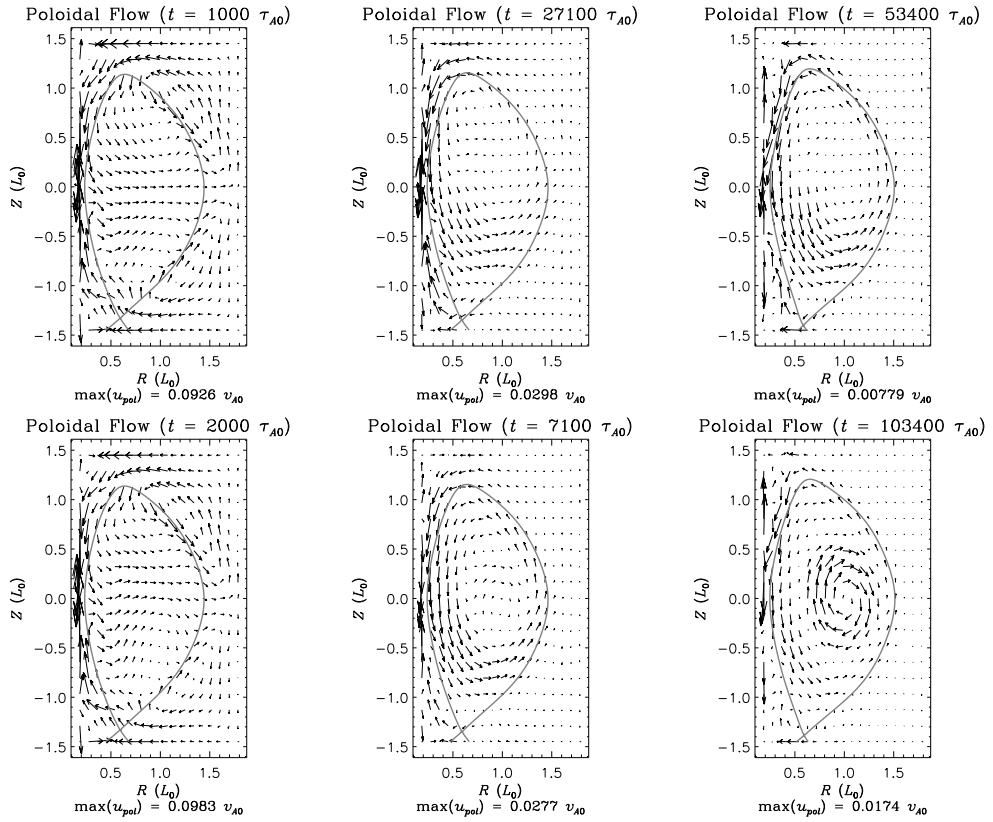

Figure 5.11: Plots of the poloidal velocity for (from left to right) $\eta_0 = 10^{-4}$, 10^{-5}, and 10^{-6}. *Top row*: one-fluid model, without gyroviscosity. *Bottom row*: two-fluid model, with gyroviscosity. As with the toroidal velocity, the results using a two-fluid model without gyroviscosity are essentially identical to that using a one-fluid model without gyroviscosity. In all cases, $\mu_\parallel = 0$.

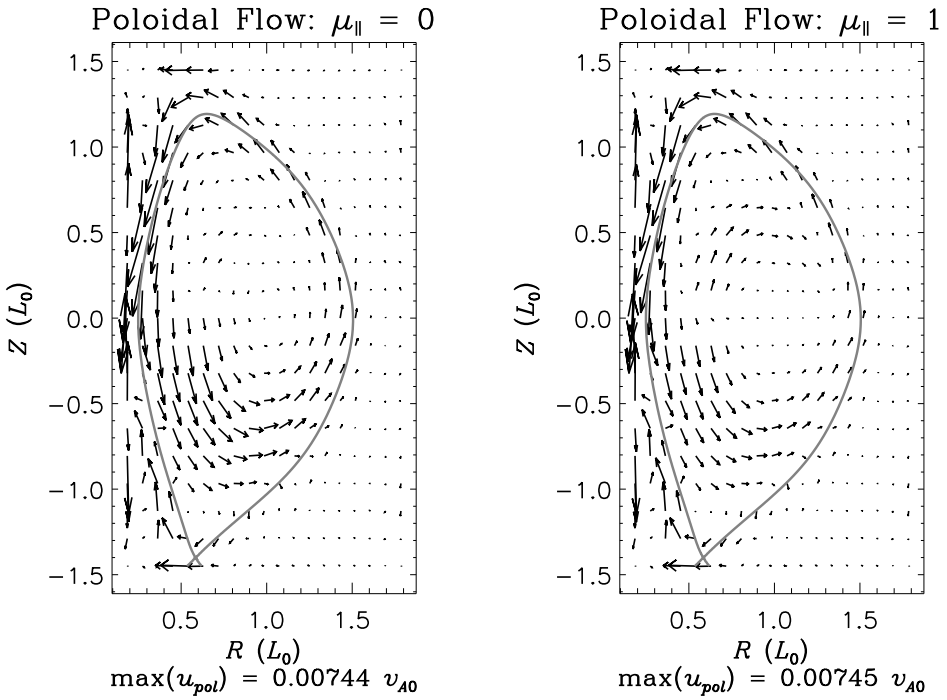

Figure 5.12: The poloidal projection of the velocity without (left) and with (right) parallel viscosity, in the one-fluid case where $\eta_0 = 10^{-6}$.

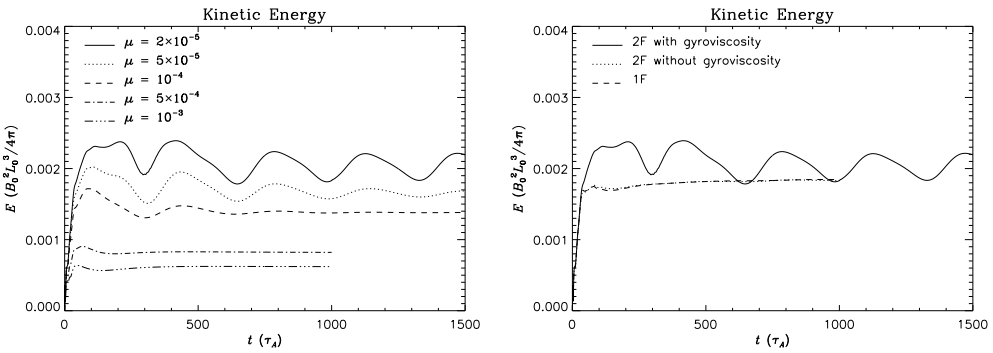

Figure 5.13: *Left*: The total kinetic energy versus time for the two-fluid model, including gyroviscosity, for various values of isotropic viscosity μ. *Right*: The total kinetic energy for various models—one-fluid (without gyroviscosity), two-fluid without gyroviscosity, and two-fluid with gyroviscosity—at $\mu = 2 \times 10^{-6}$. These results are all from simulations having $\eta_0 = 10^{-4}$.

The results shown in figure 5.11 were obtained with $\mu_\parallel = 0$. The dominant effect of parallel viscosity in a nonlinear NSTX-geometry simulation using a one-fluid model is shown in figure 5.12, in which the poloidal flow is plotted for steady-states obtained with and without parallel viscosity (both without gyroviscosity). It can be seen that parallel viscosity has the effect of reducing the poloidal rotation, resulting in a more closely up-down symmetric flow. The parallel viscosity also strongly damps the poloidal flows associated with the gyroviscous rotation, but not the toroidal component of those flows. The dominant features of the toroidal velocity are found to remain essentially unchanged by parallel viscosity.

5.3.5 Gyroviscous Oscillation

As mentioned previously, the introduction of gyroviscosity leads to very regular oscillations in the total kinetic energy. This oscillation is not yet understood, but will be characterized here. Some observations:

1. The frequency of the oscillation is almost precisely proportional to the

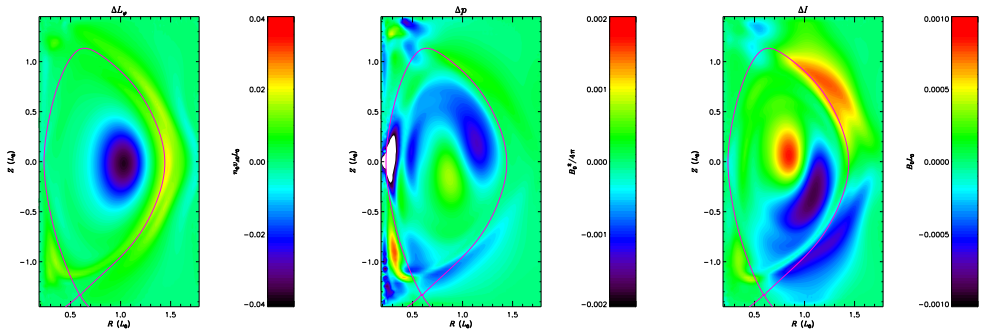

Figure 5.14: The difference between the values at the peak and trough of the gyroviscous oscillation of (from left to right) the toroidal angular momentum density L_φ, the pressure p, and the toroidal magnetic field $I = RB_\varphi$. Note that the "equilibrium" toroidal field is negative, so negative values of ΔI indicate a strengthening of the field.

resistivity, with period a period of $130\tau_{A0}$ (to within a few percent) for $\eta_0 = 2 \times 10^{-4}$ and $260\tau_{A0}$ for $\eta_0 = 10^{-4}$.

2. Increasing the density diffusion coefficient or the viscosity μ damps the oscillation. Increasing the compressional viscosity μ_c does not.

3. The necessary and sufficient component of the gyroviscosity is that part of the toroidal gyroviscous force which depends on the parallel viscosity.

4. The $\mathbf{u} \cdot \nabla \mathbf{u}$ term must be present in the momentum equation.

5. The steady-state amplitude of the oscillation seems to be independent of initial conditions. This suggests that it is a nonlinear phenomenon.

A sense of the eigenfunctions may be gained by observing the difference between each field at a peak and trough of the oscillation. Some of these approximate eigenfunctions are shown in figure 5.14, where it can be seen that the eigenfunctions have a fairly complicated, nonlocal structure. Indeed, there appear to be two separate regions of oscillation: in the core (with both

$m = 0$ and $m = 1$ components) and at the edge. This makes it very difficult to perform an analytic linear eigenmode calculation.

Given the dependence on the resistivity of this oscillation, and its prominence only in the high-resistivity cases, one might speculate that the Pfirsch-Schlüter flows play an important role. This is supported by the fact the period of the oscillation is close to the rotation period of the up-down symmetric poloidal convection cells present in these high-resistivity cases (this rotation period is not well defined, but can be roughly estimated using the length of the path formed by the mid-plane and the upper or lower half of the LCFS, and the average velocity along that path). A more complete understanding of this oscillation will be the goal of future work. In any case, this oscillation is unlikely to be observable in fusion-temperature reactors, in which the resistivity is several orders of magnitude smaller than the lowest resistivity in which it has been observed in simulations, $\eta_0 \sim 5 \times 10^{-5}$.

5.3.6 Net Toroidal Angular Momentum

Experimental results from ohmic discharges (in which no momentum is injected into the plasma) show that net toroidal rotation may be present in the steady-state [112, 113]. This rotation is usually in the counter-current direction, and is found to depend on the direction of the ion grad-B drift relative to the divertor x-point. In Alcator C-mod experiments with single-null configurations, this rotation is 10-20 km/s in the case where the grad-B drift is toward the divertor, and 30-40 km/s when the drift is away from the divertor. It has also been found experimentally that the H-mode is more easily accessed when the ion grad-B drift is toward the divertor than when it is away [114]. These results are not understood.

In M3D-C^1 simulations of NSTX-like discharges a net toroidal angular momentum also arises, and is found to depend on the direction of the ion grad-B drift relative to the divertor x-point. Furthermore, when two-fluid effects are included, the steady-state angular momentum is found to be pref-

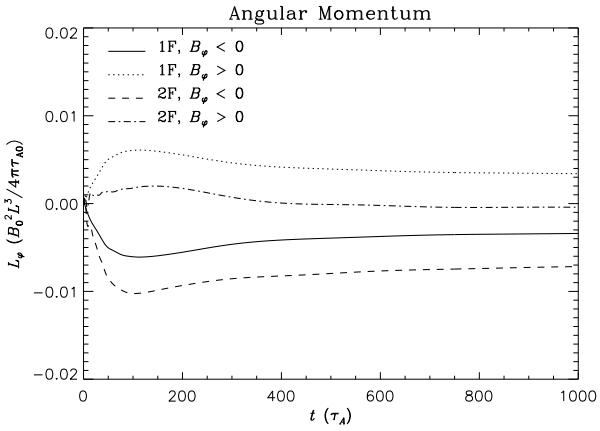

Figure 5.15: The total angular momentum in simulations using the one- and two-fluid models, with positive and negative values of B_φ. The ion $\mathbf{B} \times \nabla \mathbf{B}$ drift is downward (toward the x-point) for $B_\varphi < 0$, and upward for $B_\varphi > 0$.

erentially in the counter-current direction. These results are shown in figure 5.15. In this figure, it can be seen that with the two-fluid model, the overall toroidal angular momentum is greater in the case with $B_\varphi < 0$ (ion grad-B drift toward the divertor) than that with $B_\varphi > 0$; this disagrees with the results from Alcator C-mod.

In the two-fluid model, the toroidal angular momentum obeys the conservation equation

$$\frac{\partial (nR^2\omega)}{\partial t} + \nabla \cdot \left[R^2 \left(n\mathbf{uu} - \mathbf{BB} + \Pi \right) \cdot \nabla\varphi \right] = 0, \tag{5.26}$$

where $\omega = u_\varphi / R$ is the angular velocity The torque density due to isotropic viscosity is

$$\nabla \cdot \left[R^2 \Pi_\circ \cdot \nabla\varphi \right] = \nabla \cdot \left(\mu R^2 \nabla\omega \right). \tag{5.27}$$

In the case considered here, where the boundary conditions are such that $\hat{\mathbf{n}} \cdot \mathbf{u} = 0$ (no normal flow) and $R^2 \mathbf{B} \cdot \nabla\varphi$ is uniform on the boundary, the only nonzero contribution to the flux of toroidal angular momentum through

the simulation domain boundaries is due to viscosity. Analysis of the torque density shows that the main region of viscous torque in these simulations is near the divertors at the top and bottom of the simulation domains. Since the magnetic geometry is not up-down symmetric, the viscous drag on the flows near the lower divertor region are greater than those oppositely directed flows in the upper region, leading to a net torque on the plasma.

The one-fluid model is exactly invariant under the transformation $B_\varphi \to -B_\varphi$ and $u_\varphi \to -u_\varphi$. Therefore, reversal of the toroidal field direction reverses the direction of the toroidal rotation in the steady-state. If the plasma were up-down symmetric, there could be no net torque on the plasma in this model, since all angular momentum density flux through the upper half of the domain boundaries would necessarily cancel that through the lower half boundaries. However, the plasma is not up down symmetric, but is in a lower single null (LSN) configuration. In this configuration, the plasma is closer to the lower boundary, and hence the viscous coupling between the flows driven at the lower edge of the plasma and the lower boundary is greater than that at the upper edge. Thus viscous losses through the boundary cause the plasma to acquire a net angular momentum in the direction opposite to that of the angular momentum in the lower edge. In the typical case where $B_\varphi < 0$, the angular momentum density of the lower edge is positive, and thus the net angular momentum of the plasma should be negative. Again, this effect should change signs under reversal of the toroidal field direction. This is what is observed in these simulations (see figure 5.15). It is also possible to reduce or even reverse the sense of the rotation by moving the upper boundary down very close to the top of the plasma (without changing the LSN configuration).

The two-fluid terms break the invariance of the model to the transformation $B_\varphi \to -B_\varphi$ and $u_\varphi \to -u_\varphi$. Therefore, it is possible for the two-fluid terms to lead to a net torque on the plasma which is independent of the sign of B_φ. The Hall term leads to the development of up-down symmetric

poloidal surface currents, even in an initially symmetric magnetic configuration. This results in a symmetric contribution to the $\mathbf{J} \times \mathbf{B}$ force, which is independent of the direction of the initial toroidal field.

To understand this, it is necessary to understand the poloidal currents at the boundary. The current profile expands as it relaxes from its initial conditions, causing the toroidal field to be compressed against the conducting boundaries as the plasma column expands toward the wall. In the simulations, in which no current is allowed to flow in the boundary surface, this compression leads to surface currents in a boundary layer. In this boundary layer one may write

$$\nabla B_\varphi^2 = -\alpha \hat{\mathbf{n}}, \tag{5.28}$$

where $\hat{\mathbf{n}}$ is the outward normal unit vector and α is some positive value (assuming that $\beta_{pol} < 1$, so that the toroidal field within the plasma is greater than that in the vacuum region, as is the typical case for tokamaks [115, 25]). Now let $\mathbf{B}^{(1)}$ be the solution for the magnetic field in the one-fluid model. Then the contribution to the magnetic field from two-fluid effects is $\mathbf{B}^{(2)} = \mathbf{B} - \mathbf{B}^{(1)}$. In the case that $|\mathbf{B}^{(2)}|/|\mathbf{B}^{(1)}| \sim d_i \ll 1$, the $\mathcal{O}(d_i)$ correction equation from equation (2.8f) is

$$\frac{\partial \mathbf{B}^{(2)}}{\partial t} = -d_i \nabla \times \left[\frac{1}{n} (\mathbf{J}^{(1)} \times \mathbf{B}^{(1)} - \nabla p_e) \right]. \tag{5.29}$$

In the absence of density and pressure gradients near the boundary, the toroidal component of equation (5.29) is

$$\frac{\partial I^{(2)}}{\partial t} = -\frac{d_i}{n} R^2 \mathbf{B}^{(1)} \cdot \nabla \left(\frac{J_\varphi^{(1)}}{R} \right) + \frac{d_i}{nR^2} \frac{\partial (I^{(1)})^2}{\partial Z}. \tag{5.30}$$

Restricting the analysis to boundary layers near the edge, one may ignore derivatives acting on R which does not change rapidly in the layer. Toroidal

current is not allowed to flow on the boundary, so within the boundary layer

$$J_\varphi = -\text{sign}(J_\varphi)\gamma\hat{\mathbf{n}}, \tag{5.31}$$

with $\gamma > 0$. This equation together with equation (5.28) simplify equation (5.30):

$$\frac{\partial I^{(2)}}{\partial t} = \frac{d_i}{n}\text{sign}(J_\varphi)R\gamma\mathbf{B}^{(1)}\cdot\hat{\mathbf{n}} - \frac{d_i}{n}\alpha\hat{\mathbf{n}}\cdot\hat{\mathbf{Z}}. \tag{5.32}$$

Note that on the LFS, both terms in equation (5.32) are always negative at the upper boundary and positive at the lower one. Thus $I^{(2)}$ will always be negative on the upper boundary and positive on the lower boundary. The electromagnetic torque due to two-fluid effects in the boundary layer is $\mathbf{B}\cdot\nabla I^{(2)}$, which will be positive on both the upper and lower boundaries. These positive torques lead to positive toroidal flows in the boundary layers, and angular momentum conservation requires that negative toroidal flows must develop elsewhere in the plasma. The boundary flows are quickly damped through viscous interaction with the wall, leaving a negative net toroidal angular velocity in the plasma. This is consistent with what is observed in the simulations, as can be seen in figure 5.15.

Chapter 6

Conclusions

The numerical code M3D-C^1 has been developed to calculate numerical solutions to the nonlinear dynamical equations of a comprehensive, dissipative two fluid model, in both Cartesian and curvilinear axisymmetric geometries. The numerical methods employed by this code yield significant advantages over comparable codes in cases where multiple time scales are present. M3D-C^1 has been shown to produce results in close agreement with the analytic theory of the linear normal modes of various equilibria, including dispersive waves in a homogeneous equilibrium, and unstable modes in various stratified equilibria. Furthermore, surface-averaged neoclassical transport relations and Pfirsch-Schlüter theory are found to be well satisfied in nonlinear toroidal steady-states.

The comprehensive physical model implemented in M3D-C^1 allows for the exploration of the effects of many non-ideal processes, which have usually been omitted in previous works. In chapter 4, some of these effects—the Hall and FLR effects, in particular—have been shown analytically to play an important role in the stability criteria and growth rates of several "weak" instabilities. While it has been previously noted that the inductive FLR effects are stabilizing to the MRI, it was assumed that this stabilizing effect only becomes important as ρ_i approaches the scale of the system [116, 42].

However, it has been shown here that FLR effects may be important even when $k_\perp \rho_i \ll 1$, due to the relatively slow ideal growth rate of this instability. Furthermore, unlike the collisional parallel viscosity, which only affects the growth rate of the MRI [44], the gyroviscosity alters its stability criterion, and may result in the complete stabilization of all MRI modes present in high-β accretion disks. This stabilization contradicts the result of ideal MHD—which does not remain valid when the normalized growth rate is small compared to the magnetization parameter, $(k_\perp \rho_i)^2 \gtrsim \gamma/\omega_{ci}$—that the MRI remains unstable in the limit that $B \to 0$. These results raise questions about whether the MRI could be the primary mechanism for the amplification of the extremely weak primordial "seed" magnetic fields present in the early universe to the greater interstellar field strengths observed in the present era, as others have speculated.

The fact that FLR effects may be important in slowly growing modes likely also has relevance to instabilities in tokamaks or other fusion devices. Indeed, the gravitational instability presented in chapter 4 may serve as a model for interchange instabilities (such as the ballooning mode) in toroidal configurations, with the gravitational field playing the role of the centrifugal force, with $g \sim v_{ti}^2/R_0$ [117]. This will be explored numerically after the capability for three dimensional linear stability is fully developed in M3D-C^1.

Using M3D-C^1, steady-states of the two-fluid model described in chapter 3 have been obtained for NSTX geometry plasmas by time-integration of the dynamical, driven system. Some of these states are found to be essentially stationary on all time-scales, and others are found to be oscillatory, with more-dissipative cases tending to yield more stationary steady-states. These solutions go beyond previous calculations in several ways. First, dissipative effects such as viscosity and resistivity are included, which are not present in most other numerical methods for obtaining such steady-states. These results also go beyond those obtained using other methods which do include dissi-

pative effects, because here the numerical methods allow time-integration to be carried sufficiently far to ensure a steady-state on all physical time-scales present in the problem. Second, these simulations include realistic current drive, heating, and particle injection mechanisms, and may therefore reach a realistic steady-state in the presence of dissipation. Third, the model used here includes both parallel viscosity and gyroviscosity, which have significant influence on the steady-state flows, and which have not been included in any other study of this type. Finally, two-fluid effects are also included here, which appear not to have been present in any comparable published work.

In these solutions, a number of interesting results have been found, some of which have not previously been observed or predicted. The radial flows have been found to be in excellent agreement with the Pfirsch-Schlüter theory. The steady-state poloidal and toroidal components of the flow, which are free functions in the non-dissipative case, are more difficult to obtain analytically, especially in general geometry, and therefore simulations such as the ones described in this work are particularly useful in this regard. The radial electric field, which determines the rotation, is (obviously) similarly difficult to calculate analytically, but may be easily extracted from simulation results. It is found that strong, up-down asymmetric toroidal edge flows may exist in highly resistive SOLs, in accordance with previous simulation results [12]. Parallel viscosity has been demonstrated to damp poloidal flows significantly, as previously anticipated [32]. The radial electric field has been found to be due mainly to the ion pressure gradient in the ion momentum equation, with the poloidal electric and ion diamagnetic drifts therefore nearly equal and opposite, even in the absence of parallel viscosity. In the cases presented in the previous chapter, the toroidal angular momentum balance is between isotropic viscosity, gyroviscosity, and inertia (these are essentially the only torques which can contribute to the flux-averaged torque) with the dominant balance determined by the choice of parameters. The dynamical system has been found not to attain a stationary state when the torque due to isotropic

viscosity is significantly smaller than either of the other two (non-dissipative) terms.

In particular, gyroviscosity is found to play an important role in the steady-state flows, driving toroidal and parallel flows in the presence of a density source. A theoretical basis for this core rotation, based on the gyroviscous cancellation effect, has been presented. This result suggests the possibility of driving toroidal flows localized to particular flux surfaces by pellet injection. The inclusion of gyroviscosity is found also to result in strong, regular oscillations in highly resistive steady-states, though this oscillation is not yet fully understood.

6.1 Future Work

Work is currently being done to allow three-dimensional linear stability calculations to be done using the steady-states calculated here, as discussed in section 3.5. This work may facilitate an understanding of the effect of flows, finite Larmor orbits, and other non-ideal effects on the stability of these steady-states.

One shortcoming of the preceding work regarding tokamak simulations is the relative inattention paid to modeling boundary physics. In particular, the domain boundaries are taken to be rectangular here, which does not well approximate the shape of the conducting boundaries found in most tokamaks. The meshing capabilities of M3D-C^1 and software it uses are presently being upgraded to address this issue. Furthermore, the boundary conditions used in the preceding work exclude effects which may be important in tokamaks. Such effects including finite resistivity of the conducting boundary, which lead to current diffusion through the boundary and resistive wall modes, and sheath boundary conditions which would more accurately model the loss of particles to the divertors.

More sophisticated transport models will be necessary for the simulation

of H-mode plasmas. Currently it is possible to prescribe the transport coefficients to be arbitrary functions of space, or poloidal flux, and therefore a experimentally-determined transport profiles could be used to (in theory) obtain H-mode thermodynamic profiles. This method compromises the predictive capability of the calculation, however, and therefore a more physics-based solution is preferred. As discussed in section 2.2.4, it is possible to approximate the effect of turbulent transport by using a phenomenological transport model based on the results of turbulence calculations, such as the trapped-gyro-Landau-fluid [50] (TGLF) model. By coupling such a model with the fluid model, the radial transport due to turbulence given a macroscopic thermodynamic profile may be efficiently determined and used to self-consistently calculate the evolution of that profile, without having to resolve the turbulent fluctuations due to the micro-instabilities within the fluid simulation itself. It may be challenging to employ an implicit time advance with such a coupling, due largely to the fact that the dependence of the turbulent transport coefficients on the temperature gradient (for example) may be complicated and quite sensitive near the point of marginal stability. However, this method would certainly be more efficient than extending the fluid closures to incorporate micro-instabilities into the fluid model.

It is straightforward to extend this work to more realistic parameter regimes. Results presented here have focused on more highly-resistive cases in order to obtain essentially stationary steady-states; simulations with significantly lower resistivities are possible, but appear never to settle to a stationary state, even on time-scales much longer than all diffusive time-scales in the system. The steady-state obtained in such a case would still be of interest, and analysis of the fluctuation of these states about the mean could possibly shed light on intermittent dynamical processes observed in experiments. Finally, as outlined in section 2.2.3, modifications to the electron parallel viscosity which allow the inclusion of the bootstrap current and other important banana-regime neoclassical effects, should also be explored.

Appendix A

Normalizations

Physical Quantity		Normalization	NSTX Values	
Length	$\mathbf{x}$	L_0	1	m
Density	n	n_0	2×10^{13}	cm^{-3}
Magnetic Field	$\mathbf{B}$	B_0	0.3	T
Velocity	$\mathbf{u}$	$v_{A0} = B_0/\sqrt{4\pi m_i n_0}$	1.5×10^8	cm/s
Time	t	$\tau_{A0} = L_0/v_{A0}$	0.68	μs
Pressure	p, Π	$B_0^2/4\pi$	0.7	atm
Temperature	T	$B_0^2/4\pi n_0$	22	keV
Energy	E	$B_0^2 L_0^3/4\pi$	72	kJ
Electric Field	$\mathbf{E}$	$v_{A0}B_0/c$	450	kV/m
Current Density	$\mathbf{J}$	$B_0 c/4\pi L_0$	240	$\mathrm{kA/m}^2$
Current	I	$B_0 c L_0/4\pi$	240	kA
Resistivity	η	$4\pi\tau_{A0}(v_{A0}/c)^2$	1.9	Ω m
Diffusivity	D_n	L_0^2/τ_{A0}	1.5×10^6	m^2/s
Viscosity	μ	$B_0^2\tau_{A0}/4\pi$		
Thermal Conductivity	κ	$n_0 L_0^2/\tau_{A0}$		

Appendix B

Derivation of Radial Pfirsch-Schlüter Flows

Let us make the following ordering:

$$\mathbf{J} \sim \mathbf{B} \sim \nabla p \sim 1$$
$$\eta \sim \mathbf{u} \sim d_i \sim \delta.$$

In a stationary steady-state, equations (2.8b), (2.8f) and (2.8e) are, to lowest order in δ,

$$\nabla p = \mathbf{J} \times \mathbf{B} \tag{B.1}$$
$$\nabla \times \mathbf{E} = 0 \tag{B.2}$$
$$\mathbf{E} + \mathbf{u} \times \mathbf{B} = \eta \mathbf{J} + \frac{d_i}{n} \left(\mathbf{J} \times \mathbf{B} - \nabla p_e \right). \tag{B.3}$$

Assuming that magnetic surfaces are uniquely determined by the poloidal flux, taking $\mathbf{B}\cdot$ and $\nabla\varphi\cdot$ equation (B.1) show that, to lowest order in δ, $p = p(\psi)$ and $I = I(\psi)$ respectively. Given the large parallel thermal transport, one may also assume that $T = T(\psi)$, which implies $n = n(\psi)$ and $\eta = \eta(\psi)$.

First let us calculate the steady-state currents. Taking $\mathbf{B}\times$ equation (B.1)

gives

$$\mathbf{J}_\perp = \frac{B \times \nabla\psi}{B^2} p'. \tag{B.4}$$

The condition that $\nabla \cdot \mathbf{J} = 0$ may be written, using equation (B.4), as

$$\mathbf{B} \cdot \nabla \left(\frac{Ip'}{B^2} - \frac{J_\parallel}{B} \right) = 0, \tag{B.5}$$

so one may define a new flux quantity

$$f(\psi) = \frac{Ip'}{B^2} - \frac{J_\parallel}{B}. \tag{B.6}$$

Equation (B.2) ensures that the electric field may be written as an electrostatic potential. Let

$$\mathbf{E} = -\nabla \left(\Phi + \frac{V_L}{2\pi} \varphi \right) \tag{B.7}$$

where Φ is the component of the potential not dependent on φ and V_L is the "loop voltage," which represents a uniform, axisymmetric E_φ. Taking $\mathbf{B}\cdot$ equation (B.3), and using equations (B.6) and (B.7) to eliminate $J_\parallel$ and $E_\parallel$, respectively, yields

$$\eta B^2 f(\psi) = -\mathbf{B} \cdot \nabla\Phi + \frac{V_L I}{2\pi R^2} + \eta I p'. \tag{B.8}$$

Magnetic surface averaging to eliminate Φ, and then using equation (B.6) again to eliminate f in favor of $J_\parallel$ yields

$$J_\parallel = -\frac{I}{\langle B^2 \rangle} \left[\frac{V_L}{2\pi\eta} \left\langle \frac{1}{R^2} \right\rangle + p' \left(1 - \frac{\langle B^2 \rangle}{B^2} \right) \right] \tag{B.9}$$

Taking $(\nabla\psi \times \mathbf{B})\cdot$ equation (B.3) and using equations (B.7), (B.8), (B.6),

and (B.9) to eliminate $\mathbf{E}$, Φ, f, and $J_{\|}$, respectively, yields

$$\mathbf{u} \cdot \nabla \psi = -\frac{V_L}{2\pi} \left(1 - \frac{\langle B_\varphi^2 \rangle}{\langle B^2 \rangle} \right) - \eta p' R^2 \left(1 - \frac{B_\varphi^2}{\langle B^2 \rangle} \right). \tag{B.10}$$

Appendix C

A Spectral Method for the Solution of Poisson's Equation in Cylindrical Coordinates Subject to Dirichlet Boundary Conditions

Consider the equation

$$\nabla^2\phi = -\rho, \tag{C.1}$$

where ρ is known, subject to the boundary conditions

$$\begin{aligned} \phi(Z_0) &= 0 && \text{(C.2)} \\ \phi(Z_1) &= 0 && \text{(C.3)} \\ \phi(R_0) &= 0 && \text{(C.4)} \\ \phi(R_1) &= 0 && \text{(C.5)} \end{aligned}$$

with $0 < r_0 < r_1$. The solution may be expanded in the complete Fourier-Bessel basis

$$\phi(R,Z) = \sum_{m=1}^{\infty}\sum_{n=1}^{\infty} \sin(k_Z^{(m)} Z + \theta)[A_n J_0(k_R^{(n)} R) + B_n Y_0(k_R^{(n)} R)] \qquad \text{(C.6)}$$

where the allowed spectra of k_z and k_r are determined by the boundary conditions. Equations (C.2) and (C.4) may be used to eliminate θ and one of the undetermined coefficients A_m and B_m to yield

$$\begin{aligned} \phi(R,Z) &= \sum_{m=1}^{\infty}\sum_{n=1}^{\infty} C_{mn} \sin[k_Z^{(m)}(Z - Z_0)] \qquad \text{(C.7)} \\ &\quad \times \left[Y_0(k_R^{(n)} R_0) J_0(k_R^{(n)} R) - J_0(k_R^{(n)} R_0) Y_0(k_R^{(n)} R) \right]. \end{aligned}$$

Equations (C.3) and (C.5) determine the spectra of k_z and k_r:

$$k_Z^{(m)} = \frac{m\pi}{Z_1 - Z_0} \qquad \text{(C.8)}$$

$$J_0(k_R^{(n)} R_1) Y_0(k_R^{(n)} R_0) = J_0(k_R^{(n)} R_0) Y_0(k_R^{(n)} R_1). \qquad \text{(C.9)}$$

Equation (C.9) is transcendental and the roots must be solved numerically. This may be done efficiently by noting that the asymptotic forms of $J_0(x)$ and $Y_0(x)$ when $x \gg 1$ are

$$J_0(x) \sim \sqrt{\frac{2}{\pi x}} \cos\left(x - \frac{\pi}{4}\right) \qquad \text{(C.10)}$$

$$Y_0(x) \sim \sqrt{\frac{2}{\pi x}} \sin\left(x - \frac{\pi}{4}\right). \qquad \text{(C.11)}$$

Inserting these asymptotic forms into equation equation (C.9) gives the equation

$$\sin[k_R^{(n)}(R_1 - R_0)] = 0 \qquad \text{(C.12)}$$

so k_R are approximately given by

$$k_R^{(n)} \approx \frac{n\pi}{R_1 - R_0}. \tag{C.13}$$

This may be refined quickly using Newton's method, together with the fact that

$$\begin{aligned}\frac{\partial}{\partial k}\left[J_0(kR_1)Y_0(kR_0) - J_0(kR_0)Y_0(kR_1)\right] = \\ -R_1 J_1(kR_1)Y_0(kR_0) - R_0 J_0(kR_1)Y_1(kR_0) \\ + R_0 J_1(kR_0)Y_0(kR_1) + R_1 J_0(kR_0)Y_1(kR_1).\end{aligned} \tag{C.14}$$

Finally, C_{mn} may be calculated by inserting equation (C.7) into equation (C.1), multiplying by

$$\sin[k_z^{(m')}(Z - Z_0)]\left[Y_0(k_R^{(n')}R_0)J_0(k_R^{(n')}R) - J_0(k_R^{(n')}R_0)Y_0(k_R^{(n')}R)\right], \tag{C.15}$$

and integrating over the domain to obtain

$$\begin{aligned}[(k_R^{(n)})^2 + (k_Z^{(m)})^2]C_{mn} = \\ \frac{1}{N}\int_{Z_0}^{Z_1} dZ\, \sin[k_Z^{(m)}(Z - Z_0)] \\ \times \int_{R_0}^{R_1} dR\, R\rho\left[Y_0(k_R^{(n)}R_0)J_0(k_R^{(n)}R) - J_0(k_R^{(n)}R_0)Y_0(k_R^{(n)}R)\right]\end{aligned} \tag{C.16}$$

after making use of $\int_{Z_0}^{Z_1} dZ\, \sin^2[k_Z^{(m)}(Z - Z_0)] = \frac{1}{2}$ and

$$N = \frac{1}{2}\int_{R_0}^{R_1} dR\, R\left[Y_0(k_R^{(n)}R_0)J_0(k_R^{(n)}R) - J_0(k_R^{(n)}R_0)Y_0(k_R^{(n)}R)\right]^2. \tag{C.17}$$

Appendix D

Scalar Form of Equations Implemented in M3D-C^1

In this section, the scalar forms of the physical equations, equations (2.8a)–(2.8f) are presented. The scalar forms of the time-advance equations derived in section 3.3.2.

Before proceeding, the following definitions are made to simplify notation:

$$\begin{aligned}
\Delta^* a &= R^2 \nabla \cdot \left(\frac{\nabla a}{R^2} \right) \\
\langle a, b \rangle &= \nabla a \cdot \nabla b \\
[a, b] &= \nabla \varphi \cdot \nabla a \times \nabla b \\
\langle\langle a, b \rangle\rangle &= \nabla \nabla a : \nabla \nabla b \\
[\langle a, b \rangle] &= \nabla \varphi \cdot \nabla \nabla a \dot{\times} \nabla \nabla b \\
[[a, b]] &= \nabla \varphi \cdot \nabla \nabla a \overset{\times}{\times} \nabla \nabla b \cdot \nabla \varphi.
\end{aligned}$$

For compactness, derivatives are written as subscripts in the following expressions (*i.e.* $\nu_Z = \partial_Z \nu$).

Writing the velocity and magnetic field in the flux/potential form of equa-

tions (3.37), equations (2.8a) and (2.8c) may be written:

$$\dot{n} = -[n,U] - \langle n,\chi\rangle - n\nabla^2\chi + \sigma + D_n\nabla^2 n, \tag{D.1}$$

$$\dot{p} = -[p,U] - \langle p,\chi\rangle - \Gamma p\nabla^2\chi - d_i\frac{1}{n}[I,p_e] - d_i\Gamma p_e\left[I,\frac{1}{n}\right] + (\Gamma-1)\left[d_i\mathbf{R}\cdot\frac{\mathbf{J}}{n} + d_i\Pi_e : \nabla\frac{\mathbf{J}}{n} - \nabla\cdot\mathbf{q}\right]. \tag{D.2}$$

Acting on equation (2.8b) with the operators $-\nabla\varphi\cdot\nabla\times$, $R^2\nabla\varphi\cdot$, and $\nabla\cdot$ yields:

$$\begin{aligned} &n\Delta^*\dot{U} + \left\langle n,\dot{U}\right\rangle - R^2[n,\dot{\chi}] = \\ &\quad R^2\left[\frac{\Delta^*\psi}{R^2},\psi\right] + \left(\frac{I^2}{R^2}\right)_Z - R^2\left[n\frac{\Delta^*U}{R^2},U\right] - \frac{R^2}{2}\left[\frac{\langle U,U\rangle}{R^2},n\right] \\ &\quad - \frac{(nV^2)_Z}{R^2} - \langle n\Delta^*U,\chi\rangle - n\Delta^*U\Delta^*\chi - R^2[n,[U,\chi]] \\ &\quad - \frac{1}{2}R^2[\langle\chi,\chi\rangle,n] - \sigma\Delta^*U - \langle\sigma,U\rangle + R^2[\sigma,\chi] \\ &\quad - R^2\nabla\varphi\cdot\nabla\times(n\mathbf{g} - \nabla\cdot\Pi) \end{aligned} \tag{D.3}$$

$$n\dot{V} = [I,\psi] - n[V,U] - n\langle V,\chi\rangle - \sigma V + R^2\nabla\varphi\cdot(n\mathbf{g} - \nabla\cdot\Pi) \tag{D.4}$$

$$
\begin{aligned}
n\Delta^*\dot{\chi} + \langle n, \dot{\chi}\rangle + \left[n, \dot{U}\right] = & \qquad \text{(D.5)}\\
& -\nabla^2 p - \frac{1}{R^2}\left[(\Delta^*\psi)^2 + \langle \Delta^*\psi, \psi\rangle\right] - \frac{1}{2R^2}\Delta^*\left(I^2\right)\\
& + \frac{1}{R^2}\left[n(\Delta^* U)^2 + \langle n\Delta^* U, U\rangle\right]\\
& - \frac{1}{2}\left[n\nabla^2\left(\frac{\langle U, U\rangle}{R^2}\right) + \left\langle n, \frac{\langle U, U\rangle}{R^2}\right\rangle\right]\\
& + \frac{1}{R}\left(\frac{nV^2}{R^2}\right)_R - n\nabla^2\left[\chi, U\right] - \left[n\Delta^* U, \chi\right] + \langle n, [U, \chi]\rangle\\
& - \frac{1}{2}\left(n\nabla^2\langle\chi, \chi\rangle + \langle n, \langle\chi, \chi\rangle\rangle\right) - [\sigma, U] - \sigma\nabla^2\chi - \langle\sigma, \chi\rangle\\
& + \nabla\cdot(n\mathbf{g} - \nabla\cdot\Pi)
\end{aligned}
$$

The scalar equation for the time-evolution of the magnetic flux and toroidal field may be found by operating on equations (3.1g) and (3.1e) with $R^2\nabla\varphi\cdot$, respectively:

$$
\dot{\psi} = -[\psi, U] - \langle\psi, \chi\rangle + d_i\frac{1}{n}[\psi, I] - \frac{d_i}{n}R^2\nabla\varphi\cdot(\mathbf{R} - \nabla\cdot\Pi_e) \qquad \text{(D.6)}
$$

$$
\begin{aligned}
\dot{I} = & -R^2\left[\frac{I}{R^2}, U\right] - R^2\left[\psi, \frac{V}{R^2}\right] - I\Delta^*\chi - \langle I, \chi\rangle \qquad \text{(D.7)}\\
& + R^2 d_i\left(\left[\frac{\Delta^*\psi}{R^2 n}, \psi\right] + \frac{1}{2}\left[\frac{1}{R^2 n}, I^2\right] + \left[\frac{1}{n}, p_e\right]\right)\\
& - R^2\nabla\varphi\cdot\nabla\times\left[\frac{d_i}{n}(\mathbf{R} - \nabla\cdot\Pi_e)\right],
\end{aligned}
$$

The scalar form of $\nabla\cdot\Pi$ is not expanded here, as it contains derivative of greater than second order and is therefore not useful in this form. The scalar form of this term after integration by parts is written in the following section.

D.1 Weak Form

Equations (D.1–D.7) may now be Taylor expanded and discretized in the exactly the same manner as equations (2.8a)–(2.8f) were in section 3.3.2. These scalar equations may then be integrated to yield the weak equations appropriate for computation with finite elements. The final result of this process is the set of matrix equations (3.38)–(3.41). The operators comprising the elements of the matrices in those equations are defined below.

D.1.1 Vorticity Equation

$$
\begin{aligned}
S_{UU}U^{n+1} &= U_{Un}(U^{n+1},n) \qquad \text{(D.8)}\\
&\quad -\theta\delta t\left[\begin{array}{l} U_{UUn}(U^{n+1},U,n)+U_{UUn}(U,U^{n+1},n)\\ \quad +U_{U\chi n}(U^{n+1},\chi,n)+U_{U\Pi}(U^{n+1})+U_{U\sigma}(U^{n+1})\end{array}\right]\\
&\quad -\theta^2\delta t^2\left[\begin{array}{l} U_{U\psi\psi}(U^{n+1},\psi,\psi)+U_{UII}(U^{n+1},I,I)\\ \quad +U_{Un\mathbf{g}}(U^{n+1},n)\end{array}\right]\\
S_{UV}V^{n+1} &= -\theta\delta t\left[\begin{array}{l} U_{VVn}(V^{n+1},V,n)+U_{VVn}(V,V^{n+1},n)\\ \quad +U_{V\Pi}(V^{n+1})\end{array}\right] \qquad \text{(D.9)}\\
&\quad -\theta^2\delta t^2\left[U_{V\psi I}(V^{n+1},\psi,I)\right]\\
S_{U\chi}\chi^{n+1} &= U_{\chi n}(\chi^{n+1},n) \qquad \text{(D.10)}\\
&\quad -\theta\delta t\left[\begin{array}{l} U_{\chi\chi n}(\chi^{n+1},\chi,n)+U_{\chi\chi n}(\chi,\chi^{n+1},n)\\ \quad +U_{U\chi n}(U,\chi^{n+1},n)+U_{\chi\Pi}(\chi^{n+1})+V_{\chi\sigma}(\chi^{n+1})\end{array}\right]\\
&\quad -\theta^2\delta t^2\left[\begin{array}{l} U_{\chi\psi\psi}(\chi^{n+1},\psi,\psi)+U_{\chi II}(\chi^{n+1},I,I)\\ \quad +U_{\chi n\mathbf{g}}(\chi^{n+1},n)\end{array}\right]
\end{aligned}
$$

$$
\begin{aligned}
D_{UU}U^n &= U_{Un}(U^n, n) \qquad \text{(D.11)}\\
&\quad + (1-\theta)\delta t\,[U_{U\Pi}(U^n) + U_{U\sigma}(U^n)]\\
&\quad + \left(\frac{1}{2}-\theta\right)\delta t \left[\begin{array}{l} U_{UUn}(U^n, U, n) + U_{UUn}(U, U^n, n)\\ \quad + U_{U\chi n}(U^n, \chi, n)\end{array}\right]\\
&\quad + \frac{1}{2}\delta t \left[\begin{array}{l} U_{UUn}(U^n, U^0, n) + U_{UUn}(U^0, U^n, n)\\ \quad + U_{U\chi n}(U^n, \chi^0, n)\end{array}\right]\\
&\quad - \theta^2\delta t^2 \left[\; U_{U\psi\psi}(U^n, \psi, \psi) + U_{UII}(U^n, I, I) + U_{U\mathbf{g}}(U^n) \;\right]\\
D_{UV}V^n &= (1-\theta)\delta t\,[U_{V\Pi}(V^n)] \qquad \text{(D.12)}\\
&\quad + \left(\frac{1}{2}-\theta\right)\delta t\,[U_{VVn}(V^n, V, n) + U_{VVn}(V, V^n, n)]\\
&\quad + \frac{1}{2}\delta t\,\left[U_{VVn}(V^n, V^0, n) + U_{VVn}(V^0, V^n, n)\right]\\
&\quad - \theta^2\delta t^2\,[U_{V\psi I}(V^n, \psi, I)]\\
D_{U\chi}\chi^n &= U_{\chi n}(\chi^n, n) \qquad \text{(D.13)}\\
&\quad + (1-\theta)\delta t\,[U_{\chi\Pi}(\chi^n) + U_{\chi\sigma}(\chi^n)]\\
&\quad + \left(\frac{1}{2}-\theta\right)\delta t \left[\begin{array}{l} U_{\chi\chi n}(\chi^n, \chi, n) + U_{\chi\chi n}(\chi, \chi^n, n)\\ \quad + U_{U\chi n}(U, \chi^n, n)\end{array}\right]\\
&\quad + \frac{1}{2}\delta t \left[\begin{array}{l} U_{\chi\chi n}(\chi^n, \chi^0, n) + U_{\chi\chi n}(\chi^0, \chi^n, n)\\ \quad + U_{U\chi n}(U^0, \chi^n, n)\end{array}\right]\\
&\quad - \theta^2\delta t^2 \left[\; U_{\chi\psi\psi}(\chi^n, \psi, \psi) + U_{\chi II}(\chi^n, I, I) + U_{\chi n\mathbf{g}}(\chi^n, n) \;\right]
\end{aligned}
$$

$$
\begin{aligned}
Q_{U\psi}\psi^n &= \frac{1}{2}\delta t \left[\; U_{\psi\psi}(\psi^n, \psi+\psi^0) + U_{\psi\psi}(\psi+\psi^0, \psi^n) \; \right] && \text{(D.14)}\\
&\quad - \frac{1}{2}\theta^2\delta t^2 \left[\begin{array}{l} U_{U\psi\psi}(U^0, \psi^n, \psi+\psi^0) + U_{U\psi\psi}(U^0, \psi+\psi^0, \psi^n) \\ U_{\chi\psi\psi}(\chi^0, \psi^n, \psi+\psi^0) + U_{\chi\psi\psi}(\chi^0, \psi+\psi^0, \psi^n) \\ \; + U_{V\psi I}(V^0, \psi^n, I+I^0) \end{array} \right]\\
Q_{UI}I^n &= \frac{1}{2}\delta t \left[\; U_{II}(I^n, I+I^0) + U_{II}(I+I^0, I^n) \; \right] && \text{(D.15)}\\
&\quad - \frac{1}{2}\theta^2\delta t^2 \left[\begin{array}{l} U_{UII}(U^0, I^n, I+I^0) + U_{UII}(U^0, I+I^0, I^n) \\ U_{\chi II}(\chi^0, I^n, I+I^0) + U_{\chi II}(\chi^0, I+I^0, I^n) \\ \; + U_{V\psi I}(V^0, \psi+\psi^0, I^n) \end{array} \right]\\
Q_{Up}p^n &= 0 && \text{(D.16)}\\
Q_{Un}n^n &= \delta t \left[\begin{array}{l} U_{UUn}(U^0, U^0, n^n) + U_{VVn}(V^0, V^0, n^n) \\ \; + U_{\chi\chi n}(\chi^0, \chi^0, n^n) + U_{U\chi n}(U^0, \chi^0, n^n) + U_{n\mathbf{g}}(n^n) \end{array} \right] && \text{(D.17)}\\
&\quad + \delta t^2 \left[U_{Un\mathbf{g}}(U^0, n^n) + U_{\chi n\mathbf{g}}(\chi^0, n^n) \right]
\end{aligned}
$$

D.1.2 Toroidal Velocity Equation

$$
\begin{aligned}
S_{VU}U^{n+1} &= -\theta\delta t \left[V_{UVn}(U^{n+1}, V, n) + V_{U\Pi}(U^{n+1}) \right] && \text{(D.18)}\\
&\quad - \theta^2\delta t^2 \left[V_{U\psi I}(U^{n+1}, \psi, I) \right]\\
S_{VV}V^{n+1} &= V_{Vn}(V^{n+1}, n) && \text{(D.19)}\\
&\quad - \theta\delta t \left[\begin{array}{l} V_{UVn}(U, V^{n+1}, n) + V_{V\chi n}(V^{n+1}, \chi, n) \\ \; + V_{V\Pi}(V^{n+1}) + V_{V\sigma}(V^{n+1}) \end{array} \right]\\
&\quad - \theta^2\delta t^2 \left[V_{V\psi\psi}(V^{n+1}, \psi, \psi) \right]\\
S_{V\chi}\chi^{n+1} &= -\theta\delta t \left[V_{V\chi n}(V, \chi^{n+1}, n) + V_{\chi\Pi}(\chi^{n+1}) \right] && \text{(D.20)}\\
&\quad - \theta^2\delta t^2 \left[V_{\chi\psi I}(\chi^{n+1}, \psi, I) \right]
\end{aligned}
$$

$$
\begin{aligned}
D_{VU}U^n &= (1-\theta)\delta t\left[V_{U\Pi}(U^n)\right] \qquad \text{(D.21)}\\
&\quad + \left(\frac{1}{2}-\theta\right)\delta t\left[V_{UVn}(U^n,V,n)\right] + \frac{1}{2}\delta t\left[V_{UVn}(U^n,V^0,n)\right]\\
&\quad - \theta^2\delta t^2\left[V_{U\psi I}(U^n,\psi,I)\right]\\
D_{VV}V^n &= V_{Vn}(V^n,n)(1-\theta)\delta t\left[V_{V\Pi}(V^n)+V_{V\sigma}(V^n)\right] \qquad \text{(D.22)}\\
&\quad \left(\frac{1}{2}-\theta\right)\delta t\left[V_{UVn}(U,V^n,n)+V_{V\chi n}(V^n,\chi,n)\right]\\
&\quad + \frac{1}{2}\delta t\left[V_{UVn}(U^0,V^n,n)+V_{V\chi n}(V^n,\chi^0,n)\right]\\
&\quad - \theta^2\delta t^2\left[V_{V\psi\psi}(V^n,\psi,\psi)\right]\\
D_{V\chi}\chi^n &= (1-\theta)\delta t\left[V_{\chi\Pi}(\chi^n)\right] \qquad \text{(D.23)}\\
&\quad + \left(\frac{1}{2}-\theta\right)\delta t\left[V_{V\chi n}(V,\chi^n,n)\right] + \frac{1}{2}\delta t\left[V_{V\chi n}(V^0,\chi^n,n)\right]\\
&\quad - \theta^2\delta t^2\left[V_{\chi\psi I}(\chi^n,\psi,I)\right]
\end{aligned}
$$

$$
\begin{aligned}
Q_{V\psi}\psi^n &= \frac{1}{2}\delta t\left[V_{\psi I}(\psi^n,I+I^0)\right] \qquad \text{(D.24)}\\
&\quad + \frac{1}{2}\theta\delta t^2\left[\begin{array}{l} V_{V\psi\psi}(V^0,\psi+\psi^0,\psi^n)+V_{V\psi\psi}(V^0,\psi^n,\psi+\psi^0)\\ +U_{U\psi I}(U^0,\psi^n,I+I^0)+U_{\chi\psi I}(\chi^0,\psi^n,I+I^0)\end{array}\right]\\
Q_{VI}I^n &= \frac{1}{2}\delta t\left[V_{\psi I}(\psi+\psi^0,I^n)\right] \qquad \text{(D.25)}\\
&\quad + \frac{1}{2}\theta\delta t^2\left[\ U_{U\psi I}(U^0,\psi+\psi^0,I^n)+U_{\chi\psi I}(\chi^0,\psi+\psi^0,I^n)\ \right]\\
Q_{Vp}p^n &= 0 \qquad \text{(D.26)}\\
Q_{Vn}n^n &= \delta t\left[V_{UVn}(U^0,V^0,n^n)+V_{V\chi n}(V^0,\chi^0,n^n)\right] \qquad \text{(D.27)}
\end{aligned}
$$

D.1.3 Compressional Velocity Equation

$$
\begin{aligned}
S_{\chi U}U^{n+1} &= X_{Un}(U^{n+1},n) \qquad \text{(D.28)}\\
&\quad -\theta\delta t\left[\begin{array}{l} X_{UUn}(U^{n+1},U,n)+X_{UUn}(U,U^{n+1},n)\\ +X_{U\chi n}(U^{n+1},\chi,n)+X_{U\Pi}(U^{n+1})+X_{U\sigma}(U^{n+1})\end{array}\right]\\
&\quad -\theta^2\delta t^2\left[\begin{array}{l} X_{U\psi\psi}(U^{n+1},\psi,\psi)+X_{UII}(U^{n+1},I,I)\\ +X_{Up}(U^{n+1},p)+X_{Un\mathbf{g}}(U^{n+1},n)\end{array}\right]\\
S_{\chi V}V^{n+1} &= -\theta\delta t\left[\begin{array}{l} X_{VVn}(V^{n+1},V,n)+X_{VVn}(V,V^{n+1},n)\\ +X_{V\Pi}(V^{n+1})\end{array}\right] \qquad \text{(D.29)}\\
&\quad -\theta^2\delta t^2\left[X_{V\psi I}(V^{n+1},\psi,I)\right]\\
S_{U\chi}\chi^{n+1} &= X_{\chi n}(\chi^{n+1},n) \qquad \text{(D.30)}\\
&\quad -\theta\delta t\left[\begin{array}{l} X_{\chi\chi n}(\chi^{n+1},\chi,n)+X_{\chi\chi n}(\chi,\chi^{n+1},n)\\ +X_{U\chi n}(U,\chi^{n+1},n)+X_{\chi\Pi}(\chi^{n+1})+X_{\chi\sigma}(\chi^{n+1})\end{array}\right]\\
&\quad -\theta^2\delta t^2\left[\begin{array}{l} X_{\chi\psi\psi}(\chi^{n+1},\psi,\psi)+X_{\chi II}(\chi^{n+1},I,I)\\ +X_{\chi p}(\chi^{n+1},p)+X_{\chi\mathbf{g}}(\chi^{n+1})\end{array}\right]
\end{aligned}
$$

$$
\begin{aligned}
D_{\chi U}U^n &= X_{Un}(U^n,n) \qquad\qquad (D.31)\\
&\quad + (1-\theta)\delta t\left[X_{U\Pi}(U^n)+X_{U\sigma}(U^n)\right]\\
&\quad + \left(\frac{1}{2}-\theta\right)\delta t\left[\begin{array}{l} X_{UUn}(U^n,U,n)+X_{UUn}(U,U^n,n)\\ \quad +X_{U\chi n}(U^n,\chi,n)\end{array}\right]\\
&\quad + \frac{1}{2}\delta t\left[\begin{array}{l} X_{UUn}(U^n,U^0,n)+X_{UUn}(U^0,U^n,n)\\ \quad +X_{U\chi n}(U^n,\chi^0,n)\end{array}\right]\\
&\quad - \theta^2\delta t^2\left[\begin{array}{l} X_{U\psi\psi}(U^n,\psi,\psi)+X_{UII}(U^n,I,I)\\ \quad +X_{Up}(U^np)+X_{Un\mathbf{g}}(U^n,n)\end{array}\right]\\
D_{\chi V}V^n &= (1-\theta)\delta t\left[X_{V\Pi}(V^{n+1})\right] \qquad\qquad (D.32)\\
&\quad \left(\frac{1}{2}-\theta\right)\delta t\left[X_{VVn}(V^n,V,n)+X_{VVn}(V,V^n,n)\right]\\
&\quad + \frac{1}{2}\delta t\left[X_{VVn}(V^n,V^0,n)+X_{VVn}(V^0,V^n,n)\right]\\
&\quad - \theta^2\delta t^2\left[X_{V\psi I}(V^n,\psi,I)\right]\\
D_{\chi\chi}\chi^n &= X_{\chi n}(\chi^n,n) \qquad\qquad (D.33)\\
&\quad + (1-\theta)\delta t\left[X_{\chi\Pi}(\chi^n)+X_{\chi\sigma}(\chi^n)\right]\\
&\quad + \left(\frac{1}{2}-\theta\right)\delta t\left[\begin{array}{l} X_{\chi\chi n}(\chi^n,\chi,n)+X_{\chi\chi n}(\chi,\chi^n,n)\\ \quad +X_{U\chi n}(U,\chi^n,n)\end{array}\right]\\
&\quad + \frac{1}{2}\delta t\left[\begin{array}{l} X_{\chi\chi n}(\chi^n,\chi^0,n)+X_{\chi\chi n}(\chi^0,\chi^n,n)\\ \quad +X_{U\chi n}(U^0,\chi^n,n)\end{array}\right]\\
&\quad - \theta^2\delta t^2\left[\begin{array}{l} X_{\chi\psi\psi}(\chi^n,\psi,\psi)+X_{\chi II}(\chi^n,I,I)\\ \quad +X_{\chi p}(\chi,p)+X_{\chi n\mathbf{g}}(\chi^n n)\end{array}\right]
\end{aligned}
$$

$$
\begin{aligned}
Q_{\chi\psi}\psi^n &= \frac{1}{2}\delta t\left[\ X_{\psi\psi}(\psi^n,\psi+\psi^0)+X_{\psi\psi}(\psi+\psi^0,\psi^n)\ \right] \qquad \text{(D.34)}\\
&\quad -\frac{1}{2}\theta^2\delta t^2\left[\begin{array}{l} X_{U\psi\psi}(U^0,\psi^n,\psi+\psi^0)+X_{U\psi\psi}(U^0,\psi+\psi^0,\psi^n)\\ +X_{\chi\psi\psi}(\chi^0,\psi^n,\psi+\psi^0)+X_{\chi\psi\psi}(\chi^0,\psi+\psi^0,\psi^n)\\ +X_{V\psi I}(V^0,\psi^n,I+I^0)\end{array}\right]\\
Q_{\chi I}I^n &= \frac{1}{2}\delta t\left[\ X_{II}(I^n,I+I^0)+X_{II}(I+I^0,I^n)\ \right] \qquad \text{(D.35)}\\
&\quad -\frac{1}{2}\theta^2\delta t^2\left[\begin{array}{l} X_{UII}(U^0,I^n,I+I^0)+X_{UII}(U^0,I+I^0,I^n)\\ X_{\chi II}(\chi^0,I^n,I+I^0)+X_{\chi II}(\chi^0,I+I^0,I^n)\\ +X_{V\psi I}(V^0,\psi+\psi^0,I^n)\end{array}\right]\\
Q_{\chi p}p^n &= \delta t\left[X_p(p^n)\right]+\theta\delta t^2\left[X_{Up}(U^0,p^n)+X_{\chi p}(\chi^0,p^n)\right] \qquad \text{(D.36)}\\
Q_{\chi n}n^n &= \delta t\left[\begin{array}{l} X_{UUn}(U^0,U^0,n^n)+X_{VVn}(V^0,V^0,n^n)\\ +X_{\chi\chi n}(\chi^0,\chi^0,n^n)+X_{U\chi n}(U^0,\chi^0,n^n)+X_{n\mathbf{g}}(n^n)\end{array}\right] \qquad \text{(D.37)}\\
&\quad +\delta t^2\left[X_{Un\mathbf{g}}(U^0,n^n)+X_{\chi n\mathbf{g}}(\chi^0,n^n)\right]
\end{aligned}
$$

D.1.4 Density Equation

$$
\begin{aligned}
S_{nn}n^{n+1} &= N_n(n^{n+1}) \qquad \text{(D.38)}\\
&\quad -\theta\delta t\left[N_{nU}(n^{n+1},U)+N_{n\chi}(n^{n+1},\chi)+N_{nD_n}(n^{n+1})\right]
\end{aligned}
$$

$$
\begin{aligned}
D_{nn}n^n &= N_n(n^n) \qquad \text{(D.39)}\\
&\quad +(1-\theta)\delta t\left[N_{nU}(n^n,U)+N_{n\chi}(n^n,\chi)+N_{nD_n}(n^n)\right]
\end{aligned}
$$

$$
\begin{aligned}
R_{nU}U^{n+1} &= \theta\delta t\left[N_{nU}(n,U^{n+1})\right] \qquad \text{(D.40)}\\
R_{nV}V^{n+1} &= 0 \qquad \text{(D.41)}\\
R_{n\chi}\chi^{n+1} &= \theta\delta t\left[N_{n\chi}(n,\chi^{n+1})\right] \qquad \text{(D.42)}
\end{aligned}
$$

$$Q_{nU}U^n = -\theta\delta t\left[N_{nU}(n,U^n)\right] + \delta t\left[N_{nU}(n^0,U^n)\right] \quad \text{(D.43)}$$

$$Q_{nV}V^n = 0 \quad \text{(D.44)}$$

$$Q_{n\chi}\chi^n = -\theta\delta t\left[N_{n\chi}(n,\chi^n)\right] + \delta t\left[N_{n\chi}(n^0,\chi^n)\right] \quad \text{(D.45)}$$

D.1.5 Pressure Equation

$$\begin{aligned} S_{pp}p^{n+1} &= P_p(p^{n+1}) \quad \text{(D.46)}\\ &\quad -\theta\delta t\left[\begin{array}{l} P_{pU}(p^{n+1},U)+P_{p\chi}(p^{n+1},\chi)\\ +P_{p\kappa}(p^{n+1})+P_{pI\kappa}(p^{n+1},I)+P_{p\psi\psi\kappa}(p^{n+1},\psi,\psi)\end{array}\right] \end{aligned}$$

$$\begin{aligned} D_{pp}p^{n} &= P_p(p^{n}) \quad \text{(D.47)}\\ &\quad +(1-\theta)\delta t\left[\begin{array}{l} P_{pU}(p^{n},U)+P_{p\chi}(p^{n},\chi)\\ +P_{p\kappa}(p^{n})+P_{pI\kappa}(p^{n},I)+P_{p\psi\psi\kappa}(p^{n},\psi,\psi)\end{array}\right] \end{aligned}$$

$$R_{pU}U^{n+1} = \theta\delta t\left[\begin{array}{l} P_{pU}(p,U^{n+1})+P_{U\chi\sigma}(U^{n+1},\chi)\\ +P_{UU\sigma}(U^{n+1},U)+P_{UU\sigma}(U,U^{n+1})\end{array}\right] \quad \text{(D.48)}$$

$$R_{pV}V^{n+1} = \theta\delta t\left[P_{VV\sigma}(V^{n+1},V)+P_{VV\sigma}(V,V^{n+1})\right] \quad \text{(D.49)}$$

$$R_{p\chi}\chi^{n+1} = \theta\delta t\left[\begin{array}{l} P_{p\chi}(p,\chi^{n+1})+P_{U\chi\sigma}(U^{n+1},\chi,\sigma)\\ +P_{\chi\chi\sigma}(\chi^{n+1},\chi)+P_{\chi\chi\sigma}(\chi,\chi^{n+1})\end{array}\right] \quad \text{(D.50)}$$

$$
\begin{aligned}
Q_{pU}U^n &= (1-\theta)\delta t\left[P_{pU}(p,U^n)\right] + \delta t\left[P_{pU}(p^0,U^n)\right] \qquad \text{(D.51)}\\
&\quad + \left(\frac{1}{2}-\theta\right)\delta t\left[\begin{array}{l} P_{U\chi\sigma}(U^n,\chi) \\ \quad + P_{UU\sigma}(U^n,U) + P_{UU\sigma}(U,U^n) \end{array}\right] \\
&\quad \frac{1}{2}\delta t\left[\begin{array}{l} P_{U\chi\sigma}(U^n,\chi^0) \\ \quad + P_{UU\sigma}(U^n,U^0) + P_{UU\sigma}(U^0,U^n) \end{array}\right] \\
Q_{pV}V^n &= \left(\frac{1}{2}-\theta\right)\delta t\left[P_{VV\sigma}(V^n,V) + P_{VV\sigma}(V,V^n)\right] \qquad \text{(D.52)}\\
&\quad + \frac{1}{2}\delta t\left[P_{VV\sigma}(V^n,V^0) + P_{VV\sigma}(V^0,V^n)\right] \\
Q_{p\chi}\chi^n &= (1-\theta)\delta t\left[P_{p\chi}(p,\chi^n)\right] + \delta t\left[P_{p\chi}(p^0,\chi^n)\right] \qquad \text{(D.53)}\\
&\quad + \left(\frac{1}{2}-\theta\right)\delta t\left[\begin{array}{l} P_{U\chi\sigma}(U,\chi^n) \\ \quad + P_{\chi\chi\sigma}(\chi^n,\chi) + P_{\chi\chi\sigma}(\chi,\chi^n) \end{array}\right] \\
&\quad \frac{1}{2}\delta t\left[\begin{array}{l} P_{U\chi\sigma}(U^0,\chi^n) \\ \quad + P_{\chi\chi\sigma}(\chi^n,\chi^0) + P_{\chi\chi\sigma}(\chi^0,\chi^n) \end{array}\right]
\end{aligned}
$$

$$
O_p = \delta t\left[\begin{array}{l} P_{p_eI}(p_e,I) + P_{\psi\psi\eta}(\psi,\psi) + P_{II\eta}(I,I) \end{array}\right] \qquad \text{(D.54)}
$$

D.1.6 Electron Pressure Equation

$$
\begin{aligned}
S_{p_e\psi}\psi^{n+1} &= -\theta\delta t\left[\begin{array}{l} P_{\psi\psi\eta}(\psi^{n+1},\psi) + P_{\psi\psi\eta}(\psi,\psi^{n+1}) \\ \quad + P_{p\psi\psi\kappa}(p_e,\psi^{n+1},\psi) + P_{p\psi\psi\kappa}(p_e,\psi,\psi^{n+1}) \end{array}\right] \qquad \text{(D.55)}\\
S_{p_eI}I^{n+1} &= -\theta\delta t\left[\begin{array}{l} P_{II\eta}(I^{n+1},I) + P_{II\eta}(I,I^{n+1}) \\ \quad + P_{p_eI}(p_e,I^{n+1}) + P_{pI\kappa}(p_e,I^{n+1}) \end{array}\right] \qquad \text{(D.56)}\\
S_{p_ep_e}p_e^{n+1} &= P_p(p_e^{n+1}) \qquad \text{(D.57)}\\
&\quad - \theta\delta t\left[\begin{array}{l} P_{pU}(p_e^{n+1},U) + P_{p\chi}(p_e^{n+1},\chi) + P_{p_eI}(p_e^{n+1},I) \\ \quad + P_{p\kappa}(p_e^{n+1}) + P_{pI\kappa}(p_e^{n+1},I) + P_{p\psi\psi\kappa}(p_e^{n+1},\psi,\psi) \end{array}\right]
\end{aligned}
$$

$$
\begin{aligned}
D_{p_e\psi}\psi^n &= \left(\frac{1}{2}-\theta\right)\delta t\left[\begin{array}{l} P_{\psi\psi\eta}(\psi^n,\psi)+P_{\psi\psi\eta}(\psi,\psi^n) \\ +P_{p\psi\psi\kappa}(p_e,\psi^n,\psi)+P_{p\psi\psi\kappa}(p_e,\psi,\psi^n)\end{array}\right] \qquad \text{(D.58)}\\
&\quad +\frac{1}{2}\delta t\left[\begin{array}{l} P_{\psi\psi\eta}(\psi^n,\psi^0)+P_{\psi\psi\eta}(\psi^0,\psi^n) \\ +P_{p\psi\psi\kappa}(p_e,\psi^n,\psi^0)+P_{p\psi\psi\kappa}(p_e,\psi^0,\psi^n)\end{array}\right]\\
D_{p_eI}I^n &= -\theta\delta t\left[P_{p_eI}(p_e,I^n)+P_{pI\kappa}(p_e,I^n)\right] \qquad \text{(D.59)}\\
&\quad +\delta t\left[P_{p_eI}(p_e^0,I^n)+P_{pI\kappa}(p_e^0,I^n)\right]\\
&\quad +\left(\frac{1}{2}-\theta\right)\delta t\left[P_{II\eta}(I^n,I)+P_{II\eta}(I,I^n)\right]\\
&\quad +\frac{1}{2}\delta t\left[P_{II\eta}(I^n,I^0)+P_{II\eta}(I^0,I^n)\right]\\
D_{p_ep_e}p_e^n &= P_p(p_e^n) \qquad \text{(D.60)}\\
&\quad +(1-\theta)\delta t\left[\begin{array}{l} P_{pU}(p_e^n,U)+P_{p\chi}(p_e^n,\chi)+P_{p_eI}(p_e^n,I) \\ +P_{p\kappa}(p_e^n)+P_{pI\kappa}(p_e^n,I)+P_{p\psi\psi\kappa}(p_e^n,\psi,\psi)\end{array}\right]
\end{aligned}
$$

$$
\begin{aligned}
R_{p_eU}U^{n+1} &= \theta\delta t\left[P_{pU}(p_e,U^{n+1})\right] \qquad \text{(D.61)}\\
R_{p_eV}V^{n+1} &= 0 \qquad \text{(D.62)}\\
R_{p_e\chi}\chi^{n+1} &= \theta\delta t\left[P_{p\chi}(p_e,\chi^{n+1})\right] \qquad \text{(D.63)}
\end{aligned}
$$

$$
\begin{aligned}
Q_{p_eU}U^n &= (1-\theta)\delta t\left[P_{pU}(p_e,U^n)\right]+\delta t\left[P_{pU}(p_e^0,U^n)\right] \qquad \text{(D.64)}\\
Q_{p_eV}V^n &= 0 \qquad \text{(D.65)}\\
Q_{p_e\chi}\chi^n &= (1-\theta)\delta t\left[P_{p\chi}(p_e,\chi^n)\right]+\delta t\left[P_{p\chi}(p_e^0,\chi^n)\right] \qquad \text{(D.66)}
\end{aligned}
$$

$$
O_{p_e} = 0 \qquad \text{(D.67)}
$$

D.1.7 Magnetic Flux Equation

$$
\begin{aligned}
S_{\psi\psi}\psi^{n+1} &= \Psi_{\psi}(\psi^{n+1}) \\
&\quad - \theta\delta t \left[\begin{array}{l} \Psi_{\psi U}(\psi^{n+1}, U) + \Psi_{\psi\chi}(\psi^{n+1}, \chi) \\ + \Psi_{\psi I}(\psi^{n+1}, I) + \Psi_{\psi\eta}(\psi^{n+1}) + \end{array} \right]
\end{aligned} \tag{D.68}
$$

$$
S_{\psi I} I^{n+1} = -\theta\delta t \left[\Psi_{\psi I}(\psi, I^{n+1})\right] \tag{D.69}
$$

$$
S_{\psi p_e} p_e^{n+1} = 0 \tag{D.70}
$$

$$
\begin{aligned}
D_{\psi\psi}\psi^{n} &= \Psi_{\psi}(\psi^{n}) \\
&\quad (1-\theta)\delta t \left[\begin{array}{l} \Psi_{\psi U}(\psi^{n}, U) + \Psi_{\psi\chi}(\psi^{n}, \chi) \\ + \Psi_{\psi\eta}(\psi^{n}) + \end{array} \right] \\
&\quad + (\frac{1}{2} - \theta)\delta t \left[\Psi_{\psi I}(\psi^{n}, I)\right] + \frac{1}{2}\delta t \left[\Psi_{\psi I}(\psi^{n}, I^{0})\right]
\end{aligned} \tag{D.71}
$$

$$
D_{\psi I} I^{n} = (\frac{1}{2} - \theta)\delta t \left[\Psi_{\psi I}(\psi, I^{n})\right] + \frac{1}{2}\delta t \left[\Psi_{\psi I}(\psi^{0}, I^{n})\right] \tag{D.72}
$$

$$
D_{\psi p_e} p_e^{n} = 0 \tag{D.73}
$$

$$
R_{\psi U} U^{n+1} = \theta\delta t \left[\Psi_{\psi U}(\psi, U^{n+1})\right] \tag{D.74}
$$

$$
R_{\psi V} V^{n+1} = 0 \tag{D.75}
$$

$$
R_{\psi\chi} \chi^{n+1} = \theta\delta t \left[\Psi_{\psi\chi}(\psi, \chi^{n+1})\right] \tag{D.76}
$$

$$
Q_{\psi U} U^{n} = -\theta\delta t \left[\Psi_{\psi U}(\psi, U^{n})\right] + \delta t \left[\Psi_{\psi U}(\psi^{0}, U^{n})\right] \tag{D.77}
$$

$$
Q_{\psi V} V^{n} = 0 \tag{D.78}
$$

$$
Q_{\psi\chi} \chi^{n} = -\theta\delta t \left[\Psi_{\psi\chi}(\psi, \chi^{n})\right] + \delta t \left[\Psi_{\psi\chi}(\psi^{0}, \chi^{n})\right] \tag{D.79}
$$

D.1.8 Toroidal Magnetic Field Equation

$$
\begin{aligned}
S_{I\psi}\psi^{n+1} &= -\theta\delta t \left[\begin{array}{l} I_{\psi\psi}(\psi^{n+1},\psi) + I_{\psi\psi}(\psi,\psi^{n+1}) \\ + I_{\psi V}(\psi^{n+1},V) \end{array} \right] && \text{(D.80)} \\
S_{II}I^{n+1} &= I_I(I^{n+1}) && \text{(D.81)} \\
&\quad - \theta\delta t \left[\begin{array}{l} I_{IU}(I^{n+1},U) + I_{I\chi}(I^{n+1},\chi) + I_{I\eta}(I^{n+1}) \\ + I_{II}(I^{n+1},I) + I_{II}(I,I^{n+1}) \end{array} \right] \\
S_{Ip_e}p_e^{n+1} &= -\theta\delta t \left[I_{p_e}(p_e^{n+1}) \right] && \text{(D.82)}
\end{aligned}
$$

$$
\begin{aligned}
D_{I\psi}\psi^{n} &= (1-\theta)\delta t \left[I_{\psi V}(\psi^n, V) \right] && \text{(D.83)} \\
&\quad + \left(\frac{1}{2} - \theta \right) \delta t \left[I_{\psi\psi}(\psi^n,\psi) + I_{\psi\psi}(\psi,\psi^n) \right] \\
&\quad + \frac{1}{2}\delta t \left[I_{\psi\psi}(\psi^n,\psi^0) + I_{\psi\psi}(\psi^0,\psi^n) \right] \\
D_{II}I^{n} &= I_I(I^n) + (1-\theta)\delta t \left[\begin{array}{l} I_{IU}(I^{n+1},U) + I_{I\chi}(I^n,\chi) \\ + I_{I\eta}(I^n) \end{array} \right] && \text{(D.84)} \\
&\quad + \left(\frac{1}{2} - \theta \right) \delta t \left[I_{II}(I^n,I) + I_{II}(I,I^n) \right] \\
&\quad + \frac{1}{2}\delta t \left[I_{II}(I^n,I^0) + I_{II}(I^0,I^n) \right] \\
D_{Ip_e}p_e^{n} &= (1-\theta)\delta t \left[I_{p_e}(p_e^n) \right] && \text{(D.85)}
\end{aligned}
$$

$$
\begin{aligned}
R_{IU}U^{n+1} &= \theta\delta t \left[I_{IU}(I,U^{n+1}) \right] && \text{(D.86)} \\
R_{IV}V^{n+1} &= \theta\delta t \left[I_{\psi V}(\psi,V^{n+1}) \right] && \text{(D.87)} \\
R_{I\chi}\chi^{n+1} &= \theta\delta t \left[I_{I\chi}(I,\chi^{n+1}) \right] && \text{(D.88)}
\end{aligned}
$$

$$Q_{IU}U^n = -\theta\delta t\left[I_{IU}(I,U^n)\right] + \delta t\left[I_{IU}(I^0,U^n)\right] \quad \text{(D.89)}$$

$$Q_{IV}V^n = -\theta\delta t\left[I_{\psi V}(\psi,V^n)\right] + \delta t\left[I_{\psi U}(\psi^0,V^n)\right] \quad \text{(D.90)}$$

$$Q_{I\chi}\chi^n = -\theta\delta t\left[I_{I\chi}(I,\chi^n)\right] + \delta t\left[I_{I\chi}(I^0,\chi^n)\right] \quad \text{(D.91)}$$

D.2 Matrix Element Component Terms

The terms in the above equations are categorized and defined in the following sections. Each term has been integrated by parts to arrive at the simplest expression for which the order of differentiation on the trial function is roughly equal to that on the physical fields. The integrations by parts of tensor quantities are aided by use of the following identities, which hold for any symmetric tensor Π:

$$R^2\nu\nabla\varphi\cdot\nabla\times(\nabla\cdot\Pi) = R^2\nu_Z\nabla\varphi\cdot\Pi\cdot\nabla\varphi - \nabla\nu\cdot\Pi\cdot\nabla Z + R\nabla\varphi\cdot\left[\nabla\nabla(\nu R)\dot{\times}\Pi\right] + \nabla\cdot\mathbf{A}_1 \quad \text{(D.92)}$$

$$-R^2\nu\nabla\varphi\cdot(\nabla\cdot\Pi) = R^2\nabla\nu\cdot\Pi\cdot\nabla\varphi + \nabla\cdot\mathbf{A}_2 \quad \text{(D.93)}$$

$$-\nu\nabla\cdot(\nabla\cdot\Pi) = -\nabla\nabla\nu:\Pi + \nabla\cdot\mathbf{A}_3 \quad \text{(D.94)}$$

where

$$\mathbf{A}_1 = -R^2\nu\nabla\varphi\times(\nabla\cdot\Pi) - R\Pi\cdot[\nabla\varphi\times\nabla(R\nu)] + \nu\Pi\cdot\nabla z$$

$$\mathbf{A}_2 = -R^2\nu\Pi\cdot\nabla\varphi$$

$$\mathbf{A}_3 = \nabla\nu\cdot\Pi - \nu\nabla\cdot\Pi.$$

In order to simplify the notation of the following terms, $A \equiv B$ is defined to mean $A = \int dA\ B$.

D.2.1 Magnetohydrodynamic Terms

The terms in this section are the basic magnetohydrodynamic terms in the two-fluid equations, which do not depend on any specific choice of closure. These terms include convection, internal forces (pressure, Lorentz force), and electromagnetic induction.

$$\begin{aligned}
N_n(n) &\equiv \nu n \\
N_{nU}(n,U) &\equiv \nu\,[U,n] \\
N_{n\chi}(n,\chi) &\equiv n\,\langle \nu,\chi\rangle \quad -\nabla\cdot(\nu n\nabla\chi) \\
N_{nD_n}(n,D_n) &\equiv D_n\nu\nabla^2 n
\end{aligned} \tag{D.95}$$

$$\begin{aligned}
U_{Un}(U,n) &\equiv -\tfrac{1}{R^2}n\,\langle R^2\nu,U\rangle \\
&\quad +\nabla\cdot(\nu n\nabla U) \\
U_{\chi n}(\chi,n) &\equiv -R^2\nu\,[n,\chi] \\
U_{UUn}(U,U,n) &\equiv \tfrac{1}{R^2}n\Delta^*U\,[R^2\nu,U]+\tfrac{1}{2R^2}\,\langle U,U\rangle\,[R^2\nu,n] \\
&\quad -[\nu n\Delta^*U,U]-\left[\tfrac{1}{2}\nu\,\langle U,U\rangle\,,n\right] \\
U_{VVn}(V,V,n) &\equiv \tfrac{1}{2R^2}\,[\nu,R^2]\,VVn \\
&\quad -\left[\tfrac{1}{R}\nu nVV,R\right] \\
U_{U\chi n}(U,\chi,n) &\equiv \tfrac{1}{R^2}n\Delta^*U\,\langle R^2\nu,\chi\rangle-[U,\chi]\,[R^2\nu,n] \\
&\quad -\nabla\cdot(\nu n\Delta^*U\nabla\chi)-[R^2\nu\,[\chi,U]\,,n] \\
U_{\chi\chi n}(\chi,\chi,n) &\equiv \tfrac{1}{2}\,\langle\chi,\chi\rangle\,[R^2\nu,n] \\
&\quad -\left[\tfrac{1}{2}R^2\nu\,\langle\chi,\chi\rangle\,,n\right] \\
U_{\psi\psi}(\psi,\psi) &\equiv -\tfrac{1}{R^2}\,[R^2\nu,\psi]\,\Delta^*\psi \\
&\quad -[\psi,\nu\Delta^*\psi] \\
U_{II}(I,I) &\equiv -R^2\nu I\left[I,\tfrac{1}{R^2}\right]
\end{aligned} \tag{D.96}$$

$$\begin{aligned}
V_{Vn}(V,n) &\equiv \nu nV \\
V_{UVn}(U,V,n) &\equiv \nu n\,[U,V] \\
V_{V\chi n}(V,\chi,n) &\equiv -\nu n\,\langle\chi,V\rangle \\
V_{\psi I}(\psi,I) &\equiv \nu\,[I,\psi]
\end{aligned} \tag{D.97}$$

$$
\begin{aligned}
X_{Un}(U,n) &\equiv \nu\,[n,U] \\
X_{\chi n}(\chi,n) &\equiv -n\,\langle\nu,\chi\rangle \\
&\quad + \nabla\cdot(\nu n\nabla\chi) \\
X_{p}(p) &\equiv -\nu\nabla^2 p \\
X_{UUn}(U,U,n) &\equiv -\tfrac{1}{R^2}n\Delta^* U\,\langle\nu,U\rangle + \tfrac{1}{2}n\left\langle\nu,\tfrac{\langle U,U\rangle}{R^2}\right\rangle \\
&\quad + \nabla\cdot(\tfrac{1}{R^2}\nu n\Delta^* U\nabla U) - \nabla\cdot\left[\tfrac{1}{2}\nu n\nabla\left(\tfrac{1}{R^2}\langle U,U\rangle\right)\right] \\
X_{VVn}(V,V,n) &\equiv \tfrac{1}{2}nVV\left\langle\tfrac{1}{R^2},\nu\right\rangle \\
&\quad + \nabla\cdot\left(\tfrac{1}{R^3}\nu nVV\nabla R\right) \\
X_{U\chi n}(U,\chi,n) &\equiv (n\nabla^2\nu + \langle n,\nu\rangle)\,[U,\chi] + n\Delta^* U\,[\nu,\chi] \\
&\quad + \nabla\cdot(\nu n\nabla\,[U,\chi] - n\,[U,\chi]\,\nabla\nu) - [\nu n\Delta^* U,\chi] \\
X_{\chi\chi n}(\chi,\chi,n) &\equiv \tfrac{1}{2}n\,\langle\nu,\langle\chi,\chi\rangle\rangle \\
&\quad - \nabla\cdot\left(\tfrac{1}{2}\nu n\nabla\,\langle\chi,\chi\rangle\right) \\
X_{\psi\psi}(\psi,\psi) &\equiv \tfrac{1}{R^2}\Delta^*\psi\,\langle\nu,\psi\rangle \\
&\quad - \nabla\cdot\left(\tfrac{1}{R^2}\nu\Delta^*\psi\nabla\psi\right) \\
X_{II}(I,I) &\equiv \tfrac{1}{R^2}I\,\langle\nu,I\rangle \\
&\quad - \nabla\cdot\left(\tfrac{1}{R^2}\nu I\nabla I\right)
\end{aligned}
\tag{D.98}
$$

$$
\begin{aligned}
\Psi_{\psi}(\psi) &\equiv \nu\psi \\
\Psi_{\psi U}(\psi,U) &\equiv \nu\,[U,\psi] \\
\Psi_{\psi\chi}(\psi,\chi) &\equiv -\nu\,\langle\chi,\psi\rangle \\
\Psi_{\psi I}(\psi,I) &\equiv d_i\nu\tfrac{1}{n}\,[\psi,I]
\end{aligned}
\tag{D.99}
$$

$$
\begin{array}{lcll}
I_I(I) & \equiv & \nu I & \\
I_{IU}(I,U) & \equiv & R^2\nu\left[U,\frac{I}{R^2}\right] & \\
I_{\psi V}(\psi,V) & \equiv & R^2\nu\left[\frac{V}{R^2},\psi\right] & \\
I_{I\chi}(I,\chi) & \equiv & \frac{I}{R^2}\left\langle R^2\nu,\chi\right\rangle & -\nabla\cdot(\nu I\nabla\chi) \\
I_{\psi\psi}(\psi,\psi) & \equiv & d_i\frac{\Delta^*\psi}{R^2 n}\left[\psi,R^2\nu\right] & +\left[d_i\frac{1}{n}\nu\Delta^*\psi,\psi\right] \\
I_{II}(I,I) & \equiv & d_i R^2\nu I\left[\frac{1}{R^2 n},I\right] & \\
I_{p_e}(p_e) & \equiv & d_i R^2\nu\left[\frac{1}{n},p_e\right] &
\end{array}
\tag{D.100}
$$

$$
\begin{array}{lcll}
P_p(p) & \equiv & \nu p & \\
P_{pU}(p,U) & \equiv & \nu\left[U,p\right] & \\
P_{p\chi}(p,\chi) & \equiv & \Gamma p\left\langle\nu,\chi\right\rangle+(\Gamma-1)\nu\left\langle p,\chi\right\rangle & -\nabla\cdot(\Gamma\nu p\nabla\chi) \\
P_{p_eI}(p_e,I) & \equiv & d_i\left(\frac{1}{n}\nu\left[p_e,I\right]+\Gamma\nu p_e\left[\frac{1}{n},I\right]\right) &
\end{array}
\tag{D.101}
$$

Terms Arising From Analytic B Advance The following terms arise from the procedure outlined in section 3.3.2 of using the analytic form of $\dot{\mathbf{B}}$ to eliminate the advanced-time magnetic field from the velocity advance.

$$
\begin{array}{lcl}
U_{U\psi\psi}(U,\psi,\psi) & \equiv & \frac{1}{R^2}\left\langle\left[R^2\nu,\psi\right],\left[U,\psi\right]\right\rangle-\frac{1}{R^2}\left[R^2\nu,\left[U,\psi\right]\right]\Delta^*\psi \\
 & & +\left[\nu\Delta^*\left[U,\psi\right],\psi\right]+\left[\nu\Delta^*\psi,\left[U,\psi\right]\right] \\
 & & -\nabla\cdot\left(\frac{1}{R^2}\left[R^2\nu,\psi\right]\nabla\left[U,\psi\right]\right) \\
U_{UII}(U,I,I) & \equiv & \left[R^2,\nu\right]I\left[U,\frac{I}{R^2}\right] \\
 & & -\left[R^2,\nu I\left[U,\frac{I}{R^2}\right]\right] \\
U_{V\psi I}(V,\psi,I) & \equiv & \left[R^2,\nu\right]I\left[\frac{V}{R^2},\psi\right] \\
 & & -\left[R^2,\nu I\left[\frac{V}{R^2},\psi\right]\right] \\
U_{\chi\psi\psi}(\chi,\psi,\psi) & \equiv & -\frac{1}{R^2}\left\langle\left[R^2\nu,\psi\right],\left\langle\chi,\psi\right\rangle\right\rangle+\frac{1}{R^2}\left[R^2\nu,\left\langle\chi,\psi\right\rangle\right]\Delta^*\psi \\
 & & -\left[\nu\Delta^*\left\langle\chi,\psi\right\rangle,\psi\right]-\left[\nu\Delta^*\psi,\left\langle\chi,\psi\right\rangle\right] \\
 & & +\nabla\cdot\frac{1}{R^2}\left[R^2\nu,\psi\right]\nabla\left\langle\chi,\psi\right\rangle \\
U_{\chi II}(\chi,I,I) & \equiv & \frac{1}{R^2}\left[\nu,R^2\right]I\left(I\Delta^*\chi+\left\langle I,\chi\right\rangle\right) \\
 & & -\left[\frac{1}{R^2}\nu I\left(I\Delta^*\chi+\left\langle I,\chi\right\rangle\right),R^2\right]
\end{array}
\tag{D.102}
$$

$$
\begin{aligned}
V_{U\psi I}(U,\psi,I) &\equiv [\nu,U]\,[I,\psi] + \tfrac{1}{R^2} I\,[U,R^2]\,[\nu,\psi] \\
&\quad + \left[R^2\nu\left[U,\tfrac{I}{R^2}\right],\psi\right] + [I,\nu\,[U,\psi]] \\
V_{V\psi\psi}(V,\psi,\psi) &\equiv -[\nu,\psi]\,[V,\psi] - \tfrac{1}{R^2} V\,[\psi,R^2]\,[\nu,\psi] \\
&\quad + \left[R^2\nu\left[\tfrac{V}{R^2},\psi\right],\psi\right] \\
V_{\chi\psi I}(\chi,\psi,I) &\equiv [\nu,\psi]\,(I\Delta^*\chi + \langle I,\chi\rangle) - \langle\chi,\psi\rangle\,[\nu,I] \\
&\quad - [\nu\,(I\Delta^*\chi + \langle I,\chi\rangle),\psi] - [I,\nu\,\langle\chi,\psi\rangle]
\end{aligned}
\tag{D.103}
$$

$$
\begin{aligned}
X_{Up}(U,p) &\equiv -\nabla^2\nu\,[U,p] \\
&\quad + \nabla\cdot([U,p]\,\nabla\nu - \nu\nabla\,[U,p]) \\
X_{\chi p}(\chi,p) &\equiv \nabla^2\nu\,(\Gamma p\nabla^2\chi + \langle p,\chi\rangle) \\
&\quad + \nabla\cdot[\nu\nabla\,(\Gamma p\nabla^2\chi + \langle p,\chi\rangle) - (\Gamma p\nabla^2\chi + \langle p,\chi\rangle)\,\nabla\nu] \\
X_{U\psi\psi}(U,\psi,\psi) &\equiv \tfrac{1}{R^2}\,\langle\nu,[U,\psi]\rangle\,\Delta^*\psi - \tfrac{1}{R^2}\,\langle\langle\nu,\psi\rangle\,,[U,\psi]\rangle \\
&\quad - \nabla\cdot\begin{pmatrix} \tfrac{1}{R^2}\nu\Delta^*\psi\nabla\,[U,\psi] + \tfrac{1}{R^2}\nu\Delta^*\,[U,\psi]\,\nabla\psi \\ - \quad \tfrac{1}{R^2}\,\langle\nu,\psi\rangle\,\nabla\,[U,\psi] \end{pmatrix} \\
X_{UII}(U,I,I) &\equiv -\nabla^2\nu I\left[U,\tfrac{I}{R^2}\right] \\
&\quad + \nabla\cdot\left[I\left[U,\tfrac{I}{R^2}\right]\nabla\nu - \tfrac{1}{R^2}\nu\nabla\left(R^2 I\left[U,\tfrac{I}{R^2}\right]\right)\right] \\
X_{V\psi I}(V,\psi,I) &\equiv -\Delta^*\nu I\left[\tfrac{V}{R^2},\psi\right] \\
&\quad + \nabla\cdot\left[I\left[\tfrac{V}{R^2},\psi\right]\nabla\nu - \tfrac{1}{R^2}\nu\nabla\left(R^2 I\left[\tfrac{V}{R^2},\psi\right]\right)\right] \\
X_{\chi\psi\psi}(\chi,\psi,\psi) &\equiv -\tfrac{1}{R^2}\,\langle\nu,\langle\chi,\psi\rangle\rangle\,\Delta^*\psi + \tfrac{1}{R^2}\,\langle\langle\nu,\psi\rangle\,,\langle\chi,\psi\rangle\rangle \\
&\quad \nabla\cdot\begin{pmatrix} \tfrac{1}{R^2}\nu\Delta^*\psi\nabla\,\langle\chi,\psi\rangle + \tfrac{1}{R^2}\nu\Delta^*\,\langle\chi,\psi\rangle\,\nabla\psi \\ - \quad \tfrac{1}{R^2}\,\langle\nu,\psi\rangle\,\nabla\,\langle\chi,\psi\rangle \end{pmatrix} \\
X_{\chi II}(\chi,I,I) &\equiv \tfrac{1}{R^2}\nabla^2\nu I\,(I\nabla^2\chi + \langle I,\chi\rangle) \\
&\quad + \nabla\cdot\left\{\begin{array}{ll} & \tfrac{1}{R^2}\nu\nabla\,[I\,(I\nabla^2\chi + \langle I,\chi\rangle)] \\ - & \tfrac{1}{R^2}\nabla\nu I\,(I\nabla^2\chi + \langle I,\chi\rangle) \end{array}\right\}
\end{aligned}
\tag{D.104}
$$

D.2.2 Collisional Forces

Assuming the collisional force **R** is of the form given by equation (3.2) (which neglects the thermal force), the contributions to the scalar equations due to this force are given by

$$\begin{array}{lcll} \Psi_{\psi\eta}(\psi) & \equiv & \nu\eta\Delta^*\psi & \\ I_{I\eta}(I) & \equiv & -\frac{1}{R^2}\eta\left\langle R^2\nu, I\right\rangle & +\nabla\cdot(\nu\eta\nabla I) \\ P_{\psi\psi\eta}(\psi,\psi) & \equiv & (\Gamma-1)\frac{1}{R^2}\nu\eta\Delta^*\psi\Delta^*\psi & \\ P_{I\eta}(I) & \equiv & (\Gamma-1)\frac{1}{R^2}\nu\eta\left\langle I, I\right\rangle. & \end{array} \tag{D.105}$$

D.2.3 Gravity

These terms are obtained assuming a gravitational force of the form given by equation (3.10). (Note that here the subscripts on g denote vector components, not derivatives.)

$$\begin{array}{lcl} U_{n\mathbf{g}}(n) & \equiv & g_R\nu\left[n, R\right] - g_Z R\nu\left\langle n, R\right\rangle \\ X_{n\mathbf{g}}(n) & \equiv & \frac{n}{R^2}\left(g_R\left\langle\nu, R\right\rangle + g_Z R\left[\nu, R\right]\right). \end{array} \tag{D.106}$$

Gravitational Terms Arising From Analytic Density Advance The numerical stability of simulations of gravitational modes may be greatly improved by Taylor expanding n in the gravity term of the velocity advance and using the analytic form of $\dot{n}$ to eliminate the advanced-time occurrences of n in that term (in the same manner as **B** is treated throughout the velocity advance). This procedure leads to the following terms:

$$\begin{array}{lcl} U_{Un\mathbf{g}}(U,n) & \equiv & -\left[n, U\right]\left(\frac{1}{R}g_Z\left\langle R^2\nu, R\right\rangle - \frac{1}{R^2}g_R\left[\nu, R\right]\right) \\ & & +\nabla\cdot\left(R\nu g_Z\left[n, U\right]\nabla R\right) - \left[\nu g_R\left[n, U\right], R\right] \\ U_{\chi n\mathbf{g}}(\chi,n) & \equiv & -\left(n\nabla^2\chi + \left\langle n,\chi\right\rangle\right)\left(\frac{1}{R}g_Z\left\langle R^2\nu, R\right\rangle - \frac{1}{R^2}g_R\left[\nu, R\right]\right) \\ & & +\nabla\cdot\left[\nu R g_Z\left(n\nabla^2\chi + \left\langle n,\chi\right\rangle\right)\nabla R\right] \\ & & -\left[\nu g_R\left(n\nabla^2\chi + \left\langle n,\chi\right\rangle\right), R\right] \end{array} \tag{D.107}$$

$$
\begin{aligned}
X_{Un\mathbf{g}}(U,n) &\equiv [U,n]\left(Rg_Z[\nu,R]+\tfrac{1}{R^2}g_R\langle\nu,R\rangle\right)\\
&\quad -[R\nu g_Z[U,n],R]-\nabla\cdot\left[\tfrac{1}{R^2}\nu g_R[U,n]\nabla R\right]\\
X_{\chi n\mathbf{g}}(\chi,n) &\equiv -\left(n\nabla^2\chi+\langle n,\chi\rangle\right)\left(Rg_Z[\nu,R]+\tfrac{1}{R^2}g_R\langle\nu,R\rangle\right)\\
&\quad -[R\nu g_Z\left(n\nabla^2\chi+\langle n,\chi\rangle\right),R]\\
&\quad -\nabla\cdot\left[\tfrac{1}{R^2}\nu g_R\left(n\nabla^2\chi+\langle n,\chi\rangle\right)\nabla R\right].
\end{aligned}
\tag{D.108}
$$

D.2.4 Heat Flux Terms

These terms are obtained assuming a heat flux density of the form given by equation (3.6).

$$
\begin{aligned}
P_{\kappa_\circ}(\kappa,T) &\equiv -(\Gamma-1)\nu\kappa_\circ\nabla^2T\\
P_{\kappa_\parallel}(\kappa_\parallel,T,\psi,\psi,B^{-2}) &\equiv -(\Gamma-1)\kappa_\parallel\tfrac{1}{B^2}[\psi,\nu][\psi,T]\\
&\quad +\nabla\cdot\left[(\Gamma-1)\nu\kappa_\parallel\mathbf{bb}\cdot\nabla T\right]\\
P_{\kappa_\times}(\kappa_\times,T,I,B^{-2}) &\equiv (\Gamma-1)\kappa_\times\tfrac{I}{B}[\nu,T]\\
&\quad +[(\Gamma-1)\nu\kappa_\times I,T],
\end{aligned}
\tag{D.109}
$$

where

$$
B^2 = \frac{1}{R^2}\left[\langle\psi,\psi\rangle+I^2\right].
$$

D.2.5 Density Source

The density source term is:

$$
N_\sigma(\sigma)\equiv\nu\sigma. \tag{D.110}
$$

The contributions to the momentum equation due to the density source

are:

$$\begin{aligned}
U_{U\sigma}(U,\sigma) &\equiv \tfrac{1}{R^2}\langle R^2\nu, U\rangle\,\sigma &&+ \nabla\cdot(\nu\sigma\nabla U)\\
U_{\chi\sigma}(\chi,\sigma) &\equiv -[R^2\nu,\chi]\,\sigma &&+ [\chi, R^2\nu\sigma]\\
V_{V\sigma}(V,\sigma) &\equiv -\nu V\sigma &&\\
X_{U\sigma}(U,\sigma) &\equiv [\nu,U]\,\sigma &&+ [U,\nu\sigma]\\
X_{\chi\sigma}(\chi,\sigma) &\equiv \langle\nu,\chi\rangle\,\sigma &&+ \nabla\cdot(\nu\sigma\nabla\chi)
\end{aligned} \tag{D.111}$$

The contributions to the pressure equation do to the density source are:

$$\begin{aligned}
P_\sigma &\equiv P_{UU\sigma} + P_{VV\sigma} + P_{\chi\chi\sigma} + P_{U\chi\sigma}\\
P_{UU\sigma}(U,U,\sigma) &\equiv \tfrac{1}{2R^2}\nu\sigma\,\langle U,U\rangle\\
P_{VV\sigma}(V,V,\sigma) &\equiv \tfrac{1}{2R^2}\nu\sigma V^2\\
P_{\chi\chi\sigma}(\chi,\chi,\sigma) &\equiv \tfrac{1}{2}\nu\sigma\,\langle\chi,\chi\rangle\\
P_{\sigma U\chi}(U,\chi,\sigma) &\equiv \nu\sigma\,[\chi,U]
\end{aligned} \tag{D.112}$$

D.2.6 Viscosity

The viscous terms are each the sum of the isotropic, parallel, and gyroviscous contributions:

$$A_{B\Pi}(B) = A_{B\Pi_\circ}(B) + A_{B\Pi_\parallel}(B) + A_{B\Pi_\wedge}(B)$$

where A and B are each one of $\{U, V, \chi\}$. Each contribution is described in the following sections.

Isotropic Viscosity

These terms result from isotropic viscosity of the form given by equation (3.4c).

$$\begin{aligned}
U_{U\Pi_\circ}(U) &\equiv \tfrac{1}{R^2}\left[\left(\langle\mu, R^2\nu\rangle + \mu\Delta^*(R^2\nu)\right)\Delta^* U\right. \\
&\quad \left. + \nabla^2\mu\,\langle R^2\nu, U\rangle + \Delta^*(R^2\nu)\,\langle\mu, U\rangle\right] \\
U_{\chi\Pi_\circ}(\chi) &\equiv -\nabla^2(R^2\nu)\,[\mu,\chi] - \Delta^*\mu\,[R^2\nu,\chi] \\
&\quad - \tfrac{1}{R^2}\Delta^*(R^2\chi)\,[R^2\nu,\mu] \\
V_{V\Pi_\circ}(V) &\equiv \left[\langle\nu,\mu\rangle + \tfrac{1}{R^2}\mu\Delta^*(R^2\nu)\right] V \\
X_{U\Pi_\circ}(U) &\equiv \nabla^2\nu\,[\mu, U] + \nabla^2\mu\,[\nu, U] + \Delta^* U\,[\nu,\mu] \\
X_{\chi\Pi_\circ}(\chi) &\equiv \nabla^2\nu\,\langle\mu,\chi\rangle + \nabla^2\mu\,\langle\nu,\chi\rangle + 2\mu_c\nabla^2\nu\nabla^2\chi
\end{aligned} \tag{D.113}$$

Parallel Viscosity

These terms are obtained assuming a parallel viscosity of the form given in equation (3.4a). These equations were obtained using equations (D.92)–(D.94). For compactness, derivatives are written as subscripts in the following expressions (*i.e.* $\nu_Z = \partial_Z\nu$).

Each term takes the form

$$A_{B\Pi_\parallel}(B) \equiv \mu_\parallel D_A S_B \tag{D.114}$$

where A and B are each one of $\{U, V, \chi\}$.

$$\begin{aligned}
D_U &= \frac{3}{B^2}\left\{-\frac{1}{2}R^2\left[\nu, \frac{\langle\psi,\psi\rangle}{R^2}\right] + \langle\psi,[\nu,\psi]\rangle - \frac{1}{R^2}I^2\nu_Z\right. \\
&\quad \left. - \frac{2}{R^2}\left[\nu_Z(\psi_Z^2 - \psi_R^2) + 2\nu_R\psi_R\psi_Z\right]\right\} \\
D_V &= -3\frac{I}{B^2}\,[\nu,\psi] \\
D_X &= -\nabla^2\nu\left(1 - 3\frac{\langle\psi,\psi\rangle}{R^2B^2}\right) \\
&\quad + \frac{3}{R^2B^2}\left(\frac{1}{2}R^2\left\langle\nu, \frac{\langle\psi,\psi\rangle}{R^2}\right\rangle - \langle\psi,\langle\nu,\psi\rangle\rangle + \frac{1}{R}I^2\nu_R\right)
\end{aligned}$$

$$
\begin{aligned}
S_U &= \frac{1}{R^2B^2}\left(-\frac{1}{2}R^2\left[U,\frac{\langle\psi,\psi\rangle}{R^2}\right]+\langle\psi,[U,\psi]\rangle-\frac{1}{R^2}I^2U_Z\right)\\
S_V &= -\frac{I}{B^2}\left[\psi,\frac{V}{R^2}\right]\\
S_\chi &= \frac{1}{R^2B^2}\left(\frac{1}{2}R^2\left\langle\chi,\frac{\langle\psi,\psi\rangle}{R^2}\right\rangle-\langle\psi,\langle\chi,\psi\rangle\rangle+\frac{1}{R}I^2\chi_R+\nabla^2\chi\,\langle\psi,\psi\rangle\right)\\
&\quad -\frac{1}{3}\nabla^2\chi
\end{aligned}
$$

Gyroviscosity

These terms are obtained using equations (D.92)–(D.94) assuming a gyroviscosity of the form given by equation (3.4b).

$$
\begin{aligned}
U_{U\sqcap_\wedge}(U) &\equiv \frac{p_iI}{2R^3B^2}\\
&\times\left\{\begin{array}{l}
\left(1+\frac{3}{2}\frac{\langle\psi,\psi\rangle}{R^2B^2}\right)\left[\begin{array}{c}([R^3\nu_Z]_Z-[R^3\nu_R]_R)\left(\left[\frac{U_R}{R}\right]_Z+\left[\frac{U_Z}{R}\right]_R\right)\\ -([R^3\nu_R]_Z+[R^3\nu_Z]_R)\left(\left[\frac{U_Z}{R}\right]_Z-\left[\frac{U_R}{R}\right]_R\right)\end{array}\right]\\
+\frac{9}{2RB^2}\\
\times\left[\begin{array}{l}(\psi_Z^2-\psi_R^2)\left(\begin{array}{l}R\nu_Z\left[\left(\frac{U_Z}{R}\right)_Z-\left(\frac{U_R}{R}\right)_R\right]\\ -\frac{1}{R^3}U_Z\left[(R^3\nu_Z)_Z-(R^3\nu_R)_R\right]\end{array}\right)\\ +2\psi_R\psi_Z\left(\begin{array}{l}R\nu_Z\left[\left(\frac{U_R}{R}\right)_Z+\left(\frac{U_Z}{R}\right)_R\right]\\ -\frac{1}{R^3}U_Z\left[(R^3\nu_R)_Z+(R^3\nu_Z)_R\right]\end{array}\right)\end{array}\right]
\end{array}\right\}
\end{aligned}
$$

$$
\begin{aligned}
U_{V\sqcap_\wedge}(V) &\equiv \frac{p_i}{B^2} \\
&\times \left\{ \begin{array}{l}
\frac{1}{4R^2}\left(1-\frac{3I^2}{B^2R^2}\right) \\
\times \left(\left\langle \frac{V}{R^2}, R^4\left[\psi,\nu\right]\right\rangle - \left\langle \psi, R^4\left[\nu,\frac{V}{R^2}\right]\right\rangle + \frac{1}{R^2}\left[\nu, R^6\left\langle\frac{V}{R^2},\psi\right\rangle\right]\right) \\
-\frac{3}{4B^2}\left[\psi,\frac{V}{R^2}\right] \\
\times \left(2\left\langle\psi,\left\langle\psi,\nu\right\rangle\right\rangle - R^2\left\langle\nu,\frac{\langle\psi,\psi\rangle}{R^2}\right\rangle - \Delta^*\nu\left\langle\psi,\psi\right\rangle + 6\psi_Z\left[\nu,\psi\right]\right) \\
+\frac{9I^2}{2R^2B^2}\nu_Z\left\langle\psi,\frac{V}{R^2}\right\rangle
\end{array} \right\}
\end{aligned}
$$

$$
\begin{aligned}
U_{\chi\sqcap_\wedge}(\chi) &\equiv \frac{p_i I}{2R^3B^2} \\
&\times \left\{ \begin{array}{l}
\left[\left(\chi_{RR}-\chi_{ZZ}\right)\left([R^3\nu_R]_R - [R^3\nu_Z]_Z\right) + 2\chi_{RZ}\left([R^3\nu_R]_Z + [R^3\nu_Z]_R\right)\right] \\
+\frac{3}{R^2B^2}\left[\begin{array}{l}
\left(\Delta^*\chi[\psi_Z^2-\psi_R^2] - \chi_{ZZ}\psi_Z^2 + \chi_{RR}\psi_R^2\right) \\
\times \left([R^3\nu_R]_R - [R^3\nu_Z]_Z\right) \\
+ 2\chi_{RZ}\left(\psi_Z^2[R^3\nu_R]_Z + \psi_R^2[R^3\nu_Z]_R\right) \\
-2\psi_R\psi_Z\left(\begin{array}{l}
\left[\chi_{ZZ}-\frac{1}{R}\chi_R\right][R^3\nu_R]_Z \\
+\left[\chi_{RR}-\frac{1}{R}\chi_R\right][R^3\nu_Z]_R
\end{array}\right)
\end{array}\right]
\end{array} \right\}
\end{aligned}
$$

$$
\begin{aligned}
V_{U\sqcap_\wedge}(U) &\equiv -\frac{p_i}{4RB^2} \\
&\times \left\{ \begin{array}{l}
\left(1-3\frac{I^2}{R^2B^2}\right)\left(\begin{array}{l}
\left\langle\psi, R\left[U,\nu\right]\right\rangle + \left\langle\nu, R\left[U,\psi\right]\right\rangle \\
-\frac{1}{R^3}\left[U, R^4\left\langle\nu,\psi\right\rangle\right] + U_R\left[\nu,\psi\right] + \frac{2}{R}\psi_Z\left\langle\nu,U\right\rangle
\end{array}\right) \\
+\frac{3}{RB^2}\left[\psi,\nu\right]\left(\begin{array}{l}
2\left\langle\psi,\left\langle U,\psi\right\rangle\right\rangle - \Delta^* U\left\langle\psi,\psi\right\rangle \\
-\frac{1}{R^2}\left\langle U, R^2\left\langle\psi,\psi\right\rangle\right\rangle + \left[\psi,R^2\right]\left[\psi,U\right]
\end{array}\right) \\
-18\frac{I^2}{R^2B^2}\left[U,R\right]\left\langle\nu,\psi\right\rangle
\end{array} \right\}
\end{aligned}
$$

$$
V_{V\sqcap_\wedge}(V) \equiv -\frac{p_i I R^2}{B^2}\left(1-\frac{3}{2}\frac{\langle\psi,\psi\rangle}{R^2B^2}\right)\left[\nu,\frac{V}{R^2}\right]
$$

$$V_{\chi\sqcap_\wedge}(\chi) \equiv -\frac{p_i}{B^2} \times \left\{ \begin{array}{l} \frac{1}{4}\left(\frac{1}{R^2}\left\langle \chi, R^2\left\langle \nu,\psi\right\rangle\right\rangle - \left\langle \nu,\left\langle \chi,\psi\right\rangle\right\rangle - \left\langle \psi,\left\langle \nu,\chi\right\rangle\right\rangle\right) \\ +\frac{3}{2RB^2}\left[\psi,\nu\right]\left(\left\langle \psi, R\left[\chi,\psi\right]\right\rangle - \frac{1}{2}R\left[\chi,\left\langle \psi,\psi\right\rangle\right]\right) \\ +\frac{3}{4}\frac{I^2}{R^2B^2}\left(\left\langle \psi,\left\langle \chi,\nu\right\rangle\right\rangle + \left\langle \nu,\left\langle \chi,\psi\right\rangle\right\rangle - \left\langle \chi,\left\langle \nu,\psi\right\rangle\right\rangle - 2\Delta^*\chi\left\langle \nu,\psi\right\rangle\right) \end{array} \right\}$$

$$X_{U\sqcap_\wedge}(U) \equiv -\frac{p_i I}{2R^2B^2} \times \left\{ \begin{array}{l} \left\langle\left\langle \nu,U\right\rangle\right\rangle - R^2\left[\left[\nu,U\right]\right] + \frac{1}{R}\left[U_R(\nu_{ZZ}-\nu_{RR}) - 2U_Z\nu_{RZ} - \frac{1}{R}U_R\nu_R\right] \\ +\frac{3}{RB^2}\left[\begin{array}{l} \left(\left[\frac{U_Z}{R}\right]_Z - \left[\frac{U_R}{R}\right]_R\right)\left(\nu_{ZZ}\psi_R^2 - \nu_{RR}\psi_Z^2 + \frac{1}{R}\nu_R[\psi_Z^2-\psi_R^2]\right) \\ +2\nu_{RZ}\left(\left[\frac{U_R}{R}\right]_Z\psi_R^2 + \left[\frac{U_Z}{R}\right]_R\psi_Z^2 - \frac{1}{R^2}U_Z[\psi_Z^2-\psi_R^2]\right) \\ -2\psi_R\psi_Z\left(\begin{array}{l} \left[\frac{U_R}{R}\right]_Z\nu_{RR} + \left[\frac{U_Z}{R}\right]_R\nu_{ZZ} \\ -\frac{1}{R^2}U_Z[\nu_{ZZ}-\nu_{RR}] \\ -\frac{1}{R}\nu_R\left[\left(\frac{U_R}{R}\right)_Z + \left(\frac{U_Z}{R}\right)_R\right] \end{array}\right) \end{array}\right] \end{array} \right\}$$

$$X_{V\sqcap_\wedge}(V) \equiv -\frac{p_i}{4B^2} \times \left\{ \begin{array}{l} \left(1-\frac{3}{R^2}\frac{I^2}{B^2}\right)\left(\frac{1}{R^2}\left\langle \nu, R^2\left\langle \frac{V}{R^2},\psi\right\rangle\right\rangle - \left\langle \psi,\left\langle \frac{V}{R^2},\nu\right\rangle\right\rangle - \left\langle \frac{V}{R^2},\left\langle \psi,\nu\right\rangle\right\rangle\right) \\ +\frac{6}{B^2}\left[\psi,\frac{V}{R^2}\right]\left(\frac{1}{R}\left\langle \psi, R\left[\nu,\psi\right]\right\rangle - \frac{1}{2}\left[\nu,\left\langle \psi,\psi\right\rangle\right]\right) \\ -6\frac{I^2}{B^2}\left\langle \psi,\frac{V}{R^2}\right\rangle\left[\left(\frac{\nu_Z}{R^2}\right)_Z + \left(\frac{\nu_R}{R^2}\right)_R\right] \end{array} \right\}$$

$$X_{\chi\sqcap_\wedge}(\chi) \equiv \frac{p_i I}{B^2} \times \left\{ \begin{array}{l} \left(1+\frac{3}{2R^2}\frac{\left\langle \psi,\psi\right\rangle}{B^2}\right)\left[\left\langle \nu,\chi\right\rangle\right] \\ +\frac{3}{2B^2}\left[\begin{array}{c} \left(-\frac{1}{2}\left[\chi,\left\langle \psi,\psi\right\rangle\right] + \frac{1}{R}\left\langle \psi, R\left[\chi,\psi\right]\right\rangle\right)\left(\left[\frac{\nu_R}{R^2}\right]_R + \left[\frac{\nu_Z}{R^2}\right]_Z\right) \\ -\left(-\frac{1}{2}\left[\nu,\left\langle \psi,\psi\right\rangle\right] + \frac{1}{R}\left\langle \psi, R\left[\nu,\psi\right]\right\rangle\right)\left(\left[\frac{\chi_R}{R^2}\right]_R + \left[\frac{\chi_Z}{R^2}\right]_Z\right) \end{array}\right] \end{array} \right\}$$

Viscous Heating

The contributions from viscous heating ($-\mathsf{\Pi} : \nabla\mathbf{u}$) are

$$\begin{aligned}
P_{\mathsf{\Pi}_\circ} &= P_{\mathsf{\Pi}_\circ UU} + P_{\mathsf{\Pi}_\circ VV} + P_{\mathsf{\Pi}_\circ \chi\chi} + P_{\mathsf{\Pi}_\circ U\chi} \\
P_{\mathsf{\Pi}_\circ UU}(U,U) &\equiv \nu\mu\left(\tfrac{1}{R^2}\Delta^* U\Delta^* U - \tfrac{1}{2}\left[[U,U]\right] - \tfrac{1}{R}\left[U, \tfrac{1}{R}U_Z\right]\right) \\
P_{\mathsf{\Pi}_\circ VV}(V,V) &\equiv \nu\mu R^2\left\langle \tfrac{V}{R^2}, \tfrac{V}{R^2}\right\rangle \\
P_{\mathsf{\Pi}_\circ \chi\chi}(\chi,\chi) &\equiv 2\nu(\mu_c - \mu)\nabla^2\chi\nabla^2\chi - 2\nu\mu\left\langle\langle \chi,\chi\rangle\right\rangle \\
P_{\mathsf{\Pi}_\circ U\chi}(U,\chi) &\equiv -4\nu\mu\left(\left[\langle U,\chi\rangle\right] - \left[U, \tfrac{1}{R}\chi_R\right]\right), \\
P_{\mathsf{\Pi}_\parallel} &\equiv 3\mu_\parallel\left(\tfrac{1}{2}\mathbf{b}\cdot\mathsf{W}\cdot\mathbf{b}\right)^2 \\
P_{\mathsf{\Pi}_\wedge} &\equiv 0
\end{aligned} \tag{D.115}$$

where $\frac{1}{2}\mathbf{b}\cdot\mathsf{W}\cdot\mathbf{b} = S_U + S_V + S_\chi$, as defined in section D.2.6. Note that gyroviscosity is not dissipative, and does not contribute to viscous heating.

D.2.7 Electron Viscosity

The contribution from electron viscous heating ($d_i\mathsf{\Pi}_e : \nabla\frac{\mathbf{J}}{n}$) is

$$\begin{aligned}
P_{\mathsf{\Pi}_e} \equiv\ & \nu\lambda\left[n\left\langle\frac{\Delta^*\psi}{nR}, \frac{\Delta^*\psi}{R}\right\rangle + \frac{1}{R^4}(\Delta^*\psi)^2\right. \\
& \left. + \frac{1}{R^2}\left(\langle\langle I,I\rangle\rangle - \frac{2}{R^2}I_R^2 + \frac{1}{2}nR^4\left\langle\frac{1}{nr^2}, \frac{\langle I,I\rangle}{R^2}\right\rangle\right)\right]
\end{aligned} \tag{D.116}$$

Bibliography

[1] M. Ono, S. M. Kaye, Y.-K. M. Peng, G. Barnes, W. Blanchard, M. D. Carter, J. Chrzanowski, L. Dudek, R. Ewig, D. Gates, R. E. Hatcher, T. Jarboe, S. C. Jardin, D. Johnson, R. Kaita, M. Kalish, C. E. Kessel, H. W. Kugel, R. Maingi, R. Majeski, J. Manickam, B. McCormack, J. Menard, D. Mueller, B. A. Nelson, B. E. Nelson, C. Neumeyer, G. Oliaro, F. Paoletti, R. Parsells, E. Perry, N. Pomphrey, S. Ramakrishnan, R. Raman, G. Rewoldt, J. Robinson, A. L. Roquemore, P. Ryan, S. Sabbagh, D. Swain, E. J. Synakowski, M. Viola, M. Willians, J. R. Wilson, and NSTX Team. Exploration of spherical torus physics in the NSTX device. *Nucl. Fusion*, 40(3Y):557–561, 2000.

[2] R. Aymar, V. A. Chuyanov, M. Huguet, and Y. Shimomura. Overview of ITER-FEAT the future of international burning plasma experiment. *Nucl. Fusion*, 41(10):1301, 2001.

[3] F. Wagner, G. Becker, K. Behringer, D. Campbell, A. Eberhagen, W. Engelhardt, G. Fussmann, O. Gehre, J. Gernhardt, G. v. Gierke, G. Haas, M. Huang, F. Karger, M. Keilhacker, O. Klüber, M. Kornherr, K. Lackner, G. Lisitano, G. G. Lister, H. M. Mayer, D. Meisel, E. R. Müller, H. Murmann, H. Niedermeyer, W. Poschenrieder, H. Rapp, H. Röhr, F. Schneider, G. Siller, E. Speth, A. Stäbler, K. H. Steuer, G. Venus, O. Vollmer, and Z. Yü. Regime of improved confinement

and high beta in neutral-beam-heated divertor discharges of the asdex tokamak. *Phys. Rev. Lett.*, 49(19):1408–1412, November 1982.

[4] H. Biglari, P. H. Diamond, and P. W. Terry. Influence of sheared poloidal rotation on edge turbulence. *Phys. Fluids B*, 2(1):1–3, 2001.

[5] K. H. Burrell. Effects of $E \times B$ velocity shear and magnetic shear on turbulence and transport in magnetic confinement devices. *Phys. Plasmas*, 4:1499, May 1997.

[6] K. C. Shaing and Jr. E. C. Crume. Bifurcation theory of poloidal rotation in tokamaks: a model for L-H transition. *Phys. Rev. Lett.*, 63(21):2369–2372, 1989.

[7] A. B. Hassam, Jr. T. M. Antonsen, J. F. Drake, P. N. Guzdar, C. S. Liu, D. R. McCarthy, and F. L. Waelbroeck. Spontaneous and driven perpendicular rotation in tokamaks. *Phys. Fluids B*, 5(7):2519–2524, 1993.

[8] F. L. Hinton. Thermal confinement bifurcation and the L- to H-mode transition in tokamaks. *Phys. Fluids B*, 3:696, March 1991.

[9] H. Zohm. Edge localized modes (ELMs). *Plasma Phys. Control. Fusion*, 38:105–128, 1996.

[10] J. W. Connor. Edge-localized modes—physics and theory. *Plasma Phys. Control. Fusion*, 40:521–542, 1998.

[11] P. B. Snyder, H. R. Wilson, J. R. Ferron, L. L. Lao, W. Leonard, T. H. Osborne, and A. D. Turnbull. Edge localized modes and the pedestal: a model based on couples peeling-ballooning modes. *Phys. Plasmas*, 9:2037, May 2002.

[12] A. Y. Aydemir. Shear flows at the tokamak edge and their interaction with edge-localized modes. *Phys. Plasmas*, 14, 2007.

[13] M. N. Rosenbluth, N. A. Krall, and N. Rostoker. Finite Larmor radius stabilization of "weakly" unstable confined plasmas. *Nucl. Fusion Suppl.*, 1:143, 1962.

[14] Harold P. Furth, John Killeen, and Marshall N. Rosenbluth. Finite-resistivity instabilities of a sheet pinch. *Phys. Fluids*, 6(4):459–484, April 1963.

[15] J. Birn, J. F. Drake, M. A. Shay, B. N. Rogers, R. E. Denton, M. Hesse, M. Kuznetsova, Z. W. Ma, A. Bhattacharjee, A. Otto, and P. L. Pritchett. Geospace environmental modeling (GEM) magnetic reconnection challenge. *J. Geophys. Res*, 106(A3):3715–3719, March 2001.

[16] R. Samtaney, S. C. Jardin, P. Coletta, and D. F. Martin. 3d adaptive mesh refinement simulations of pellet injection in tokamaks. *Comput. Phys. Comm.*, 164:220–228, December 2004.

[17] A. H. Glasser and X. Z. Tang. The SEL macroscopic modeling code. *Comput. Phys. Comm.*, 164:237–243, December 2004.

[18] A. Y. Aydemir and D. C. Barnes. Three-dimensional nonlinear incompressible MHD calculations. *J. Comp. Phys.*, 53(1):100–123, January 1984.

[19] W. Park, E. V. Belova, G. Y. Fu, X. Z. Tang, H. R. Strauss, and L. E. Sugiyama. Plasma simulation studies using multilevel physics models. *Phys. Plasmas*, 6(5):1796–1803, May 1999.

[20] C.R. Sovinec, A.H. Glasser, T.A. Gianakon, D.C. Barnes, R.A. Nebel, S.E. Kruger, S.J. Plimpton, A. Tarditi, M.S. Chu, and the NIMROD Team. Nonlinear magnetohydrodynamics with high-order finite elements. *J. Comp. Phys.*, 195:355, 2004.

[21] N. M. Ferraro and S. C. Jardin. Finite element implementation of Braginskii's gyroviscous stress with application to the gravitational instability. *Phys. Plasmas*, 13(9):092101, September 2006.

[22] S. C. Jardin, J. Breslau, and N. Ferraro. A high-order implicit finite element method for integrating the two-fluid magnetohydrodynamic equations in two dimensions. *J. Comp. Phys.*, 226(2):2146–2174, October 2007.

[23] Nathaniel M. Ferraro. Finite Larmor radius effects on the magnetorotational instability. *ApJ*, 662(1):512–516, June 2007.

[24] J. A. Krommes. Course notes for *Irreversible Processes in Plasma*. 2004.

[25] Glenn Bateman. *MHD Instabilities*. The MIT Press, Cambridge, Massachusetts, 1978.

[26] S. Chapman and T. G. Cowling. *The Mathematical Theory of Nonuniform Gases*. Cambridge University Press, London, 1953.

[27] S. I. Braginskii. Transport processes in a plasma. In M. A. Leontovich, editor, *Reviews of Plasma Physics*, volume 1, pages 205–311. Consultants Bureau, New York, 1965.

[28] J. J. Ramos. Fluid formalism for collisionless magnetized plasmas. *Phys. Plasmas*, 12:052102, April 2005.

[29] V. S. Tsypin A. B. Mikhailovskii. Transport equations and the gradient instabilities in a high pressure collisional plasma. *Plasma Physics*, 13:785–798, 1971.

[30] J. J. Ramos. General expression of the gyroviscous force. *Phys. Plasmas*, 12:112301, 2005.

[31] G. F. Chew, M. L. Goldberger, and F. E. Low. The Boltzmann equations and the one-fluid hydromagnetic equations in the absence of particle collisions. *Proc. Royal Soc. London A*, 236(1204), July 1956.

[32] Adil B. Hassam and Russell M. Kulsrud. Time evolution of mass flows in a collisional tokamak. *Phys. Fluids*, 21(12):2271–2279, December 1978.

[33] S. P. Hirshman and D. J. Sigmar. Neoclassical transport of impurities in tokamak plasmas. *Nucl. Fusion*, 21(9):1079, 1981.

[34] A. A. Galeev and R. Z. Sagdeev. Transport phenomena in a collisionless plasma in a toroidal magnetic system. *Soviet Physics JETP*, 26:233, January 1968.

[35] P. B. Snyder, G. W. Hammett, and W. Dorland. Landau fluid models of collisionless magnetohydrodynamics. *Phys. Plasmas*, 4(11):3974, November 1997.

[36] M. A. Beer and G. W. Hammett. The dynamics of small-scale turbulence-driven flows. In *Proceedings of the Varenna-Lausanne International Workshop*, page 19, Bologna, Italy, 1998. Societá Italiana di Fisica, Editrice Compositori.

[37] J. J. Ramos. Fluid theory of magnetized plasma dynamics at low collisionality. *Phys. Plasmas*, 14:052506, 2007.

[38] K. C. Shaing. Extending the collisional fluid equations in to the long mean-free-path regime in toroidal plasmas. IV banana regime. *Phys. Plasmas*, 14:112509, 2007.

[39] T. A. Gianakon, S. E. Kruger, and C. C. Hegna. Heuristic closures for numerical simulations of neoclassical tearing modes. *Phys. Plasmas*, 9(2):536–547, February 2002.

[40] G. W. Hammett and F. W. Perkins. Fluid moment models for Landau damping with application to the ion-temperature-gradient instability. *Phys. Rev. Lett.*, 64(25):3019–3022, 1990.

[41] G. W. Hammett, W. Dorland, and F. W. Perkins. Fluid models of phase mixing, Landau damping, and nonlinear gyrokinetic dynamics. *Phys. Fluids B*, 4(7):2052, July 1992.

[42] Eliot Quataert, William Dorland, and Gregory Hammett. Magnetorotational instability in a collisionless plasma. *ApJ*, 577:524–533, September 2002.

[43] Prateek Sharma, Gregory W. Hammett, and Eliot Quataert. Transition from collisionless to collisional magnetorotational instability. *ApJ*, 596:1121–1130, October 2003.

[44] Tanim Islam and Steven Balbus. Dynamics of the magnetoviscous instability. *ApJ*, 633:328–333, November 2005.

[45] M. N. Rosenbluth and F. L. Hinton. Ploidal flow driven by ion temperature-gradient turbulence in tokamaks. *Phys. Rev. Lett.*, 80(4):724–727, January 1998.

[46] A. M. Dimits, G. Bateman, M. A. Beer, B. I. Cohen, W. Dorland, G. W. Hammett, C. Kim, J. E. Kinsey, M. Kotschenreuther, A. H. Kritz, L. L. Lao, J. Mandrekas, W. M. Nevins, S. E. Parker, A. J. Redd, D. E. Shumaker, R. Sydora, and J. Weiland. Comparisons and physics basis of tokamak transport models and turbulence simulations. *Phys. Plasmas*, 7(3):969–983, March 2000.

[47] G. W. Hammett. Private communication.

[48] Z. Chang and J. D. Callen. Unified fluid/kinetic description of plasma microinstabilities. part I: Basic equations in a sheared slab geometry. *Phys. Fluids B*, 4(5):1167, may 1992.

[49] A. Brizard. Nonlinear gyrofluid description of turbulent magnetized plasmas. *Phys. Fluids B*, 4(5):1213, May 1992.

[50] G. M. Staebler, J. E. Kinsey, and R. E. Waltz. A theory-based transport model with comprehensive physics. *Phys. Plasmas*, 14:055909, 2007.

[51] S. C. Jardin. A triangular finite element with first-derivative continuity applied to fusion MHD applications. *J. Comp. Phys.*, 200:133–152, 2004.

[52] S. C. Jardin and J. A. Breslau. Implicit solution of the four-field extended-magnetohydrodynamic equations using high-order high-continuity finite elements. *Phys. Plasmas*, 12:056101, 2005.

[53] D. A. Dunavant. High degree efficient symmetrical gaussian quadrature rules for the triangle. *Int. J. Numer. Methods Eng.*, 21:1129–1148, 1985.

[54] George Karypis and Vipin Kumar. A parallel algorithm for multilevel graph partitioning and sparse matrix ordering. In *10th Intl. Parallel Processing Symposium*, pages 314–319, 1996.

[55] Karen Devine, Erik Boman, Robert Heaphy, Bruce Hendrickson, and Courtenay Vaughan. Zoltan data management services for parallel dynamic applications. *Computing in Science and Engineering*, 4(2):90–97, 2002.

[56] Erik Boman, Karen Devine, Lee Ann Fisk, Robert Heaphy, Bruce Hendrickson, Vitus Leung, Courtenay Vaughan, Umit Catalyurek, Doruk Bozdag, and William Mitchell. Zoltan home page. http://www.cs.sandia.gov/Zoltan, 1999.

[57] Douglas S. Harned and D. D. Schnack. Semi-implicit method for long time scale magnetohydrodynamic computations in three dimensions. *J. Comp. Phys.*, 65(1):57–70, July 1986.

[58] Edward J. Caramana. Derivation of implicit difference schemes by the method of differential approximation. *J. Comp. Phys.*, 96:484–493, 1991.

[59] L. Chacón and D. A. Knoll. A 2D high-β Hall mhd implicit nonlinear solver. *J. Comp. Phys.*, 188(2):573–592, July 2003.

[60] Richard Fitzpatrick. Scaling of forced magnetic reconnection in the Hall-magnetohydrodynamic Taylor problem. *Phys. Plasmas*, 11(3):937–946, March 2004.

[61] Xiaoye S. Li and James W. Demmel. SuperLU_DIST: A scalable distributed-memory sparse direct solver for unsymmetric linear systems. *ACM Trans. Mathematical Software*, 29(2):110–140, June 2003.

[62] Satish Balay, Kris Buschelman, William D. Gropp, Dinesh Kaushik, Matthew G. Knepley, Lois Curfman McInnes, Barry F. Smith, and Hong Zhang. PETSc Web page, 2001. http://www.mcs.anl.gov/petsc.

[63] Satish Balay, William D. Gropp, Lois Curfman McInnes, and Barry F. Smith. Efficient management of parallelism in object oriented numerical software libraries. In E. Arge, A. M. Bruaset, and H. P. Langtangen, editors, *Modern Software Tools in Scientific Computing*, pages 163–202. Birkhäuser Press, 1997.

[64] Daniel R. Reynolds, Ravi Samtaney, and Carol S. Woodward. A fully implicit numerical method for single fluid resistive magnetohydrodynamics. *J. Comp. Phys.*, 219(1):144–162, November 2006.

[65] Vyacheslav S. Lukin. *Computational Study of the internal kink mode evolution and associated magnetic reconnection phenomena*. PhD thesis, Princeton University, January 2008.

[66] S. C. Jardin, N. Ferraro, X. Luo, J. Chen, J. Breslau, K. E. Jansen, and M. S. Shepard. The M3D-C^1 approach to simulating 3D 2-fluid magnetohydrodynamics in magnetic fusion experiments. *J. Phys.: Conf. Ser.*, 125:012044, 2008.

[67] K. V. Roberts and J. B. Taylor. Magnetoydrodynamic equations of finite Larmor radius. *Phys. Rev. Lett.*, 8(5):197–198, March 1962.

[68] Allan N. Kaufman. Plasma viscosity in a magnetic field. *Phys. Fluids*, 3(4):610–616, 1960.

[69] D. D. Schnack, D. C. Barnes, D. P. Brennan, C. C. Hegna, E. Held, C. C. Kim, S. E. Kruger, A. Y. Pankin, and C. R. Sovinec. Computational modeling of fully ionized magnetized plasmas using the fluid approximation. *Phys. Plasmas*, 13:058103, May 2006.

[70] W. B. Thompson. The dynamics of high temperature plasmas. *Reports on Progress in Physics*, 24, 1961.

[71] Steven A. Balbus and John F. Hawley. A powerful local shear instability in weakly magnetized disks. I. linear analysis. *ApJ*, 376:214–222, July 1991.

[72] Mark Wardle. The Balbus-Hawley instability in weakly ionized disks. *MNRAS*, 307:849–856, August 1999.

[73] Steven A. Balbus and Caroline Terquem. Linear analysis of the hall effect in protostellar disks. *ApJ*, 552:235–247, May 2001.

[74] Raquel Salmeron and Mark Wardle. Magnetorotational instability in stratified, weakly ionized accretion disks. *MNRAS*, 345:992–1008, 2003.

[75] Julian H. Krolik and Ellen G. Zweibel. The weak-field limit of the magnetorotational instability. *ApJ*, 644:651–661, June 2006.

[76] Steven A. Balbus. Viscous shear instability in weakly magnetized, dilute plasmas. *ApJ*, 616:857–864, December 2004.

[77] Steven A. Balbus and John F. Hawley. Instability, turbulence, and enhanced transport in accretion disks. *Rev. Mod. Phys.*, 70(1):1–53, January 1998.

[78] Steven A. Balbus. Stability, instability and "backward" transport in stratified fluids. *ApJ*, 534:420–427, May 2000.

[79] Ian J. Parrish and James. M. Stone. Nonlinear evolution of the magnetothermal instability in two dimensions. *ApJ*, 633:334–348, 2005.

[80] L. E. Zakharov and A. Pletzer. Toroidal magnetohydrodynamic code ESC, August 2008. http://w3.pppl.gov/ntcc/ESC/.

[81] A. Pletzer. NTCC JSOLVER module, August 2008. http://w3.pppl.gov/ntcc/Jsolver/.

[82] Johan Carlsson. NTCC teq module, August 2008. http://w3.pppl.gov/ntcc/Teq/.

[83] T. E. Stringer. Diffusion in toroidal plasmas with radial electric field. *Phys. Rev. Lett*, 22(15):770–774, April 1969.

[84] M. N. Rosenbluth and J. B. Taylor. Plasma diffusion and stability in toroidal systems. *Phys. Rev. Lett.*, 23(7):367–370, August 1969.

[85] A. A. Galeev. Influence of termperature perturbation on plasma diffusion in toroidal systems. *ZhETF Pis. Red.*, 10(7):353–357, October 1969.

[86] O. P. Pogutse. Classical diffusion of a plasma in toroidal systems. *Nuclear Fusion*, 10:399–403, 1970.

[87] A. Bondeson and D. J. Ward. Stabilization of external modes in tokamaks by resistive walls and plasma rotation. *Phys. Rev. Lett.*, 72(17):2709–2712, 1994.

[88] A. M. Garofalo, E. J. Strait, L. C. Johnson, R. J. La Haye, E. A. Lazarus, G. A. Navratil, M. Okabayashi, J. T. Scoville, T. S. Taylor, and A. D. Turnbull. Sustained stabilization of resistive-wall mode by plasma rotation in the DIII-D tokamak. *Phys. Rev. Lett.*, 89(23):235001, November 2002.

[89] B. LaBombard, J. E. Rice, A. E. Hubbard, J. W. Hughes, M. Greenwald, J. Irby, Y. Lin, B. Lipschultz, E. S. Marmar, C. S. Pitcher, N. Smick, S. M. Wolfe, S. J. Wukitch, and the Alcator Group. Transport-driven scrape-off-layer flows and the boundary conditions imposed at the magnetic separatrix in a tokamak plasma. *Nucl. Fusion*, 44:1047–1066, 2004.

[90] J. M. Greene, J. L. Johnson, K. E. Weimer, and N. K. Winsor. Intertial and resistive effects in toroidal systems. *Phys. Fluids*, 14(6):1258–1267, June 1971.

[91] B. J. Green H. P. Zehrfeld. Stationary toroidal equilibria at finite beta. *Nucl. Fusion*, 12:569–575, 1972.

[92] R. D. Hazeltine. Rotation of a toroidal confined, collisional plasma. *Phys. Fluids*, 17(5):961–968, May 1974.

[93] H. A. Claassen, H. Gerhauser, and A. Rogister. Neoclassical theory of rotation and electric field in high collisionality plasmas with steep gradients. *Phys. Plasmas*, 7(9):3699–3706, September 2000.

[94] Peter J. Catto and Andrei N. Simakov. Evaluation of the neoclassical radial electric field in a collisional tokamak. *Phys. Plasmas*, 12:012501, 2005.

[95] S. K. Wong and V. S. Chan. Fluid theory of radial angular momentum flux of plasmas in an axisymmetrix magnetic field. *Phys. Plasmas*, 14:112505, 2007.

[96] J. B. Taylor. Relaxation of toroidal plasma and generation of reverse magnetic fields. *Phys. Rev. Lett.*, 33(19):1139–1141, November 1974.

[97] L. C. Steinhauer and A. Ishida. Relaxation of a two-species magnetofluid and application to finite-β flowing plasmas. *Phys. Plasmas*, 5(7):2609–2622, July 1998.

[98] L. C. Steinhauer and Akio Ashida. Nearby-fluids equilibria. i. formalism and transition to single-fluid magnetohydrodynamics. *Phys. Plasmas*, 13:052513, 2006.

[99] G. N. Throumoulopoulos and H. Tasso. On Hall magnetohydrodynamics equilibria. *Phys. Plasmas*, 13:102504, 2006.

[100] S. Semenzato, R. Gruber, and H. P. Zehrfeld. Commputation of symmetric ideal MHD flow equilibria. *Comp. Phys. Rep.*, 1:389, 1984.

[101] A. J. Beliën, M. A. Botchev, J. P. Goedbloed, B. van der Holst, and R. Keppens. FINESSE: Axisymmetric MHD equilibria with flow. *J. Comp. Phys.*, 182(1):91–117, October 2002.

[102] L. Guazzotto, R. Betti, J. Manikam, and S. Kaye. Numerical study of tokamak equilibria with arbitrary flow. *Phys. Plasmas*, 11(2):604–614, February 2004.

[103] L. Guazzotto and R. Betti. Magnetohydrodynamics equilibria with toroidal and poloidal flow. *Phys. Plasmas*, 12:056107, 2005.

[104] F. L. Hinton. Neoclassical transport effects and the H-mode transition. *Nucl. Fusion*, 25(10):1457, October 1985.

[105] T. D. Rognlien, P. N. Brown, R. B. Campbell, T. B. Kaiser, D. A. Knoll, P. R. McHugh, G. D. Proter, and M. E. Resnik abd G. R. Smith. 2-D fluid transport simulations of gaseous/radiative divertor. *Contrib. Plasma Phys.*, 34:362, 1994.

[106] Richard Fitzpatrick. Interaction of scrape-off layer currents with magnetohydrodynamical instabilities in tokamak plasmas. *Phys. Plasmas*, page 062505, 2007.

[107] Leonid E. Zakharov. The theory of the kink mode during the vertical plasma disruption events in tokamaks. *Phys. Plasmas*, 15:062507, 2008.

[108] D. Pfirsch and A. Schlüter. Technical Report MPI/PA/7/62, Max-Planck-Institut für Plasmaphysik, 1962.

[109] F. L. Hinton and S. K. Wong. Neoclassical ion transport in rotating axisymmetric plasmas. *Phys. Fluids*, 28(10):3082–3098, October 1985.

[110] J. W. Connor, S. C. Cowley, R. J. Hastie, and L. R. Pan. Toroidal rotation and momentum transport. *Plasma Phys. and Controlled Fusion*, 29(7):919–931, 1987.

[111] R. Maingi, C. S. Shaing, Seunghoe Ku, T. Biewer, R. Maqueda, M. Bell, C. Bush, D. Gates, S. Kaye, H. Kugel, B. LeBlanc, J. Menard, D. Mueller, R. Raman, S. Sabbagh, V. Soukhanovskii, and the NSTX Team. Effect of gas fuelling location on h-mode access in nstx. *Plasma Phys. Control. Fusion*, 46:A305–A313, 2004.

[112] J. E. Rice, W. D. Lee, E. S. Marmar, N. P. Basse, P. T. Bonoli, M. J. Greenwald, A. E. Hubbard, J. W. Hughes, I. H. Hutchinson, A. Ince-Cushman, J. H. Irby, Y. Lin, D. Mossessian, J. A. Snipes, S. M. Wolfe, S. J. Wukitch, and K. Zhurovich. Toroidal rotation and momentum transport in Alcator C-Mod plasmas with no momentum input. *Phys. Plasmas*, 11(5):2427–2431, May 2004.

[113] A. E. Hubbard J. E. Rice, J. W. Hughes, M. J. Greenwald, B. LaBombard, J. H. Irby, Y. Lin, E. S. Marmar, D. Mossessian, S. M. Wolfe, and S. J. Wukitch. The dependence of core rotation on magnetic configuration and the relation to the H-mode power threshold in Alcator C-Mod plasmas with no momentum input. *Nucl. Fusion*, 45:251–257, 2005.

[114] F. Wagner, R. Bartiromo, G. Becker, H. S. Bosch, A. Eberhagen, C. Fussmann, O. Gehre, J. Gernhardt, G. v. Gierke, E. Glock, O. Gruber, G. Haas, G. Janeschitz, F. Karger, M. Keilhacker, A. Kislyakov, O. Klüber, M. Kornherr, P. B. Kotzé, K. Lackner, M. Lenoci, G. Lisitano, A. Mahdavi, H.-M. Mayer, K. McCormick, D. Meisel, V. Mertens, E. R. Müller, H. Murmann, H. Niedermeyer, W. Poschenreider, H. Rapp, F. Ryter, J. Roth, F. Schneider, G. Siller, P. Smeulders, F. Söldner, E. Speth, K. Steinmetz, K.-H. Steuer, and O. Vollmer. Experimental evidence for neoclassical ion transport effects in the H-transition of ASDEX. *Nucl. Fusion*, 25(10):1490–1495, 1985.

[115] I. B. Bernstein, E. A. Frieman, M. D. Kruskal, and R. M. Kulsrud. An energy principle for hydromagnetic stability problems. *Proc. Roy. Soc. London. Series A*, 244(1236):17–40, February 1958.

[116] S. A. Balbus. *ApJ*, 413, 1993.

[117] M. N. Rosenbluth and C. L. Longmire. Stability of plasmas confined by magnetic fields. *Annals of Physics*, 1:120–140, 1957.